The University Of Sheffield.

Development of New Ti Alloys for Biomedical Applications

by

Yidong Xu

Submitted in accordance with the requirements for the degree of

Doctor of Philosophy

Supervisor: Prof W.Mark Rainforth

The Department of Materials Science and Engineering

University of Sheffield

September 2020

Declaration

I, Yidong Xu, declare that this thesis is my work and has not been submitted in any form for another degree at any other university or other institutes.

Publications Arising from this Thesis

Yidong Xu, Junheng Gao, Yuhe Huang, W.M. Rainforth, "A low-cost metastable beta Ti alloy with high elastic admissible strain and enhanced ductility for orthopaedic application," J. Alloys Compd. 835 (2020) 155391

Yidong Xu, Jiahui Qi, John Nutter, Jo Sharp, Mingwen Bai, Le Ma, W.M. Rainforth, "Correlation between the formation of tribofilm and repassivation in biomedical titanium alloys during tribocorrosion," submitted.

Yidong Xu, Mingwen Bai, Jiawei Xi, Jiahui Qi, John Nutter, Junheng Gao, William Mark Rainforth, "A new laser textured structure to improve tribocorrosion behaviours of Ti-6Al-4V ELI for orthopaedic applications," submitted.

Acknowledgements

Before everything, I would like to express my honest gratitude to my supervisor Prof. Mark W Rainforth. All his patient encouragement and guidance, just liked a light in the dark, supported me to keep moving forward during my doctoral journey. Many thanks are also due to Prof. Iain Todd throughout these four years.

I would like to thank Dr Junheng Gao, Dr Dikai Guan and Dr Yuhe Huang for their kindly help and guidance regarding the design of the composition, arc melting, as well as advanced microscopy technology. It is because of all their valuable suggestions I can avoid making a detour.

I would like to thank Dr Jiawei Xi, Dr Mingwen Bai, Dr Jiahui Qi and Dr John Nutter. They gave me a lot in laser texturing, preparing focus ion beam samples, and characterisations of the worn surface using high resolution transmission microscopy.

I also want to acknowledge Dr Le Ma, Dr Righdan Namus, Dr Cong Liu, Mr Neil Hind for their assistance when necessary.

Finally, I must thank my parents and family for their support and love, especially for my wife, Mrs Lu Yang. I lack independence in daily life. Without her companion and care, it could be very difficult for me during this long journey. Appreciate and love you forever!

Abstract

Ti and its alloys have shown an excellent combination of biocompatibility and mechanical properties to become the first choice for orthopaedic implants. However, one perennial problem is the high stiffness of these alloys which creates a large mismatch between the implant and bone. In this thesis, the author firstly designed a new group of low-cost biomedical Ti-Mo-Fe-Sn alloys: Ti-4Mo-Fe-3Sn, Ti-5Mo-Fe-3Sn and Ti-5Mo-Fe-4Sn (at.%) on the basis of d-electron, average valence electron concentration and Mo equivalent number designing strategies. In addition, a new surface modification strategy via selective laser melting (SLM) was proposed for the current commercialized Ti-6Al-4V ELI (Extra Low Interstitial). The characteristics of their mechanical properties and microstructure evolution after the uniaxial tensile and tribocorrosion tests were studied using scanning and transmission electron microscopy (SEM and TEM).

All developed alloys exhibited similar equiaxed microstructure in the annealed state. In these alloys, the main deformation modes were the formation of stress-induced martensite, multiple twinning and dislocation slip. The balance of these deformation modes correlated with the β phase stability but not with the prediction of the d-electron method. An excellent combination of low elastic modulus (52 GPa) and high yield strength (740 MPa) was achieved in Ti-5Mo-Fe-3Sn, leading to the highest elastic admissible strain (1.42%) in comparison with reported biomedical Ti alloys. It was found that the combined addition of Sn and Fe suppressed the formation of athermal omega phase and introduced solid solution strengthening. Transmission electron microscopy results revealed that with an increase in tensile strain, the {332}<113>

twin system was initiated first, and then secondary {332}<113> twinning and ternary {112}<111> twinning was also observed. The evolution of the multi-twin system during deformation was responsible for the enhanced strain hardening rate and plasticity (elongation ~30%).

Tribocorrosion tests were carried out in new-born calf serum solutions at open circuit potential. The specimen was rubbed at reciprocating frequencies of 5 Hz and 2.5 Hz. The presence of grooves and retained wear debris suggested that the main wear mechanism in all samples was abrasive wear. Ti-5Mo-Fe-3Sn and Ti-6Al-4V ELI were found to have the ability to regain passive state in the wear track when testing at 2.5 Hz. This slower sliding speed was better for protein aggregation at the tribological interface, which further interacted with oxide particles contributing to the compact tribofilm similar to passive film.

SLM of Ti-6Al-4V ELI was undertaken using laser texturing to develop a riblet-like texture. Micropillars were FIB machined from the high points on the surface. In-situ micropillar compression tests of SLM Ti-6Al-4V ELI showed that the strength of the texture increased by 74%. It was mainly attributed to the diffusionless martensite transformation, resulting in grain refinement that contributed to enhanced mechanical properties. Moreover, the specific wear rate of SLM Ti-6Al-4V ELI was three orders of magnitude lower in comparison to the untreated sample for a tribocorrosion test carried at 2.5 Hz. The worn surface characterisation showed it to be ultra-smooth, far smoother than the equivalent test on non-SLM material. In the SLM alloy, wear debris was removed from the tribocontact in the recesses on the surface, which appears to be a key aspect of generating the ultra-smooth worn surface, whereby the laser

texture had prevented 3rd body wear. Additionally, the structural and chemical evolution of the subsurface region was examined after the wear test by precession electron diffraction using the Nanomegas system to generate nanoscale orientation imaging and electron energy loss spectroscopy (EELS) mapping in the TEM. The smooth topography corresponded to a thin tribofilm with metallic characteristic, and the substructure displayed a columnar microstructure with negligible plastic deformation, indicating a better resistance to shear deformation.

Therefore, the results in this thesis show that the newly developed Ti-5Mo-Fe-3Sn alloy is a promising candidate material for support components of orthopaedic implants, such as stem or tibial part. It was also shown that SLM could play a significant role in improving the wear resistance of the current commercialized Ti-6Al-4V ELI alloy, resulting in a huge reduction in debris formation and a removal of 3rd body wear. This technique should work for any titanium alloy.

Keywords: Biomedical Ti alloys; Strain hardening; Deformation mechanism; Tribocorrosion; Tribofilm; Laser surface texture

Contents

List of Figures

List of Tables

Nomenclature

ARMD	Adverse reaction to metal debris.
at.%	Atomic percentage.
α	Alpha.
α'	Hexagonal closed-packed martensite.
α''	Orthorhombic martensite.
BSA	Bovine serum albumin.
β	Beta.
β_c	Critical concentration of β stabilisers.
bcc	Body-centred cubic.
B_o	Bond order.
$\overline{B_o}$	Average bond order.
C_0	Chemical materials degradation.
CCLM	Cold crucible levitation melting.
ΔC_w	Wear accelerated corrosive degradation.
C_w	Total chemical degradation.
C_i	Actual concentration of the element.
C_{ki}	Critical concentration of the element.
e/a	Average electron concentration.
E	Young's modulus.
E_{corr}	Corrosion potential.
E_{pp}	Primary passivation potential.
EAS	Elastic admissible strain.
EELS	Electron energy loss spectroscopy.
ELI	Extra Low Interstitial.
e.g.	For example.
F	Friction force.

fs	Femtosecond.
GPa	Gigapascal.
$\boldsymbol{H}$	Hardness.
HAADF	High-angle annular dark-field.
HAZ	Heat-affected zone.
hcp	Hexagonal closed-packed.
i.e.	That is.
$\boldsymbol{I_{corr}}$	Current density.
$\boldsymbol{I_{cc}}$	Critical current density.
$\boldsymbol{I_p}$	Passive current.
$\boldsymbol{k}$	Specific wear rate.
$\boldsymbol{K}$	Wear coefficient.
$\boldsymbol{K_\beta}$	Coefficient of β stabilisation.
ns	Nanosecond.
nm	Nanometre.
$\mathbf{M_d}$	Metal d-orbital level.
$\mathbf{Mo_{eq}}$	Mo equivalent number.
$\overline{\boldsymbol{M_d}}$	Average metal d-orbital level.
$\mathbf{M_s}$	Martensite transformation start temperature.
$\mathbf{M_f}$	Martensite finish temperature.
MPa	Megapascal.
$\boldsymbol{P}$	Unit area.
PBS	Phosphate buffered solution.
$\boldsymbol{Q}$	Total volume of material loss.
RT	Room temperature.
$\boldsymbol{S}$	Synergy between wear and corrosion.
SBF	Simulated human body fluid.
SEM	Scanning electron microscopy.

SLM	Selective laser melting.
TEM	Transmission electron microscopy.
THA	Total hip and arthroplasty.
TKA	Total knee arthroplasty.
TM	Transition metal element.
tEL	Total elongation.
$\boldsymbol{T}$	Total volume of materials degradation.
TWIP	Twinning induced plasticity.
TRIP	Transformation induced plasticity.
$\boldsymbol{U}$	Sliding velocity.
$\boldsymbol{V_{total}}$	Total materials loss.
$\boldsymbol{V_{mech}}$	Mechanical wear.
$\boldsymbol{V_{chem}}$	Wear accelerated corrosion.
$\boldsymbol{W}$	Normal force.
$\boldsymbol{W_0}$	Pure mechanical disruption.
$\boldsymbol{W_C}$	Total mechanical degradation.
$\boldsymbol{\Delta W_C}$	Corrosion accelerated mechanical degradation.
wt.%	Mass percentage.
YS	Yield strength.
ZRA	Zero-resistance ammetry.
ω	Omega.
℃	Celsius degree.
$\boldsymbol{\mu}$	Coefficient of friction.
μm	Micrometre.
$\boldsymbol{\eta}$	Viscosity.
$\boldsymbol{\rho}$	Bulk density.

Chapter 1 Introduction

1.1 Background and Motivation

Recently, biomedical implants have received much more attention due to the unprecedented trend of population ageing around the world. According to the newest projection from 2020 to 2040, the number of primary total hip and knee arthroplasty (THA and TKA) in the USA will increase by 284% and 401% respectively, which may together result in over four million cases annually [1]. The lifetime of current implants is limited to around 15 years, which means that younger adults (<55 years old) having higher mobility demands during daily life would experience at least one revision after the first implant [2]. The optimized design of implants, such as through the use of modular hip systems, offers a more patient-tailored solution: not only providing flexibility which is beneficial to individual joints but also reducing pain during the revision procedure. However, implant loosening and adverse reaction to metal debris (ARMD), the two most common failure reasons, still keep playing negative effects in the human body and lead to the product degradation eventually [3]–[5].

Thanks to a combination of excellent mechanical and biocompatible properties, Ti and its alloys are generally accepted as the best choice for implant biomaterials. One issue with biomedical implants is the mismatch in stiffness between the bone and the implant. For traditional alloys such as Ti-6Al-4V ELI, this mismatch is large and can lead to problems associated with stress shielding. Therefore, there is a drive to develop biomedical materials with lower stiffness closer to that of bone. To date, the lowest elastic modulus reported for metastable beta biomedical Ti alloys is around 40 GPa [6], [7]. However, there still remains

some shortcomings limiting their application in the field of orthopaedics. It is reported the lack of strain hardening in beta Ti alloys may lead to the generation of severe wear debris in human body fluid [8]. Moreover, poor tribological performance coming from low shear resistance and weak protection of oxide layer also gives rise to concern [9], [10]. Thus, given the difficulty in performing revision replacement (especially for THA), and the growing shift of the distribution of patient age distribution to younger groups, it becomes extremely urgent to develop and improve the properties of biomedical Ti alloys.

1.2 Aims and Objectives

The current project aims to develop new Ti alloys for biomedical applications, investigate and compare their tribocorrosion behaviour in protein-containing solutions, and improve tribocorrosion performance using recent cutting-edge selective laser melting technology. The detailed objectives of the proposed program are outlined as follows:

1. To design new metastable β Ti alloys based on empirical designing strategies, such as the "d-electron" approach and average electron concentration method, meanwhile, to reduce the alloy cost using cheap alloying elements, such as Fe.
2. To understand the micro- and nano-scale microstructure evolution of the materials during thermomechanical treatment and plastic deformation through SEM and TEM.
3. To investigate the correlation between the formation of tribofilm and repassivation in designed Ti alloys during tribocorrosion test based on the SEM observation of the worn surface and the composition analysis from surface to subsurface.

4. Investigate the effect of selective laser melting on surface topography and microstructure using optical profilometry and X-ray diffraction, thereby based on *in-situ* micropillar compression and hereafter TEM observation of deformed microstructure, to generate a comprehensive understanding of the difference of mechanical properties between the primary and treated surface.
5. To investigate the effect of surface texturing on tribocorrosion behaviour in protein-containing simulated human body fluid (SBF) using ball-on-disc reciprocating apparatus. To evaluate laser texturing of Ti-6Al-4V alloy for biomedical applications through comparing the worn surface and material loss to untreated samples.

1.3 Thesis Outline

Chapter 2 firstly gives a review of biomedical Ti alloys for orthopaedic applications, including basic theories, recent understanding of microstructure, designing strategies and deformation mechanism. Tribocorroison behaviour and laser surface modification of biomedical Ti alloys are also presented.

Following the literature review, Chapter 3 describes the methodology and experimental procedures, contains detailed information about sample preparation, thermomechanical processing, surface treatment, mechanical property analysis, tribocorrosion tests and various characterisation techniques applied in this study.

Chapter 4 describes a new group of designed Ti-Mo-Fe-Sn alloys with corresponding phase analysis. Mechanical properties based on tensile test and deformation mechanism are reported. Also, the potential for biomedical application is discussed in detail.

In Chapter 5, further investigation of the tribocorrosion behaviour is provided. Comparison of specific wear rate, worn surface, structural evolution of subsurface and electrochemical behaviour between Ti-Mo-Fe-Sn alloys and commercialised Ti-6Al-4V ELI are summarised and discussed.

Chapter 6 and 7 introduce a new routine to optimise next-generation Ti alloys via advanced additive manufacturing technique: surface modification via selective laser melting, which includes design strategies and microstructure results, mechanical properties, tribocorrosion behaviour and structural evolution of subsurface.

Chapter 2 Literature Review

2.1 Titanium Alloys for Biomedical Applications

2.1.1 Fundamentals of titanium and its alloys

Titanium was first discovered by William Gregor in 1791. As the rapid development of metallurgy occurred after World War II (i.e., after the creation of the "Kroll method"), titanium and its alloys started to be given great attention. Pure titanium has two main crystal structures: hexagonal closed-packed (hcp) at ambient condition and body-centred cubic (bcc) above 882 ℃, named α and β phase, respectively [11]. As illustrated in Fig.2.1, the room-temperature lattice constants for α phase are a = 0.295 nm and c = 0.468 nm, resulting in a c/a ratio of 1.587, which is smaller than the ideal hcp structure (1.633).

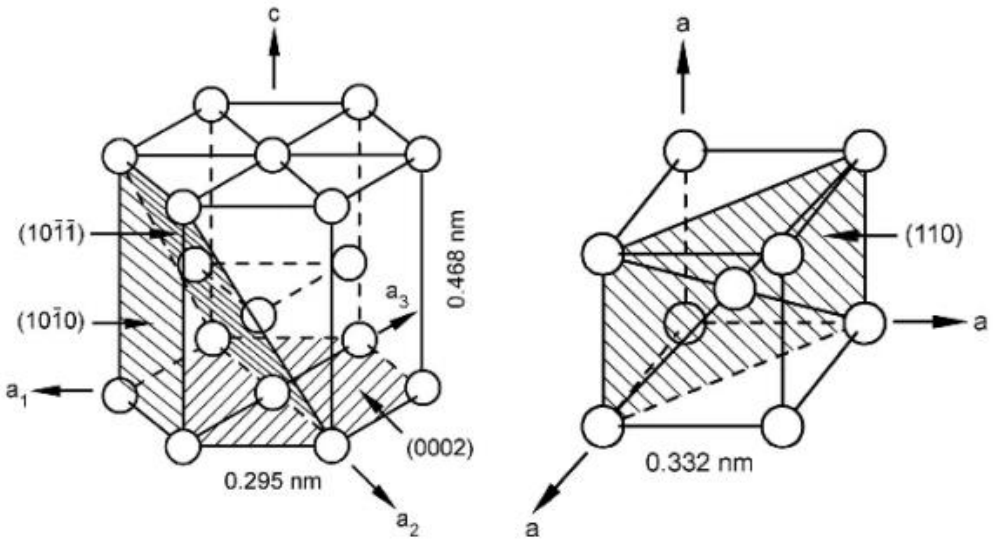

Fig.2. 1. *Two basic crystal structure of titanium [11].*

Alloying elements in titanium alloys can be summarised into three groups: α stabilisers, β stabilisers and neutral elements. It can be seen in Fig.2.2, α stabilisers (e.g., Al, N, O, etc.) can increase the β transus temperature via either substituting or interstitial filling lattice site. Accordingly, the β phase can be fully retained at room temperature by adding a certain amount of β stabilisers (e.g., Mo, Nb, Fe, Cr, etc.). It should be noted that β stabilisers are further divided into isomorphous- and eutectoid-type of elements depending on their solubility. Unlike isomorphous elements with complete solubilities in the β phase, the intermetallic compound would be formed during solidification when eutectoid elements exceed the critical point. Other elements (e.g., Zr, Sn and Hf) that have a weak effect on the formation of α and β phase are often termed as neutral elements.

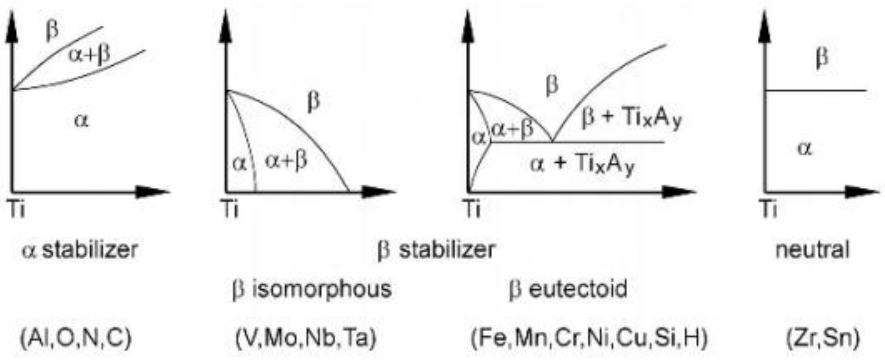

Fig.2. 2. *Schematic plot illustrating phase transformation of titanium alloys based on various alloying elements [11].*

2.1.2 Metastable transformation in titanium alloys

Titanium alloys are classified into α alloys, α+β alloys, β alloys depending on the amount of retained equilibrium phases (i.e., α and β) at room temperature. The transformation between α and β is a diffusion process in which atoms can undergo long-range movement and would be strongly affected by external circumstances, such as cooling rate and heat treatment temperature. Generally, the β phase has a lower Young's modulus in comparison to the α phase. Thus, developing new β Ti alloys has received considerable attention for orthopaedic application. However, there are two kinds of metastable transformation due to displacive transformation: the formation of martensite and omega phase, which play a significant role in the evolution of microstructure as well as mechanical performance in titanium alloys [11], [12].

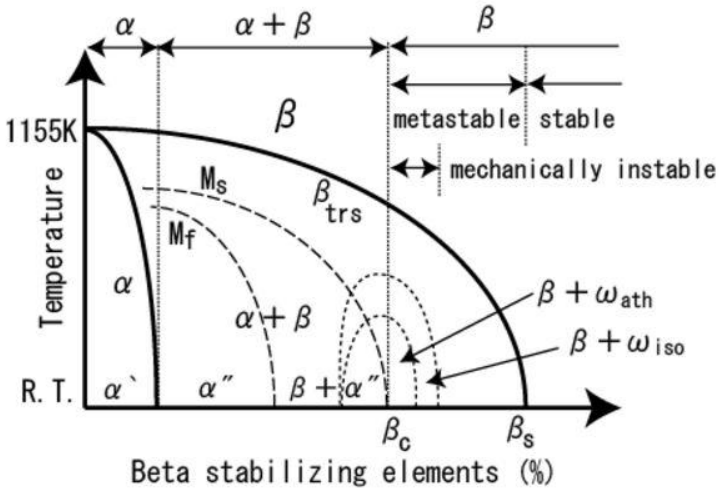

Fig.2. 3. *Schematic of classification of Ti alloys based on stability of β phase (amount of β stabilisers) [13].*

As illustrated in Fig.2.3, the stability of the β phase is directly linked to the amount of β stabilisers. It is found that martensite with orthorhombic crystalline structure α″ could be

formed when the amount of β phase stabilisers is below a critical level (indicated by β_c), and hexagonal closed pack (hcp) martensite α′ would appear with a further reduced amount. Such transformation is attributed to the elastic instability of bcc lattice similar to the martensitic transformation widely reported in iron [13].

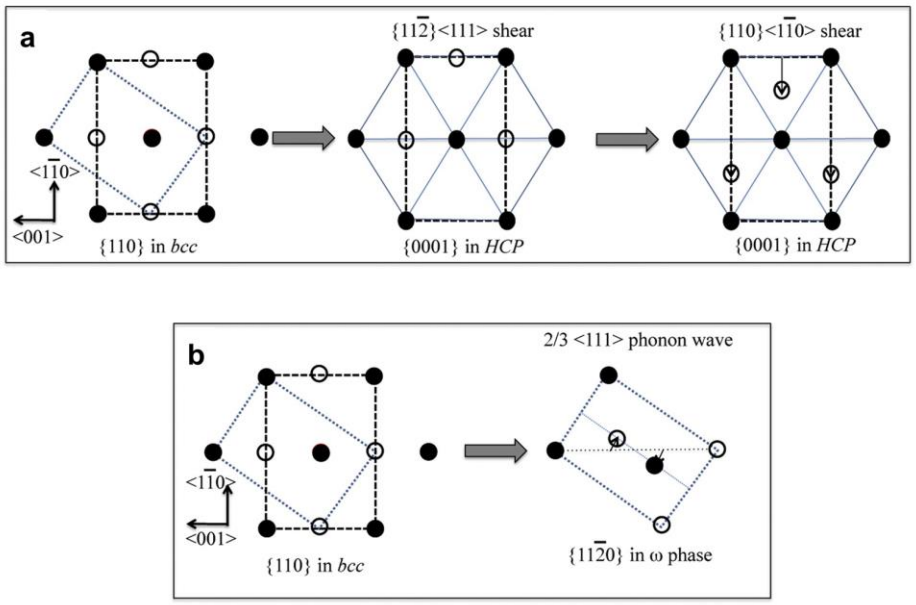

Fig.2. 4. *Schematic illustration of (a) martensitic transformation and (b) the formation of omega phase [17].*

From a thermodynamic viewpoint, molten titanium alloys attempt to achieve the lowest Gibbs energy state during cooling from high temperature. Martensitic transformation can accommodate the insufficient drop in free energy during rapid cooling, leading to atomic shuffle compared to the parent lattice [13]. As the amount of β stabilisers decreases, the starting temperature for martensite transformation (M_s), representing the stability of martensite would increase as well. Thus, the quenched microstructure is supposed to be dominated by martensite when the M_s is above room temperature. As shown in Fig.2.4a, {11-2}<111> shear strain and

resulting {110} plane shuffle along the <1-10> direction together contribute to the lattice distortion, in which larger magnitude corresponds to orthorhombic α″ and less displacement represents hcp α′ [14]. They satisfied the Burgers relationship with β lattice: $\{110\}_{\beta}$ // $\{0001\}_{\alpha'}$, $<111>_{\beta}$ // $<1120>_{\alpha'}$ and habit plane is close to $\{334\}_{\beta d}$ or $\{344\}_{\beta}$; $\{110\}_{\beta}$ // $\{001\}_{\alpha''}$, <111> // $<110>_{\alpha''}$ and habit plane is $\{133\}_{\beta}$ [13]–[17]. For different compositions, the boundary between α′ and α″ is different, and the morphology of martensite is usually acicular or lath-like plates (Fig.2.5) [18], [19]. It is worth noting that the activation of the internal twinning structure is widely observed, resulting from the transformation strain accommodation. Additionally, martensite can be stress-induced during deformation because stored energy from deformation decreases the phase transformation resistance and provides the driving force [20].

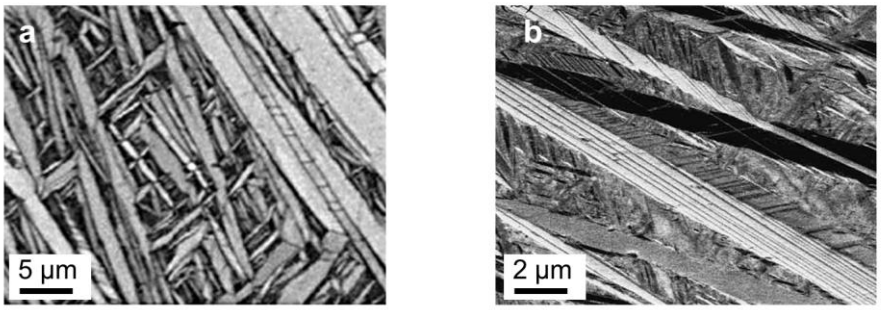

Fig.2. 5. *SEM images of quenched Ti-4Mo and Ti-7.5Mo displaying fine arrangement of acicular martensite [18], [19].*

In comparison to the martensitic transformation, two types of ω phase: athermal and isothermal ω phase, have been observed in many metastable Ti alloys with higher β phase stability. The transformation from bcc to hexagonal lattice (not closed-packed) is derived from a longitudinal 2/3 <111> phonon wave, which results in the collapse of $\{111\}_{\beta}$ plane in pairs and shuffles to

become a new plane (Fig.2.4b) [14], [21]. The transformation satisfies the Burgers relationship with β lattice: $\{1\text{-}10\}_\beta$ // $\{11\text{-}20\}_\omega$, $<111>_\beta$ // $[0001]_\omega$, and the nucleation of ω embryos is diffusionless and usually occurs instantaneously.

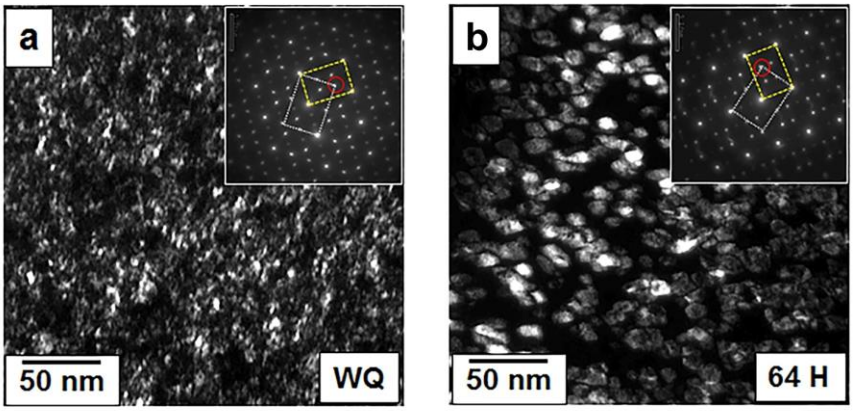

Fig.2. 6. *Dark-field TEM image of omega phase in Ti-19V (at.%) along [110] zone axis: as-annealing condition (a) and ageing at 300 ℃ for 64h (b) respectively.*

Microscopically, the athermal ω phase has a homogeneous distribution with extremely fine nanostructure in the quenched state (Fig.2.6a). On the other hand, the isothermal ω phase usually grows from athermal ω embryos via solute atom diffusion during ageing at 200-500 ℃ or slow cooling from high temperature [22], [23]. As shown in Fig.2.6b, the morphology of the isothermal ω phase can be divided into cuboidal and ellipsoidal depending on the misfit of alloying systems [13], [24], [25]. Isothermal ω phase is cuboid in high misfit system, such as Ti-V, while ellipsoidal shape in low misfit system, such as Ti-Mo. Recently, ω assisted α precipitation attracted intensive attention. Extremely fine precipitation structures can be achieved to realize superior strength through appropriate ageing in some metastable Ti alloys [25]–[27]. However, it should be noted that enhanced strength often comes at the expense of

ductility, which may reduce the formability of alloys via the initiation of defects during thermomechanical processing.

The Young's modulus of Ti alloys mainly depends on their crystal structure. It is generally accepted β phase has the lowest value among all phases, and the sequence of Young's modulus among different phases is: ω > α > α′ > α″ > β [1]. Athermal ω phase formed during quenching has the highest Young's modulus because the lattice misfit between ω and matrix leads to higher strain at the coherent interface. Hexagonal closed-packed (hcp) α phase and hcp martensite (α′) exhibit a higher Young's modulus than body-centred (bcc) phase and orthorhombic martensite (α″) [28]. Additionally, metastable Ti alloys also have the risk of embrittlement due to room temperature ageing even though the amount of athermal ω phase is very low, which is a challenge for practical applications [29]. Therefore, extensive work has focused on the development of metastable β Ti alloys through stabilising high-temperature β or β+α″ to ambient temperature, such as Ti-24Nb-4Zr-8Sn (Ti2448) and Ti-29Nb-13Ta-4.6Zr (TNTZ) presenting very low Young's modulus [30]–[35].

2.1.3 Design strategies for biomedical titanium alloys

Ideal metallic alloys for biomedical application require that candidate composition should have superior mechanical performance and excellent biocompatibility as well as wear resistance. Currently, there are several empirical and theoretical strategies developed to design metastable Ti alloys. It is thus necessary to propose a considerable evaluation to avoid extra experimental works. The following summarises their advantages and limitations in detail.

2.1.3.1 Element selection

As mentioned above, alloying elements in Ti can be divided into α stabilisers, β stabilisers and neutral elements. In order to avoid side effects from potential toxicity, some elements such as Co, Cr and V should be removed from the sketch. Representative β stabilisers: Nb, Ta, Mo, Fe and Mn are preferred. The first three of them are isomorphous elements, while Fe and Mn are eutectoid elements which means the addition should be limited to a certain amount to avoid segregation. Additionally, Zr and Sn are usually added to enhance mechanical properties and corrosion resistance. From recent investigations, Zr and Sn could be recognized to decrease martensite transformation start temperature (M_s) and behave as weak β stabilisers. In the Ti-Mo system, M_s decreased by 80 and 90K when the addition of Zr and Sn increased each atom%. The quenched microstructure could transform from α″ + β to full β structure, and the athermal ω phase was suppressed as well [36]–[38]. Thus, it would be effective to apply Zr or Sn in designing biomedical Ti alloys, which may tune microstructure and realise lattice softening, i.e., a lower Young's modulus.

2.1.3.2 "d-electron" approach

For a multi-element Ti-based system, predicting the interaction between various elements and eventual microstructure is much more complicated. Since the 1990s, a theory based on the molecular orbit calculation of electronic structure was developed, namely the "d-electron" approach [32], [39]. This method estimates the bond strength between Ti and alloying elements through two electronic parameters: B_o (bond order) and M_d (the metal d-orbital level). The

average values of B_o and M_d in Ti alloys are denoted as $\overline{B_o}$ and $\overline{M_d}$ which are calculated as following formulas:

$$\overline{B_o} = \sum_{i=1}^{n} x_i (B_o) i \quad (2.1)$$

$$\overline{M_d} = \sum_{i=1}^{n} x_i (M_d) i \quad (2.2)$$

Where x_i, $(B_o)i$ and $(M_d)i$ is atomic percentage, B_o and M_d of alloying element i respectively. On the basis of this, Niinomi's group calculated and developed $\overline{B_o}$ and $\overline{M_d}$ of various reported Ti alloys and plotted well-known $\overline{B_o} - \overline{M_d}$ diagram (Fig.2.7) [28]. This map can provide information about the resulting microstructure as well as the corresponding deformation mechanism. Taking one of the commercialised β Ti alloys: Ti-12Mo-6Zr-2Fe alloy as an example, the diagram reveals the location within the slip region and with respect to β Ti alloys, which thus suggests the as-quenched alloy has a fully bcc structure and the deformation is dominated by dislocation slip. Additionally, when $\overline{B_o}$ ranges from 2.75~2.85 and $\overline{M_d}$ ranges from 2.35~2.45, metastable Ti alloys can be formed, and increasing values of $\overline{B_o}$ and $\overline{M_d}$ are also consistent with a low Young's modulus. However, from the author's viewpoint, this diagram just introduces a general framework in designing new biomedical Ti alloys; accurate range composition still needs more experimental validation.

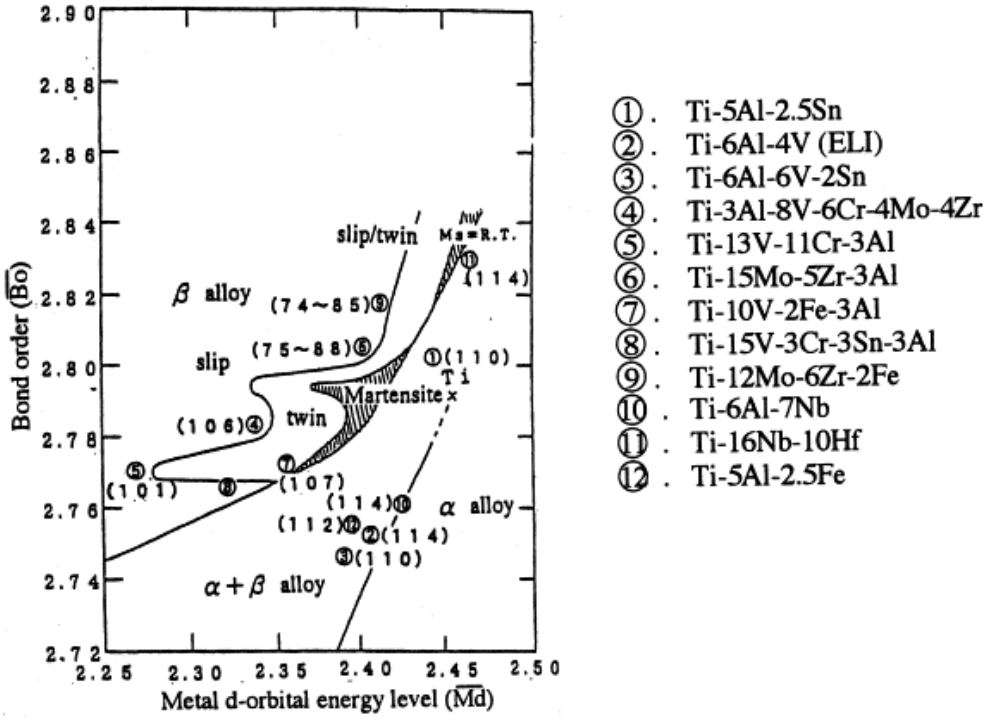

Fig.2. 7. $\overline{B_o} - \overline{M_d}$ *diagram showing the position of some recent developed titanium alloys [32].*

2.1.3.3 Average electron concentration method

Average electron concentration (e/a) is defined as the average number of valence electrons per atom. Ikehata [40] calculated critical e/a concentration of Ti-TM (transition metal element) binary system and proposed a critical e/a of 4.20, which could promise retained full β phase at room temperature. It was also found that Young's modulus could be the smallest when e/a ranged from 4.20~4.24. However, this calculation does not consider the effects of metastable phases in Ti alloys.

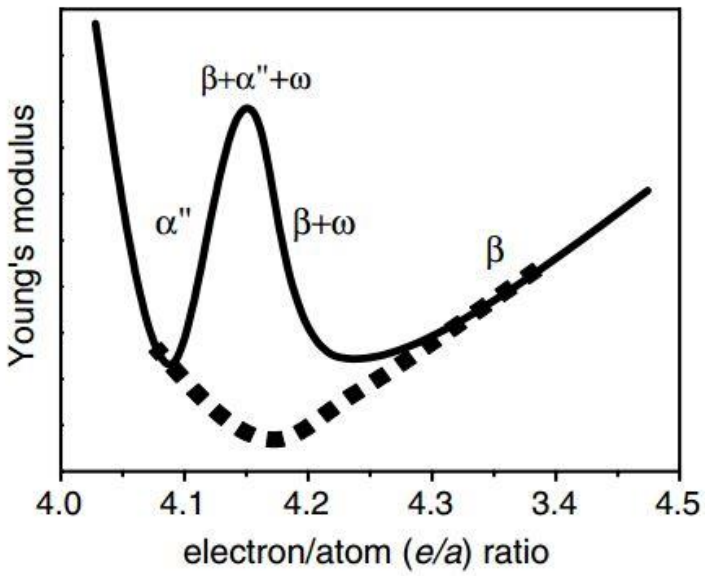

Fig.2. 8. *Effects of e/a on Young's modulus and stability of β phase in Ti-M binary system [31].*

Fig.2.8 shows the correlation between Young's modulus and e/a in Ti-TM binary system. When e/a is around 4.10 and 4.20, Young's modulus is smaller thanks to fully orthorhombic martensite and suppression of ω phase. The dotted line also indicates another potential condition that composition can reach the smallest Young's modulus theoretically if ω formation is completely suppressed in α″ + β structure. Thus, the proposed value of e/a should be controlled from 4.10 to 4.25 to design new composition with ultra-low Young's modulus [31].

2.1.3.4 Coefficient of β stabilisation (K_β) & Mo equivalent number (Mo_{eq})

From Fig.2.3, the critical concentration of β stabilisers (β_c) represents the smallest amount of element needed to retain a fully beta structure at room temperature in a binary system. Thus, the coefficient of β stabilisation (K_β) based on β_c is developed to evaluate well the β phase stability in the multi-element system, which is defined as the following formula [29]:

$$K_\beta = \sum_{i=1}^{n} \frac{C_i}{C_{ki}} \qquad (2.3)$$

Where C_i and C_{ki} is actual and critical concentration of the element in the alloy. Table 2.1 lists the critical concentration of common β stabilisers in Ti alloys. Wang et al. [41] suggested that the critical K_β between α+β alloys and metastable β alloys is around 1.0 while that of stable β alloys is above 2.5. Therefore, in order to design metastable Ti alloys K_β of proposed composition are controlled from 1.0 to 2.5.

Another similar strategy is called Mo equivalent (Mo_{eq}), taking critical concentration of Mo as a reference and denoted as following formula [42]:

$$Mo_{eq} = [Mo] + 0.2[Ta] + 0.28[Nb] + 0.4[W] + 0.67[V] + 1.25[Cr] + 1.25[Ni] + 1.7[Mn] + 1.7[Co] + 2.5[Fe] \quad [Element] in\ wt.\% \qquad (2.4)$$

Mo_{eq} of metastable Ti alloys range from 8 to 12 [2]. It should be noted that both methods do not consider the effects of neutral elements during alloy design, such as Sn and Zr, which are

reported to suppress the martensitic transformation during quenching, indicating weak β stabilising effects [43]–[45]. Additionally, the reported coefficients for these elements are different from those in other publications depending on the critical concentration measurement. Therefore, it is challenging to obtain a predictable range of value in Ti, and an accurate value of specific composition still needs further experimental confirmation.

Table 2. 1 *The critical concentration of β stabilisers [41].*

Element	Concentration (wt.%)	Concentration (at.%)
Mo	10.0	5.2
Ta	45.0	17.8
Nb	36.0	22.5
W	22.5	7.0
V	15.0	14.2
Ni	9.0	7.5
Co	7.0	5.8
Fe	3.5	2.4

2.1.4 Review of recently developed Ti alloys for orthopaedic applications

Decreasing Young's modulus of metallic implants is a persistent challenge in developing new biomedical Ti alloys. Although a series of new metastable Ti alloys were developed with Young's modulus as low as 38 GPa [6], their mechanical properties still cannot meet long-time

implantation requirements. In 2010, a number of modular hip components made of Ti-12Mo-6Zr-2Fe (TMZF) from Stryker were recalled by the US Food & Drug Administration due to the occurrence of unacceptably high levels of wear debris in use [46]. After a comparison between TMZF and Ti-6Al-4V in corrosion-wear condition, it was found the strain softening could be the dominant reason, which meant strain hardening was not only important to the improvement of mechanical properties but also may enhance tribocorrosion behaviour of Ti alloys [8]. The lack of strain hardening in Ti alloys is the main reason for the poor ductility, especially in stable β Ti alloys. With a growing number of active patients who have more physical activities than elderly patients, a better combination of strength and ductility, as well as decreasing Young's modulus, should be given more attention [47].

Table 2. 2 *Mechanical properties of some recently developed biomedical Ti alloys, including alloy type, yield strength (YS), Young's modulus (E), elastic admissible strain (EAS) and total elongation (tEL).*

Alloy	Alloy type	E (GPa)	YS (MPa)	EAS	tEL (%)
Ti-6Al-4V ELI [2]	α+β	110	900	0.82	10-15
Ti-34Nb-25Zr [48]	β	62	810	1.31	14.8
Ti-31.7Nb-6.2Zr-1.4Fe-0.16O [49]	β	62	1038	1.67	9
Ti-13Nb-13Zr (aged) [50]	β	81	872	1.08	13
Ti-35.3Nb-5.1Ta-7.1Zr [50]	β	55	547	0.99	19

Ti-19Nb-2.5Fe-6Sn (aged) [45]	β+α	98	1261	1.29	6
Ti-19Nb-2.5Fe-10Zr [45]	β	69	1027	1.49	31
Ti-12Nb-5Fe (at. %) [51]	β	90	740	0.82	42
Ti-29Nb-13Ta-4.6Zr (aged) [50]	β	80	864	1.08	13
Ti-23Nb-0.7Ta-2Zr-1.2O (at. %) [52]	β	65	850	1.31	19
Ti-33Nb-4Sn (cold rolled) [35]	β+α″	44	665	1.51	~4
Ti-15Mo (annealed) [50]	β	78	544	0.70	21
Ti-12Mo-6Zr-2Fe (annealed) [50]	β	80	1030	1.29	20
Ti-7.5Mo [18]	β+α″	55	386	0.70	29
Ti-7.5Mo-0.3O [18]	β+α″	67	711	1.06	17
Ti-15Mo-0.2O [53]	β	83	680	0.82	42
Ti-15Mo-0.5O [53]	β	87	1180	1.36	10
Ti-3Mo-0.5Fe (at. %) [54]	β+α	82	~600	0.73	18
Ti-25Ta [55]	α″	64	480	0.75	20
Ti-50Ta (aged) [56]	β+α	77	612	0.79	12
Ti-10Ta-4Fe (at. %) [51]	β	121	1360	1.12	14
Ti-25Ta-25Nb [57]	β	55	530	0.96	20
Ti-9Mn [58]	β	94	1023	1.09	19
Ti-5Mn-4Mo [59]	β	91	815	0.90	34
Ti-6Mn-3Mo [59]	β	89	1200	1.35	15

Table 2.2 lists recently developed Ti alloy and corresponding mechanical properties. It has been observed that metastable and stable β alloys often present a better ductility thanks to the high symmetry of the bcc structure, in which there exists a larger number of slip systems than the hcp structure. For instance, full β Ti-15Mo-0.2O presents a ductility of 42%, which is almost four times larger than the value of Ti-6Al-4V ELI with α + β structure. Moreover, it suggests that ultra-high yield strength would be achieved through heat or mechanical processing route. After ageing at 450 ℃ for 12 hours, Ti-19Nb-2.5Fe-6Sn presents a much higher yield strength, increasing from 765 to 1261 MPa [45]. However, it is also worth noting that the transition of microstructure results in the increase of Young's modulus (from 71 to 98 GPa), as well as poor ductility (reduced from 31 to 6%). Therefore, especially for biomedical Ti alloys, a new parameter termed as elastic admissible strain (EAS) is developed to monitor their mechanical properties, which is defined as the ratio of yield strength to Young's modulus [48]. A higher value of EAS with enhanced ductility is supposed to be an appropriate indicator of Ti alloy for orthopaedic applications.

Additionally, mechanical properties of martensite are still in dispute, some groups recently found quenched structure containing α′ and α″ had a lower modulus and higher strength [15], [16], [60], [61]. Recent research about the investigation of continuous changing of lattice parameter ratio of metastable Ti alloys at different temperature using *in-situ* synchrotron-based X-ray diffraction (SXRD) technique may have helped in revealing the correlation between Young's modulus of the martensite and matrix and develop new martensite-type biomedical Ti alloys [62], [63].

2.1.5 Twinning induced plasticity (TWIP) and transformation induced plasticity (TRIP)

In Ti alloys, there are various deformation mechanisms, including conventional dislocation slip, twinning, stress-induced martensite or ω phase formation. From the $\overline{B_o} - \overline{M_d}$ diagram (Fig. 2.7), it is found that activation of these deformation modes is strongly associated with the metastability of the β phase and chemical composition. Deformation modes will change from slip to stress-induced transformation and twinning when the stability of the β phase decreases, {332}<113> or {112}<111> twinning, or both. {332}<113> twinning often appears in metastable β Ti alloys, while {112}<111> twinning is usually observed in stable β alloys [25], [64].

The approach to overcoming the strength-ductility trade-off of metals is to introduce dislocation obstacles during plastic deformation, such as precipitation hardening and refinement of crystal grains [65]. Considering the generation of massive twin and phase boundaries and their potential to prevent dislocation glide, a designing strategy, namely twinning induced plasticity (TWIP) and transformation induced plasticity (TRIP), is proposed in Ti alloys [66]–[70]. The stability of the β phase is controlled within the metastable region by adjusting the chemical composition.

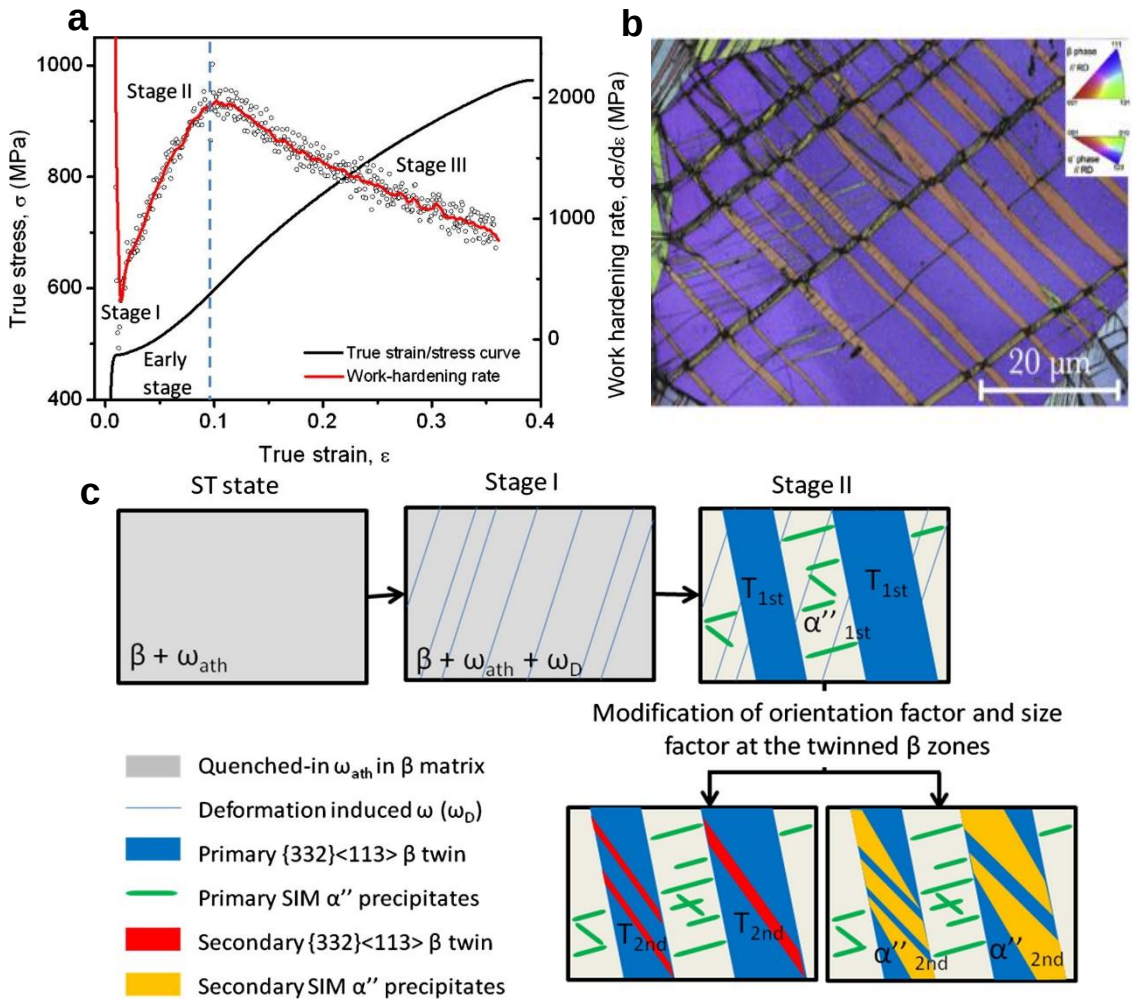

Fig.2. 9. *(a) Tensile true stress-true strain and working hardening rate curve of Ti-12Mo. (b) EBSD image of Ti-12Mo at a strain of 5%; (c) Schematic evolution of deformation mechanism in Ti-12Mo alloys [71], [72].*

Sun's group studied the evolution of deformed structure of Ti-12Mo, a metastable β Ti alloy [71], [72]. It was found that the deformation process could be divided into three stages based on the strain hardening curve (Fig.2.9a): conventional elastic to plastic region (stage I), a rapid increase of strain hardening rate (stage II) and strain softening (stage III). At stage II, EBSD and TEM observation confirmed the presence of {332}<113> twinning and stress-induced martensite (α″). The activation of the various variant of the primary {332}<113> twins, as well

as needle-like martensite precipitates, thus generated an intragranular network (Fig.2.9b). From a classic view, networking of deformation products could reduce the mean free path of dislocation slip and perform as dislocation obstacles, leading to high strain rate, also termed dynamic hardening [73]. As further illustrated in Fig.2.9c, the primary {332}<113> twins would be strengthened by secondary internal {332}<113> twins and α″ depending on the crystalline orientation of matrix, suggesting a strong capacity of strain accommodation.

Through the *in-situ* electron backscattered diffraction technique (EBSD), more details of the correlation between TWIP and TRIP are recently revealed. Lai et al. [17] found that the {332}<113> twin was actually coupled with stress-induced α″, and initiation of twinning usually occurred at the grain boundary. More recently, Lilensten et al. [74] investigated the *in-situ* deformation behaviour of metastable Ti-10V-4Cr-1Al alloy. It was found that the formation of twinning and martensite essentially was preferred in certain grain orientations, which suggested a heterogeneous deformation behaviour in metastable Ti alloys.

2.1.6 The cost factor

Also indicated from Table 2.2, Ti-Nb or Ta based biomedical Ti alloys have very low modulus. Due to their relatively low beta stabilising effects, large addition is usually required to increase the stability of the β phase, which may lead to an increase in bulk density. Additionally, considering their supply disruption, such as fluctuating price and low stock, the addition of these rare elements will result in the accelerating price growth of raw materials. Thus, it seems

not sustainable for a long period in the field of bulk implants such as hip and knee replacement, where increasing demand is predicted for the future.

Recently, a series of Ti alloys containing Mn and Fe were developed [51], [54], [58]. Niinomi's group found that the amount of athermal ω phase decreased as the percentage of Mn increased in Ti-Mn binary system. Among several developed compositions, Ti-9Mn had the lowest Young's modulus (94 GPa) as well as excellent mechanical properties compared to Ti-6Al-4V ELI [58]. Soon after, to reduce the potential risks of Mn toxicity during tribocorrosion, they also optimized Ti-Mn binary system with the addition of Mo, and it revealed that Ti-(5-6)Mn-(3-4)Mo had comparable electrochemical properties to CP-Ti. Additionally, they also exhibited TWIP and TRIP effects, which led to better ductility and larger strength [59]. However, due to the difference in vapour pressure between Mn and Ti, using the arc-melting method is difficult to promote the nominal content of Mn in composition. Instead, the cold crucible levitation melting technique (CCLM) was applied to melt Ti-Mn based alloys and the measured difference between nominal and actual Mn content was control under 10%.

Fe is another cheap element with a strong β stabilising effect. It is recently added in the Ti-Nb(Ta) system to realize both superior mechanical properties and cost reduction in new biomedical Ti alloys. It is attractive that the yield strength of Ti-10Ta-4Fe (at.%) can reach 1360 MPa while maintaining Young's modulus at 121 GPa, which has the potential for the development of a low-cost, porous biomedical implant [51]. Meanwhile, melting compositions that do not have Mn avoid evaporation issues. Thus, Fe can be regarded as a more suitable alloying element than Mn to be used in designing low-cost biomedical Ti alloys. However,

although they showed comparable corrosion rate and biological properties to CP-Ti and Ti-6Al-4V, strain softening problem still exists in these developed alloys, which may cause the formation of wear debris similar to TMZF [75]. Therefore, it is suggested that tribocorrosion properties of these developed alloys should be investigated to confirm their suitability for eventual application in next-generation orthopaedic biomaterials.

2.2 Tribology and Corrosion in Implant

Tribology can be simply defined as a subject focused on the relative motion between two contacting solid surfaces, including three main characteristics: friction, wear and lubrication. From the sole of shoes to gearboxes in spacecraft, it covers all fields around the world and accounts for almost a quarter of total energy consumption annually [76]–[78]. *In-vivo* tribological performance of an implant directly determines postoperative feeling and the lifetime of the product.

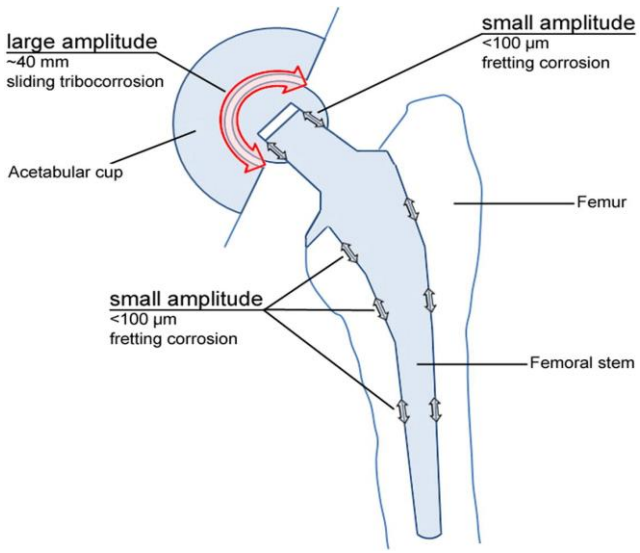

Fig.2. 10. *Illustration of tribological contact in an artificial hip configuration [77].*

As illustrated in Fig.2.10, a conventional configuration of an artificial hip consists of three main contacting surfaces: femoral head-cup, neck-head and stem-cement [79]. For the recent developed modular design with an exchangeable neck, there is the additional interface of the stem-neck [80]. According to the previous analysis, their contacting modes are directly related to their functions and the relative distance of motion normally ranged from tens of micrometres to millimetres [81]. Additionally, it should be noted that the lubricating condition of an implant is much more complicated due to the electrochemically active environment in human body. Implant undergoes both mechanical and corrosive damage, together presenting a synergistic effect on material degradation. Thus, the tribological performance of an implant in the human body is often categorized as tribocorrosion. More details and corresponding fundamentals are reviewed and discussed in the following section.

2.2.1 Fundamentals of friction

Classical friction theory derived from Amontons' laws of friction describes three main characteristics of friction [82]:

1. The frictional force F between contacting surface is proportional to the normal force W, and the relationship can be expressed as follows:

$$F = \mu W \qquad (2.5)$$

Where the ratio μ of F and W is known as the coefficient of friction.

2. The frictional force is independent of the apparent area.
3. The frictional force is independent of the sliding velocity.

Note that these laws provide a fundamental frame to understand friction under unlubricated condition, and they are applicable to most materials. However, how to explain the origin of the frictional force is a challenging task because even the well-polished surface still presents a distribution of asperities, i.e., surface roughness. It could not only introduce material transfer due to strong adhesion effects along the shear direction but also deformation of asperities if the material has a weak ability of strain accommodation. Thus, recent viewpoints attribute tribological energy dissipation to the contribution of both adhesion and deformation [82]. For passive metals, deformation of asperity plays a more significant role during sliding because the oxide film on the surface would weaken the ductility of asperities and decrease adhesive force upon the initiation of shearing [83].

2.2.2 *Archard* wear equation

During rubbing tribological pairs, it is inevitable that hard asperities will compress and plough the soft asperity, introducing damage such as cracks, delamination and debris on the surface. Thus, this progressive material degradation is termed as wear and responsible for the main tribological energy dissipation alongside friction in industrial applications. The classic theory to describe wear is *Archard* wear equation, which is given as follows [82], [84]:

$$Q = \frac{KW}{H} \tag{2.6}$$

Where Q is the total volume of material loss, W is the normal load, and H is the hardness of the worn surface. The dimensionless constant K can directly reflect the attrition of tribological pairs and usually known as the wear coefficient. However, it should be noted that the hardness of a surface may be affected by an acceleration of dynamical events in the subsurface, e.g. dislocation slip, deformation twinning and martensite formation, which can contribute to the hardness gradient from the surface to the substrate [85], [86]. Thus, K/H is termed as specific wear rate k for simplicity in a unit of $mm^3\ m^{-1}\ N^{-1}$. This expression is favourable to make a comparison between various materials and initially determine their wear resistance.

Wear can be classified into mild and severe wear based on the worn surface topography. Material undergoing mild wear often presents a smooth region, shallow delamination and very fine wear debris (< 100 nm), while a severe worn surface exhibits rougher region and larger wear debris [84], [87]. The initial stage of wear is often termed running-in, corresponding to the continuous growth of asperity junctions and enhancement of frictional compatibility. At this stage, wear rate will rapidly increase but stabilise after certain cycles when contacting area and stress condition reach equilibrium, i.e., so-called steady wear. Investigation of their mechanism is the key to avoid component failure and has recently drawn extensive attention [88]–[90]. Additionally, the wear coefficient K can also exhibit transitions, increasing by several orders of magnitude when tribological pairs operate at a specific sliding velocity or normal load conditions. For ductile metal under unlubricated condition, this critical value of K for the mild regime is below 10^{-4}~10^{-5} [84].

2.2.3 Adhesive and abrasive wear

Given a lot of experimental and modelling work, various wear mechanisms have been identified, depending on the circumstance and properties of the sliding pair. Herein, two main mechanical wear processes: adhesive wear and abrasive wear are reviewed in detail.

Adhesive wear is identified according to the adhesive force between tribological pairs with comparable mechanical properties, in which localised failure and adhesion of contacting asperities under shear result in a material transfer from the soft to the hard surface [82], [84]. From Archard's model, detachment of mixed asperities on the softer surface, are responsible for the generation of wear debris and contribute to the continuous material removal. The recent molecular dynamic simulation further reveals that the condition of detachment is associated with the critical touching length of the asperity junction. The larger value representing higher elastic energy is favourable to the formation of debris; otherwise, the smaller length retains plastic deformation locally [91], [92].

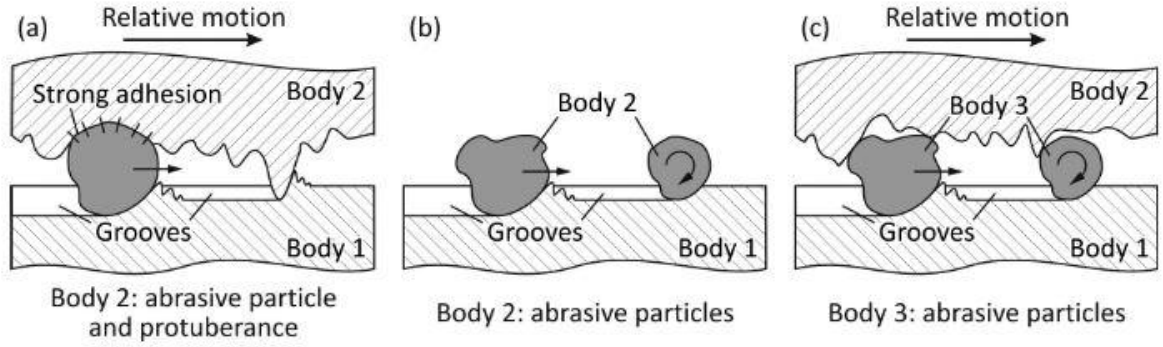

Fig.2. 11. *Schematic illustrations of wear mechanisms: (a-b) Two-body wear; (c) Three-body wear [93].*

Abrasive wear occurs when material removal results from a hard asperity or particles within the contact regime, which includes micromachining, ploughing and localized plastic deformation. It can be classified into two-body and three-body depending on the actual contacting situation. Fig.2.11 shows a schematic illustration of various abrasion mechanisms [93]. In the first two-body mode, the mixture of broken asperities or free particles similar to the hard protuberances has strong adhesion to the counterface, which could embed into the surface and cut deeply during rubbing. Thus, the surface after this two-body abrasion always presents grooves and a very high wear rate (Fig.2.11a). In another case, erosion, a second body from gas, liquid or solid impact on the surface, can also result in wear (Fig.2.11b) [82]. Moreover, the three-body mode presents free particles from surface detachment or externally introduced acting as abrasive particles (Fig.2.11c). The normal loading would introduce very high contact stress between particle and surface, often exceeding the crushing strength and result in plastic/brittle deformation of asperities. It should be noted that in erosion and three-body abrasion, the motion of free particles could either be sliding or rolling depending on the particle shape, size, as well as attack angle against the surface. Sliding corresponds to micromachining and ploughing, leading to a higher wear rate, while abrasive effects of rolling are much weaker.

It is also worth noting that the actual boundary between two-body and three-body in tribological pairs is indistinguishable because the generation of free particles is also related to the rigidity of the surface. Thus, high-stress and low-stress abrasion on the basis of crushing strength have been introduced to explain the abrasive process. High-stress abrasion results in

severe wear, while low-stress abrasion exhibits relatively fine scratches [82]. Lastly, although abrasion is not experienced in bearing components, the understanding of mechanical and chemical interaction between particles and surface plays a significant role in developing a new suspension for improving polishing technology.

Currently, the femoral head is usually made of fourth-generation ceramic, zirconia-toughened alumina, or the more traditional CoCrMo alloys [94]. The acetabular cup, femoral neck and stem are made from Ti alloys. Thus, there are three possibilities for the main contacting surfaces in an implant: ceramic-ceramic, metal-metal and ceramic-metal. Especially for ceramic-metal contact, the harder ceramic asperities may introduce plastic deformation on the softer metallic surface and further generate hard particles, which may accelerate material degradation and have the potential to cause inflammation after implantation [95]. Therefore, how to avoid harmful wear products and further enhance the lifetime of the implant becomes a considerable challenge for current researchers.

2.2.4 Fundamentals of lubrication

As an integral part of tribology, the purpose of lubrication is to reduce the friction force and avoid mechanical interaction of asperities via the formation of lubrication film between the contact surfaces. The form of lubricant is not limited to liquid, as solid and gas lubricants are also widely used in industry, such as graphite and helium [82], [84]. According to the thickness of lubricant film and surface contact mode, lubrication can be classified into hydrodynamic, elastohydrodynamic and boundary conditions.

In hydrodynamic lubrication, the lubricant film is thick enough (ranged from 1 ~ 100 μm) to separate asperities (Fig.2.12) [96]. This occurs when tribological pairs are in conformal contact with a small clearance, because the interfacial pressure is kept below a critical level and deformation of the surface is thus regarded negligible. In comparison, elastohydrodynamic often occurs in non-conformal contact geometry, such as opposing gear surfaces, which often have localised point or line contact. The elastohydrodynamic pressure would increase in response to the decreased area, which consequently reduces the thickness of lubricant film to below 1 μm, much thinner than that of hydrodynamic lubrication, and introduces elastic deformation of the softer surface. The distribution of pressure in these two conditions can be described by *Reynold* equations and is strongly linked to the working condition [82].

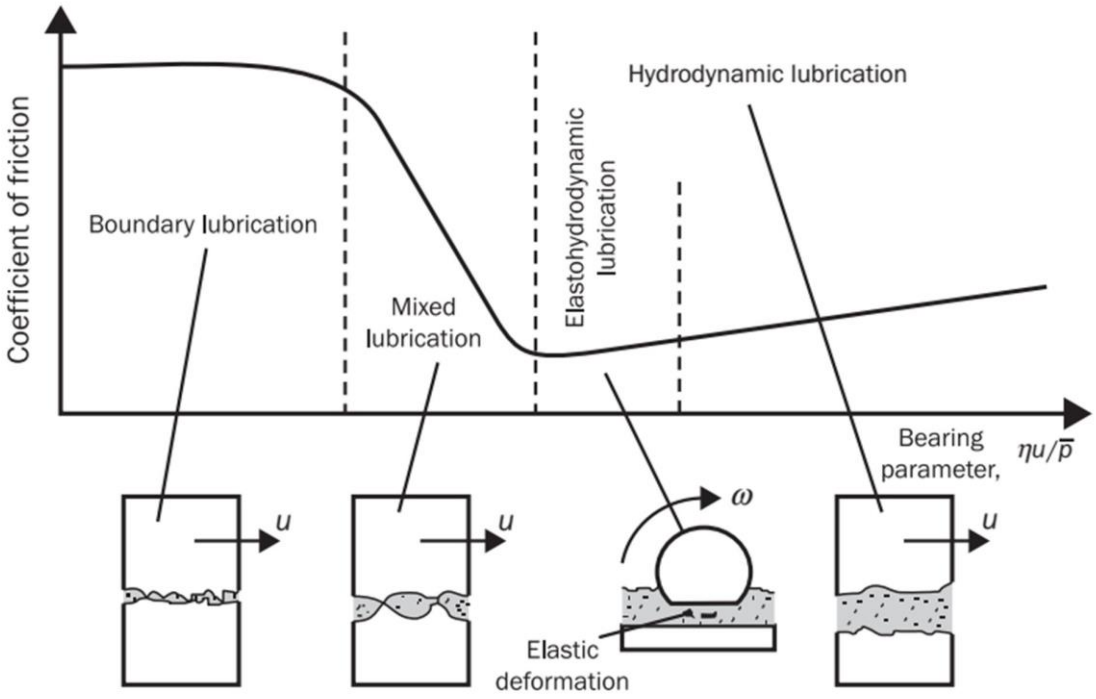

Fig.2. 12. *Stribeck curve and corresponding illustration of various lubrication conditions [96].*

As the lubricant thickness further decreases to less than the roughness (average height of asperities), lubrication becomes boundary lubrication, where asperities mechanically touch each other and a very thin lubricant film covers the surface recesses. In this case, the real contact area contributes much higher pressure and results in plastic deformation on the opposing surfaces.

Although the transition between lubrication regimes can be determined by the thickness of the lubricant film, it is difficult to carry out *in-situ* measurements. Therefore, the coefficient of friction μ is usually regarded as a crucial parameter to confirm the lubrication state. The evolution of μ depending on the bearing number: $\frac{\eta U}{P}$, also known as Hersey number, a dimensionless quantity including viscosity η, sliding velocity U and load per unit area P, can be illustrated via the *Stribeck* curve (Fig.2.12). High load, low viscosity and slow sliding velocity can break and reduce the lubricant film, leading to boundary lubrication [84], [96]. It is also worth noting that there is a mixed lubrication regime between boundary and elastohydrodynamic lubrication. Under this condition, coexistence of boundary, elastohydrodynamic and hydrodynamic lubrication occur, and the frictional force is mainly attributed to the combination of lubricant and plastic deformation, which explains why μ is sensitive to the *Sommerfeld* number.

2.2.4.1 Lubrication of metallic implants

In terms of lubrication in human joints, implants are surrounded by synovial fluid which is rich in albumin and various globulins, which together contribute to a concentration of protein in the

range from 10~30 g/L [97]. It is widely recognized that protein content is strongly linked to age and health condition; the elderly and people with the joint disease often have higher concentration because the filtration efficiency of protein via synovial membrane is decreasing [98]. Another important component of synovial fluid is hyaluronic acid, which has the disaccharide structure constructed of N-acetyl-glucosamine and glucuronic acid. These large molecules could interact with protein and significantly affect the viscosity, showing non-Newtonian fluid behaviour [98]. In other words, there is a positive correlation between shear rate and viscosity that also indicates the localised viscosity at the interface would largely change if undergoes any mechanical disruption.

The early investigations suggest that the lubrication mechanism in joints is dominated by fluid film lubrication because it well explains the superior lubricating properties of the joint [99]. However, this assumption ignores the actual loading condition during human body movement. Normal walking contains heel strike, toe off, leg flexion and extension, in which the variation of loading is consistent with the sine function. Thus, lubrication would change from fluid film to boundary lubrication due to the reduced lubricant film, and describing joint lubrication using the assumption of mixed lubrication is more reasonable [100].

2.2.5 Corrosion of biomedical Ti alloys in the human body

Corrosion is a significant issue in metallic implants, in addition to the mentioned organic compounds, synovial fluid could also be regarded as a kind of electrolyte solution consisting of alkali ions and chloride ions. Metallic implant would release metallic ions and stimulate

surrounding tissue after a long time [8]. Furthermore, it results in the failure of the metallic implant and increases the pain of the patients.

Basically, metallic corrosion describes chemical/electrochemical actions between metal and the surrounding medium, which would introduce damage or deterioration to the components [83], [101]. For active metals, the nature of corrosion can be directly evaluated by the dissolution of metallic atoms:

$$M \rightarrow M^{n+} + ne \qquad (2.7)$$

For passive metal, the active anodic dissolution is often accompanied by the formation of a metallic oxide film covering the surface of the metallic electrode (so-called passivation), which can be expressed as the following equation:

$$M + nH_2O \rightarrow MO_n + 2nH^+ + 2ne \qquad (2.8)$$

In Ti alloys, when the surface is exposed to an aqueous environment, the amorphous titanium dioxide (TiO_2) with a thickness around 1.5 -10 nm can be formed, which can be regarded as an electronic transfer barrier preventing further anodic reaction [102]. Thus, the dissolution rate of the substrate itself in many corrosive medias can be very low. This is why Ti alloys usually have excellent corrosion resistance compared to other metallic materials.

Additionally, in order to satisfy the equilibrium state, transferred electrons would be consumed via the following reactions, depending on the surrounding environmental conditions:

$$2H^+ + 2e \rightarrow H_2 \quad (2.9)$$

$$O_2 + 2H_2O + 4e \rightarrow 4OH^- \quad (2.10)$$

the generation of hydrogen with respect to equation 2.9 is usually observed in an acid environment, and oxygen reduction often occurs in aerated solutions. Considering the neutral and oxygen-containing environment in the human body, equation 2.10 is the main cathodic reaction of the metallic implant. Fig.2.13 schematically illustrates these interfacial events [81]. The formation of an electrical double layer due to released positive and negative ions are also highlighted.

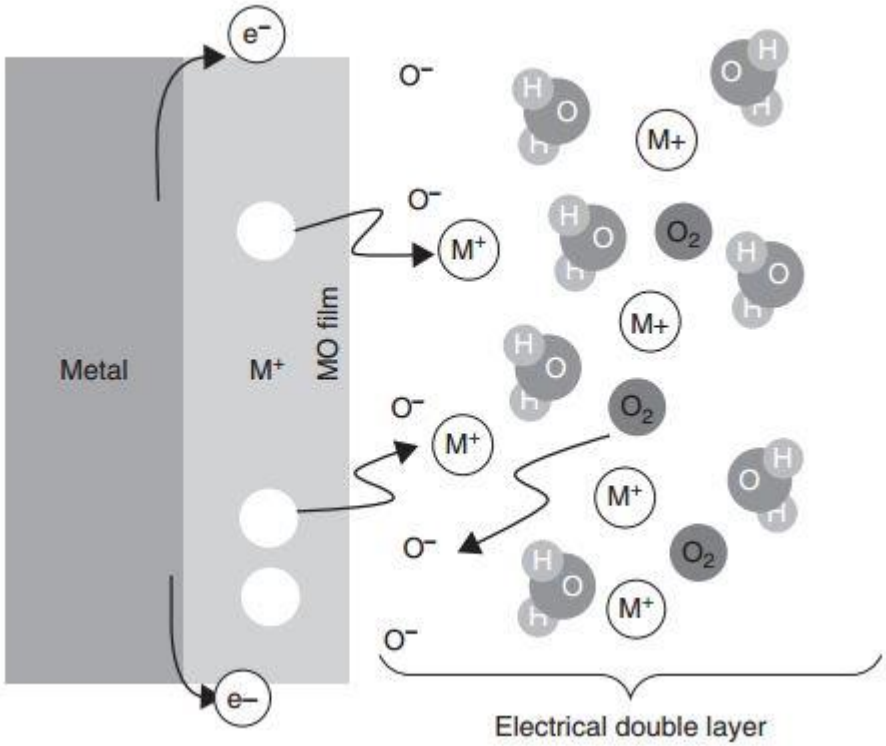

Fig.2. 13. *The interfacial circumstance of passive metal in human body [81].*

2.2.6 Synergistic effects of mechanical and chemical contributions to the total materials degradation in implant

Obviously, the total wear loss should be described with respect to the mechanical and chemical damage. However, the straightforward sum of them is not enough to quantitatively represent the nature of materials degradation. As illustrated in Fig.2.14, mechanic material removal not only generates wear debris but also exposes the fresh surface of the substrate to the aqueous environment, leading to their secondary corrosion [103]. In 1994, the first standard guide (ASTM G119) was proposed by Madsen to determine the wear-corrosion synergism [104], [105].

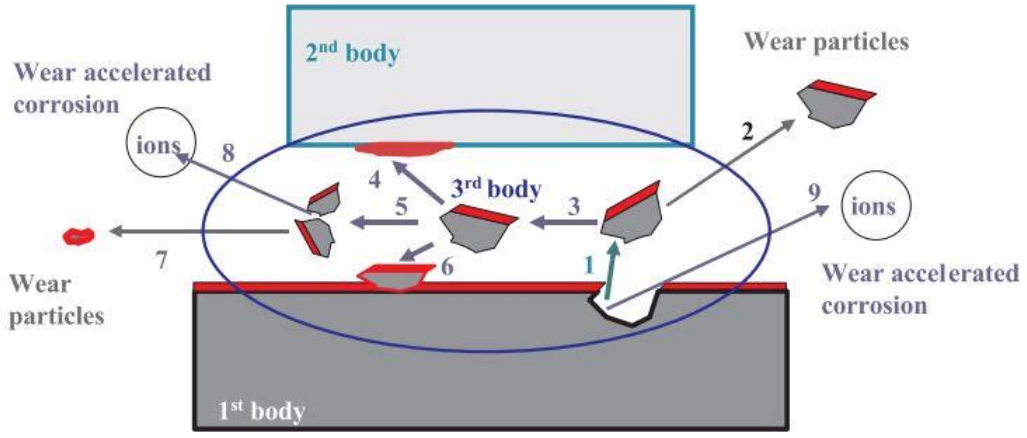

Fig.2. 14. *Schematic illustration of synergistic relationship in tribocorrosion [103].*

The total volume of materials degradation (T) is separated into three parts: material loss due to pure mechanical disruption (W_0), chemical materials degradation (C_0) individually and synergy between wear and corrosion (S):

$$T = W_0 + C_0 + S \qquad (2.11)$$

The synergistic factor S can be further described as the sum of wear accelerated corrosive degradation (ΔC_w) and corrosion accelerated mechanical degradation (ΔW_C):

$$S = \Delta C_w + \Delta W_C \quad (2.12)$$

Then, equation 2.11 can be rewritten as:

$$T = W_0 + C_0 + \Delta C_w + \Delta W_C \quad (2.13)$$

Therefore, the total chemical degradation C_w is attributed to $C_0 + \Delta C_w$, and total mechanical degradation W_C is attributed to $W_0 + \Delta W_C$.

This method describes the synergistic interaction between wear and corrosion. Current experimental limitations mean that data is only collected individually, which means that at least extra three measurements are required to understand the system fully. C_0 and C_w can be determined via electrochemical tests without and with wear respectively. Furthermore, wear under cathodic protection suppresses oxidation, and the resulting material loss can be regarded as W_0.

However, it was reported that cathodic potential would embrittle 304 stainless steel surface due to the absorption of hydrogen, deteriorating abrasive wear and result in accelerated material loss [106]. Bidiville [107] also compared the initial structural evolution of 316 steel surface

under cathodic and anodic potential. TEM results confirmed that the formation of dislocation cell structure underneath the surface enhanced the wear resistance. On the contrary, the passive film is responsible for the stress-induced martensite and blocking of dislocations. Thus, it still remains challenging to increase confidence in the data when using this synergistic method.

Additionally, another mechanistic model developed by Uhlig has simplified total materials loss (V_{total}) into two components: mechanical wear (V_{mech}) and wear accelerated corrosion (V_{chem}) [108]:

$$V_{total} = V_{mech} + V_{chem} \tag{2.14}$$

Herein, V_{total} can be determined through optical or mechanical profilometry. V_{chem} is calculated using Faraday's law:

$$V_{chem} = \frac{Q \times M}{n \times F \times \rho} \tag{2.15}$$

Where Q is electric charge flowing through the electrode consistent to the area of measured current versus time, which can be given by their integration, M is the equivalent weight of the metal in a unit of g/mol, n is the number of valence electrons for metallic ion, F is the Faraday constant (96490 mol^{-1}), ρ is the bulk density. For V_{mech}, the current experimental technique cannot measure and usually given by subtracting the V_{chem} from V_{total}.

As previously suggested, the ratio of V_{chem}/V_{mech} could be performed as a benchmark to determine the dominant mechanism of materials degradation during tribocorrosion, in which $V_{chem}/V_{mech} < 0.1$ corresponds to wear mechanism, $0.1 < V_{chem}/V_{mech} < 1$ corresponds to wear-corrosion mechanism, $1 < V_{chem}/V_{mech} < 10$ corresponds to corrosion-wear mechanism and $V_{chem}/V_{mech} > 10$ corresponds to corrosion mechanism [109]–[111].

2.2.7 Electrochemical techniques for investigating tribocorrosion of Ti alloys

Currently, one of the widely used electrochemical techniques to characterise the tribocorrosion process of Ti alloys is open circuit potential (OCP, E_{ocp}) measurement. E_{ocp}, also termed the free potential or spontaneous potential, is essentially a mixed potential representing the kinetics of anodic and cathodic reactions without any applied potential or current [112]. After immersion in an aqueous solution, monitoring the evolution of E_{ocp} versus time at static conditions could provide information about the thermodynamic tendency of surface oxidation. As previously suggested, E_{ocp} of Ti alloys would firstly shift towards the positive regime, corresponding to the spontaneous formation and growth of the passive layer. After that, E_{ocp} stabilises around a constant and a more positive value represents a better ability of passivation [113]–[115].

Additionally, for passive metals, E_{ocp} measurements during mechanical disruption are also widely performed to investigate wear-corrosion evolution because it is regarded as the closest to the actual condition [81]. A standard experimental procedure consists of three steps: E_{ocp}

stabilization prior to loading, loading and unloading [116]. Upon initial disruption, the stabilised potential would rapidly drop, consistent with the breakdown of the passive layer. During sliding, removal of the passive layer exposes the substrate to the media, which generates galvanic coupling between the worn and unworn regions. Thus, fluctuation of the potential can reflect the dynamic depassivation and repassivation process. It should be noted that this depassivation can be partial or complete depending on the magnitude of normal force and sliding speed. In general, the evolution of E_{ocp} can be determined by the following four parameters [116]–[119]:

- The intrinsic E_{ocp} of worn and unworn regions.
- The contact area, in other words, the ratio of worn and unworn regions in real-time.
- The relative position of worn and unworn regions.
- The kinetics of anodic and cathodic reactions.

After sliding, the surface will tend to recover to the static condition and potential shifts to a positive regime close to the stabilized E_{ocp}.

Another common electrochemical technique is potentiodynamic polarisation, which is often used to examine the passive behaviour of metals in static condition. Fig.2.15 presents a typical scanned curve of passive metals, within the anodic scan, the metallic electrode firstly undergoes an active region, where the log current density is proportional to the potential, following the well-known Tafel Equation [120]. Combined with the cathodic part, the current density (I_{corr}) and corrosion potential (E_{corr}) can be obtained via the Tafel extrapolation method. The next thing that happens is that the surface starts to initialize passivation, but it takes place in the

form of an anti-proportionality relation between potential and current density. The starting marking point is defined as the primary passivation potential (E_{pp}) and critical current density (I_{cc}). Then, a steady passive current (I_p) can be obtained not affected by increasing potential, indicating the formation of impact and dense passive layer. Furthermore, this protection would be invalid if the potential reaches the breakdown level.

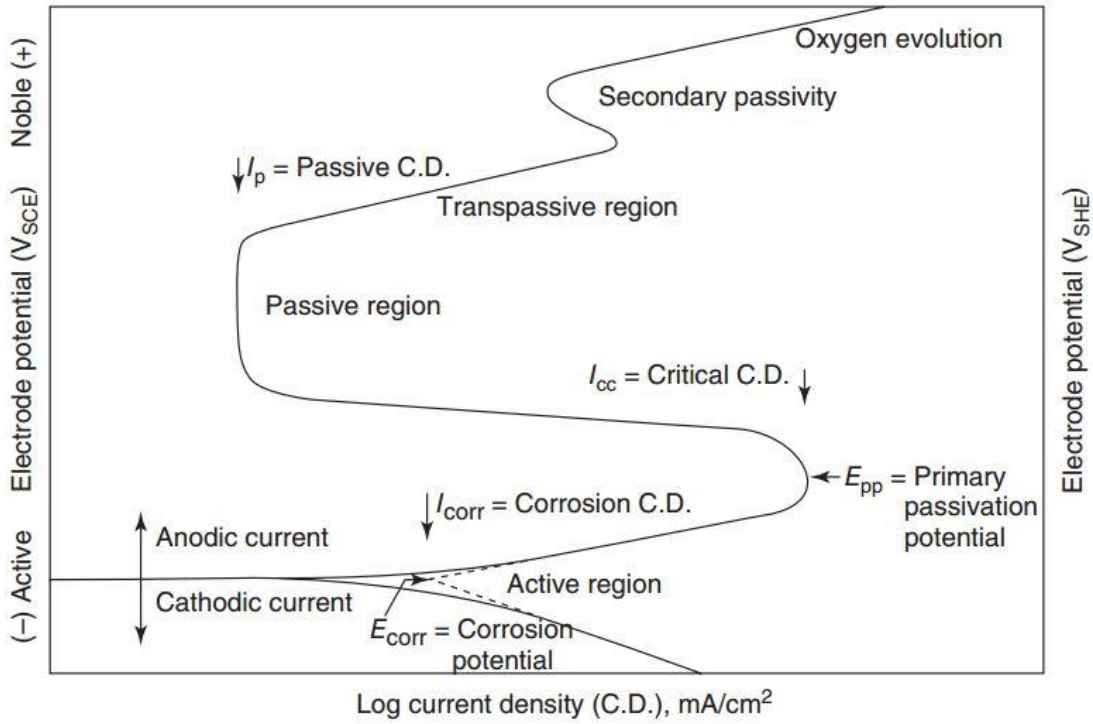

Fig.2. 15. *Tpical regions and parameters in polarisation curve (from ASTM G3) [117].*

2.2.8 Critical evaluation of current tribocorrosion of biomedical Ti alloys

To establish the actual physiological surrounding, investigations of corrosion resistance or tribocorrosion behaviours of biomedical Ti alloys are always conducted in simulated human body fluid (SBF), such as Ringer's and phosphate buffered solution (PBS). Considering only 5-6 mL synovial fluid in the human body, it is unrealistic for tribocorrosion tests to require a

hundred millilitres of lubricant. Thus, the addition of animal serum, especially bovine serum albumin (BSA), including calf and newborn calf serum in SBF, is widely used to achieve similar protein concentration [121].

Contu et al. [112], [122] compared tribocorrosion response of Ti-6Al-4V alloy in buffer solution and buffer solution with BSA at different pH, under OCP potential. It was found that the presence of protein had negligible effects on the rubbing potential but performed as a corrosion inhibitor, in which the absorption of BSA on the surface slowed down both cathodic and anodic reaction, resulting in a lower E_{corr} and repassivation rate. Similar results were also observed in Karimi's study [123]. The increasing concentration of BSA lowered the stability of passive film near the surface, leading to a weak polarisation resistance and a more negative E_{ocp} at static condition.

Another interesting phenomenon is the formation of a tribofilm. Yazdi et al. [124] investigated the tribocorrosion of Ti-6Al-4V after oxidation treatment. The tribofilm with a thickness of 200 nm was observed on the surface. Energy Dispersive Spectroscopy and X-ray Photoelectron Spectroscopy confirmed the film consisted of oxide from the alumina counterparts and substrate, i.e., Al_2O_3 and TiO_2, indicating a synergistic reaction between contact surfaces and lubricant. A hard TiN coating has also been demonstrated to provide superior wear performance compared to the metallic substrate [125]. However, they have a risk of de-adhesion, which may result in unacceptable failure of the implant.

Currently, more information about factors affecting the formation of tribofilm in Ti alloys is rarely reported and still unclear. But according to previous similar studies on CoCrMo alloy,

the formation of this organic layer is strongly related to surface finish. Zeng et al. [126] found CoCrMo surface after mechanical polishing presented much thicker tribofilm compared to the electropolished surface. It also revealed that the mechanically polished sample had a larger specific wear rate, suggesting weak protection of tribofilm.

Also, quantitatively determining synergism of tribocorrosion under OCP is challenging because the integration of current flow is zero, and rubbing potential depends on the kinetics of the active worn surface and the passive unworn surface, i.e., mixed potential. Jensen et al. [127] used epoxy coating to cover the unworn part when testing stainless steel at OCP. It had been observed that a potential drop of the coated surface shifted to a more negative region. To further examine current flowing inside worn surface, Espallargas et al. [128] proposed a new experimental set-up on the basis of zero-resistance ammetry (ZRA), in which two working electrodes (two samples) were prepared. One electrode ready for sliding was covered with an insulating coating performing as the anode while another electrode was the cathode. Thus, the galvanic current could be measured to calculate real V_{chem} during tribocorrosion [129].

It is worth noting that most reported tribocorrosion experiments of biomedical Ti alloys fall into the region of severe wear, presenting classic feature of abrasion and adhesion: inhomogeneous distribution of wear debris, delamination and abrasive grooves. Meanwhile, there are still some factors limiting the outcomes of the experimental works. Firstly, the bovine serum does not follow non-Newtonian behaviour, which means the viscosity of the lubricant has the potential to rapidly decrease during sliding, leading to the reduced lubricant film, as well as the transition of lubrication mode. And, the actual protein concentration of the testing

solution is not constant due to the batch problem, affecting the experiment repeatability [98]. Secondly, the degradation of the protein limits the testing time only within a few hours, which cannot validate the long-term capacity. Lastly, Ti alloys are very easy to catch hydrogen in an aqueous solution, especially for open bcc structure such as beta Ti alloys. Therefore, tests at cathodic potential can introduce error into the synergistic calculation due to surface embrittlement, and it is still unclear whether ASTM G119 is suitable for a protein-containing system [105].

2.3 Improved Tribocorrosion Performance via Laser Surface Texturing

2.3.1 Introduction

Nature has always been the source of various scientific principles and major inventions of mankind since ancient times. The development of aircraft is perhaps the most representative example of biomimicry. Traceback to 400 BC, Archytas of Tarentum, a mathematician and philosopher firstly invented a mechanical pigeon, which establishes the milestone of humans to conquer the sky. Then, from Da Vinci's aircraft design drawings to Wright brothers' first flight, although it takes almost 500 years, there is no doubt that 12 second and 36.6 meters have an extraordinary significance and would be one of the most remarkable achievements in human history.

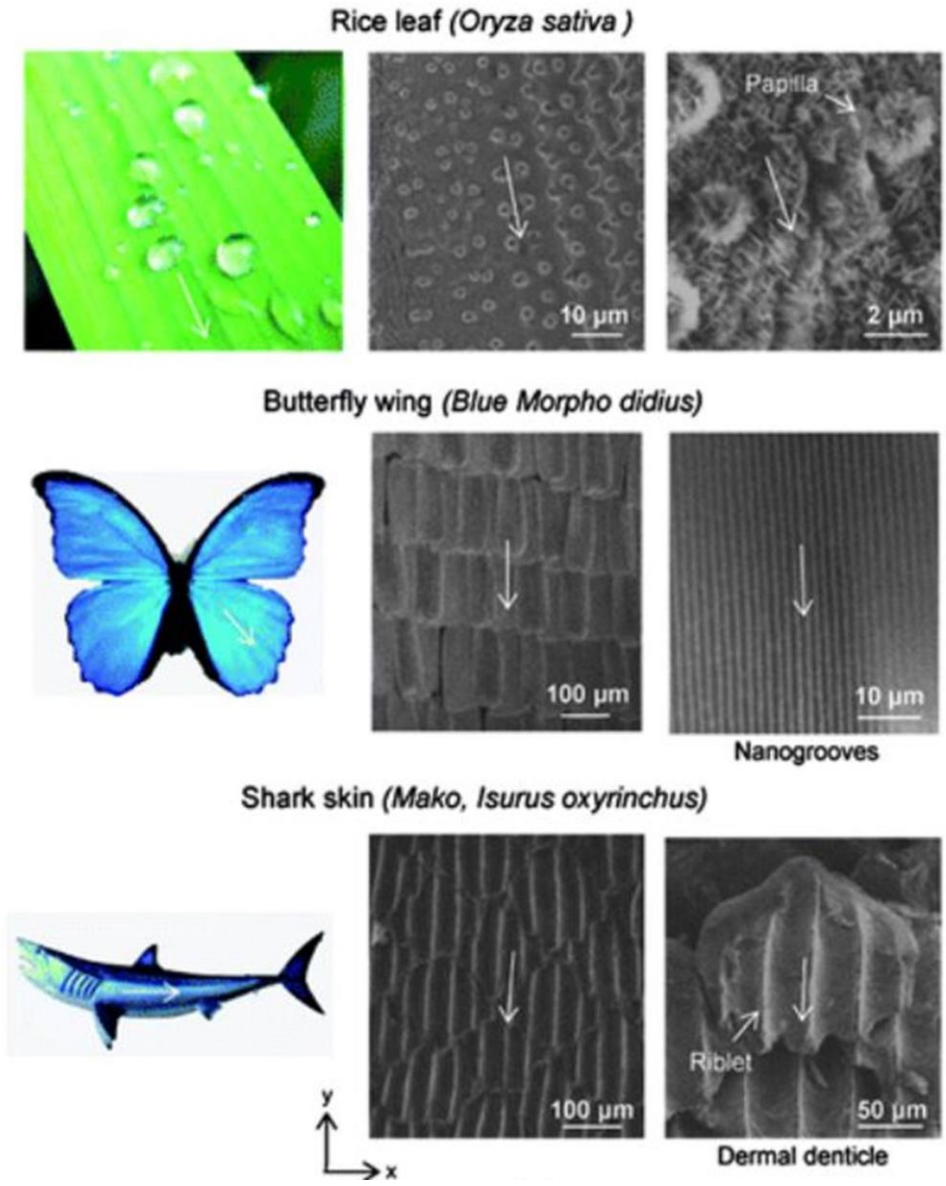

Fig.2. 16. *Surface texture found from rice leaf, butterfly wings and shark skin. Their corresponding SEM images under different magnifications are also presented [131], [132].*

Learning living nature has also attracted extensive attention in materials science, especially in modifying surface structure. Some nature-inspired textures are widely used to introduce a revolutionary solution to industries, which increases the multifunctional integration and reduces energy consumption [130]. Herein, three typical cases are demonstrated in Fig.2.16 [131], [132]. Rice leaf and butterfly wing can realize superhydrophobicity and self-cleaning

(also termed as lotus effect) through the periodic arrangement of micro-scale papillae and grooves, which could decrease contact angle resulting in a lower surface adhesion force. The formation of smaller riblet-like feature in sharkskin can block fluid vortex translation, which reduces the probability of vortex ejection and transfer on the boundary, leading to drag reduction.

Currently, methods to realize texturing includes lithography, etching, electrochemical/mechanical micromachining, ion milling, laser ablation and remelting. Compared to other techniques, precise and high-speed energy beams could realize nanofabrication and promise both high precision and output efficiency [133]–[136]. In this section, two main laser methods to manufacture surface texturing as well as their effects on tribological performance, are reviewed in detail.

2.3.2 Laser texturing via material ablation

A laser can be emitted either in a pulsed or continuous beam. It is apparent that well-controlled pulsed radiation would lead to the instantaneous accumulation of high energy. For metallic material, it should be noted that relatively high thermal conductivity in contrast to ceramic and composite brings challenges to perform surface modification with high precision. This process is firstly accompanied by the absorption of electrons leading to lattice heating. Generally, the electron cooling time is in the order of 1 ps, and heat transfer in the lattice usually needs 10~100 ps. Thus, the material would directly evaporate without melting if the pulse time is shorter than the cooling time (Fig.2.17a).

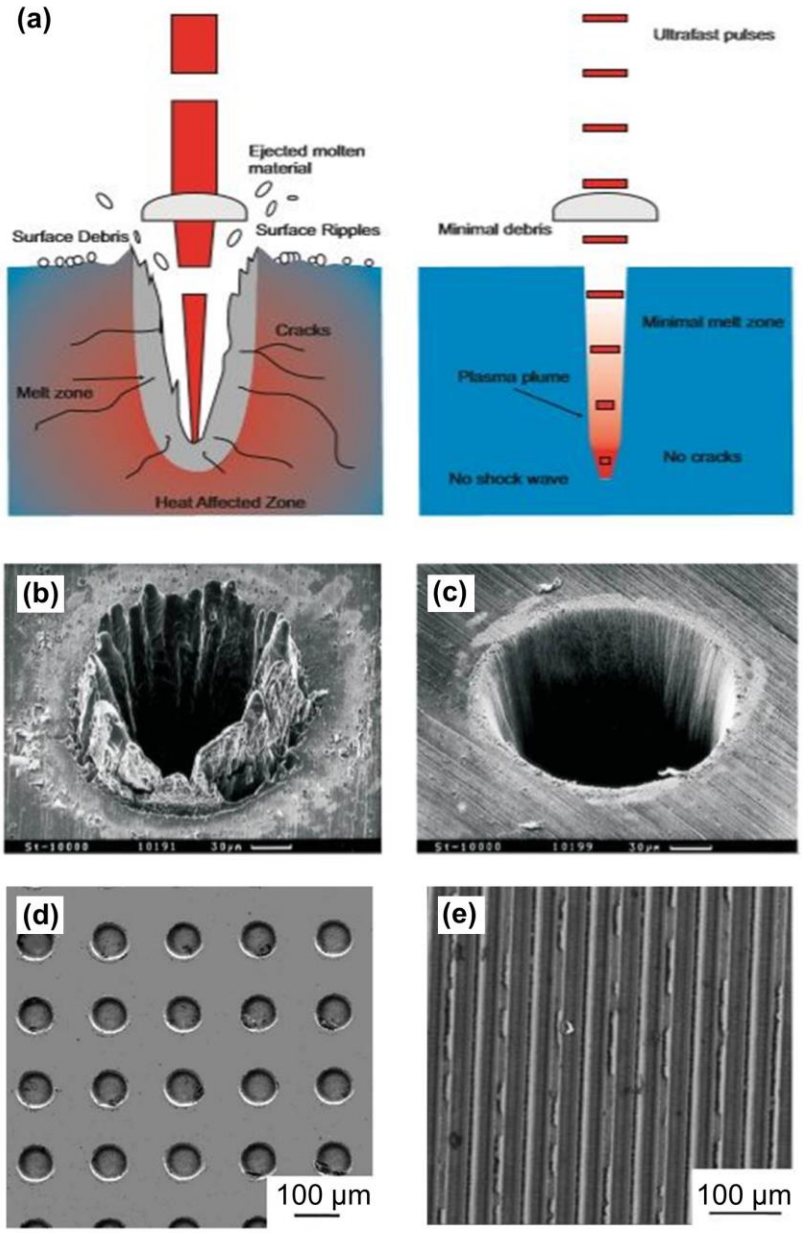

Fig.2. 17. *(a) Schematic illustration of laser ablation process at different wavelength; (b-c) Magnified SEM micrographs of textured steel after femtosecond and nanosecond laser ablation respectively; SEM micrographs exhibiting recent developed dimple (d) and linear texture of Ti64 alloy [134] [135].*

On the other hand, the thermal process occurs if the pulse time is longer (usually of the order of ns), in which the formation of thermal cracking and a heat-affected zone (HAZ) would be observed [134]. As illustrated in Figs.2.17b-c, steel after 3.3 ns laser process has a much rougher surface finish than the same sample textured with 200 fs laser [135]. Additionally, recoil pressure mainly driven by the combinatorial effects of the molten phase and evaporation can result in liquid ejection that can favour debris formation on the surface after solidification. Thus, to achieve high precision, an ultrashort pulse laser is preferred.

Currently, a dimple geometry is widely used in metallic materials for tribological application [137]. It was reported that dimple textured Ti64 showed better wear resistance compared to the untextured sample under dry sliding condition [138], [139]. The decreased friction coefficients were observed in textured samples with higher dimple density. It was mainly attributed to the dynamic entrapped process of wear debris in dimples, which acted as a disincentive to abrasive wear. Additionally, it should be pointed out that the difference in wear rate between textured and untextured samples was not obvious, and the reason for this will be discussed later. In terms of biocompatibility, polarisation tests of textured Ti64 samples in Hanks's solution revealed a decreased corrosion rate and nobler electrochemical behaviour, which indicated an enhanced corrosion resistance. Immersion experiments suggested that textured topography had no toxic effects in comparison with untextured samples [138]. When sliding under lubricated conditions, Dipankar et al. [140] compared *in-situ* tribological performance between dimple textured and as-polished CrCoMo alloy in a hip simulator. It was observed the square dimple was favourable to increase the thickness of the lubricant film to as high as 795 nm. Therefore,

it could be concluded that this laser texture plays a significant effect in altering the tribological properties of metallic materials. The recesses may act as a lubricant and debris reservoir during tribological contact.

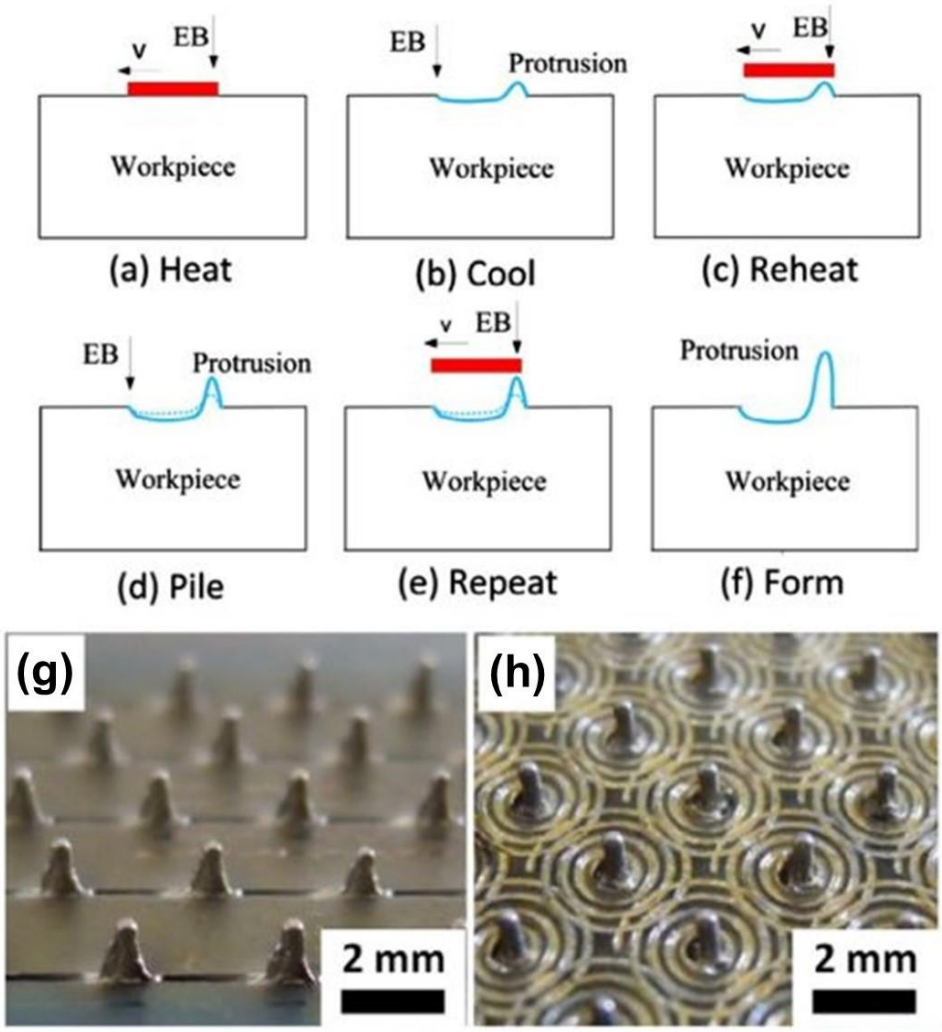

Fig.2. 18. *(a-f) Schematics illustrating the formation of protrusion in Surfi-Sculpt process; (g-h) Optical images of Ti64 after Surfi-Sculpt treatment [141] [142].*

2.3.3 Laser texturing via material remelting

Continuous laser wave is another tool to modify surfaces. Different to the material removal realizing texture in laser ablation, there is no material loss in this process, and the materials are

always at thermal equilibrium. Currently, two remelting techniques based on this mechanism are widely used and reported. One is the Surfi-Sculpt© process developed by The Welding Institute (TWI, GB) [141], [142]. In this method, a laser or electron beam is scanned over the surface at high speed, repeating the same scanning route, which leads to the redistribution and the acceleration of material flow at the beginning of the track (Figs.2.18a-f). The size can be tuned from the micro to millimetre scale by changing processing parameters or the number of scans. As illustrated in Figs.2.18g-h, a high aspect ratio spike is the most popular example and a very good candidate for joining application, such as bonding of polymer to the metal component. Another method is termed WaveShape, in which a modulated laser beam is used to redistribute the molten material (Fig.2.19a) [143]. More specifically, the resultant texture is mainly attributed to the deformation of the molten pool, also known as the Marangoni effects [144]. Tension variation is inversely proportional to the temperature gradient derived from the interaction between laser and material surface, which can result in thermal Marangoni convection/vortex promoting the fluid movement to form a protruding structure. In other words, this technique enables a decreased roughness, but at the same time, increases waviness of the surface by generating periodic features. As shown in Figs.2.19b-c, the well-controlled laser beam and scanning route generate annular texture on the Ti64 surface. When comparing the efficiency of laser ablation and laser remelting, the building efficiency of remelting for metallic materials (17.6 mm^3/min) is much higher than ablation (10 min/cm^2), which is believed to be more economical in actual application [143], [145], [146].

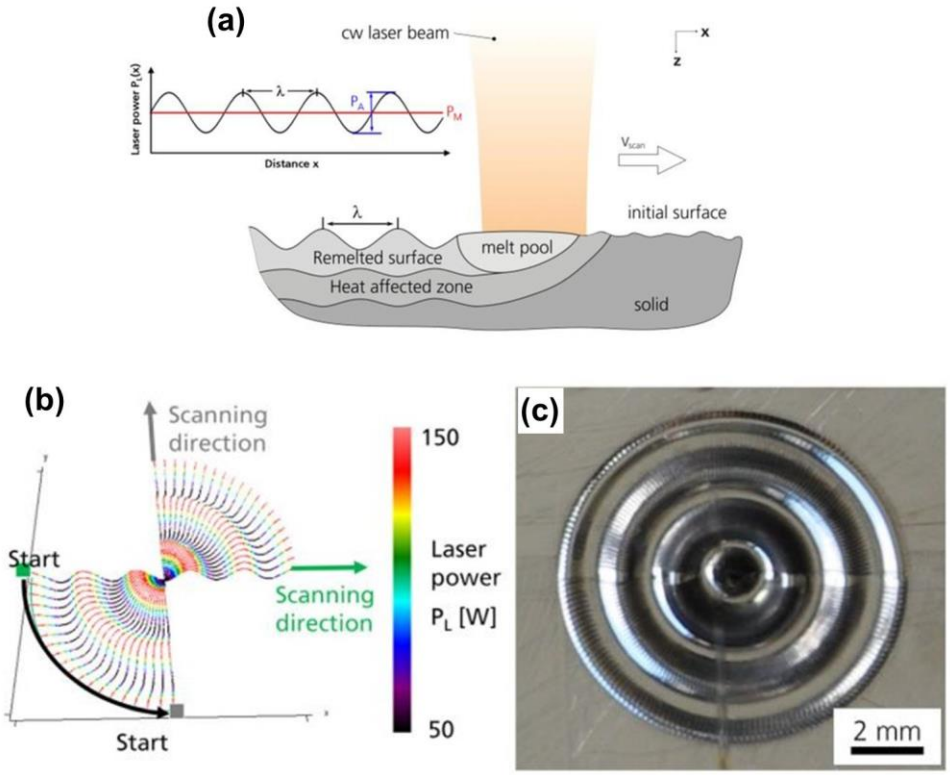

Fig.2. 19. *(a) Schematic diagram of WaveShape process; laser processing map (b) and optical image of received texture on Ti64 surface [143].*

2.3.4 Critical evaluation of laser texturing on Ti alloys for orthopaedic applications

To sum up, current laser texturing on metallic components for orthopaedic applications still remains difficult and challenging. For ablated geometries they cannot promote a completely smooth surface finish, which may introduce localized high-stress concentration due to non-conformal contact, leading to debris formation [147]. As mentioned above, although dimple or channel texture can lower friction coefficient, the formation of wear debris and corresponding mechanical accelerated wear still occurs. The texture has the possibility to be exhausted or worn away after a certain time. Thus, the ablated texture is still unacceptable in the field of implants requiring superior tribocorrosion performance. In contrast, it seems that laser remelting can provide a much better surface finish; more importantly, the rapid solidification is favourable to the refinement of microstructure, which gives a solution to the possible increasing stress in tribological contact. However, it can be found that the current design of geometry is very large, subject to the laser beam diameter (>200 μm). And, there are no related articles concerning their effects on tribocorrosion behaviour. Therefore, from the author's point of view, it would be an interesting story to design texture with improved mechanical properties using a refined laser beam, which may change the wear mechanism from three-body to two-body abrasion and has unusual significance for substantially increase the service life of implants.

2.4 Summary of the Literature Review

Developing new Ti alloys for orthopaedic applications requires a comprehensive understanding of several cross-disciplinary subjects. Recent investigations on designing new composition, deformation behaviour, tribocorrosion performance and surface modification have been reviewed and discussed in detail. Beta Ti alloys present lower stiffness and exhibit novel deformation, the extent of which depends on the β-phase stability. However, two main challenging questions remain for researchers. The first is how to design new Ti alloys with both low Young's modulus and high strength. The second is how to improve the tribocorrosion performance of Ti alloys and further enhance the lifespan of the implant. The majority of current studies have just been on CoCrMo alloys. In contrast, the bio-tribofilm formation on Ti alloys and the evolution of the subsurface during tribocorrosion are not fully understood. Studies are then needed to contribute to these topics.

Chapter 3 Methodology and Experimental Procedures

3.1 Introduction

Three metastable Ti-Mo based alloys: Ti-4Mo-Fe-3Sn, Ti-5Mo-Fe-3Sn and Ti-5Mo-Fe-4Sn (at.%) were developed based on d-electron, average valence electron concentration and Mo equivalent number. These alloys are hereafter denoted Ti413, Ti513 and Ti514, respectively. Details of composition design, alloy preparation and subsequent characterisation are summarised as follows.

3.2 Composition design

The majority of alloying elements used in biomedical Ti-based alloys are Al and V, which are considered highly cytotoxic and can increase the failure risk of implants. Especially for orthopaedic implants requiring a longer lifespan, the material-tissue interaction can introduce material degradation depending on environmental conditions and contacting mode. Therefore, it is important to select elements with low metal sensitivity when designing new composition. This is why non-toxic elements, such as Nb, Ta and Mo, are widely used in biomedical titanium alloy design [148]. Herein, we aimed to design an alloy with both low Young's modulus and superior mechanical properties with relatively cheap alloying elements. Compared to Ta and Nb, the stronger beta stabilising effect of Mo could result in a lower cost in terms of raw materials. However, considering their little effects on mechanical performance, i.e., yield and tensile strength, the eutectoid promoting element Fe was chosen and expected to activate the

solid solution strengthening effect, as well as enhanced wear resistance. Meanwhile, neutral elements (Zr, Hf and Sn) could also decrease Young's modulus by suppressing the formation of athermal ω phase [7], [37], [149]. On the basis of these concepts, a group of Ti-Mo-Fe-Sn alloys were developed, and their electronic parameters are shown in Table 3.1.

Table 3. 1 *Designed compositions of calculated parameters.*

Composition (at.%)	$\overline{Bo}$	$\overline{Md}$	e/a	K_β	Mo_{eq}
Ti-4Mo-Fe-3Sn	2.402	2.784	4.12	1.04	10.07
Ti-5Mo-Fe-3Sn	2.398	2.787	4.14	1.21	11.80
Ti-5Mo-Fe-4Sn	2.394	2.782	4.14	1.21	11.65

The upper limit of 1% Fe was decided to avoid possible elemental segregation during high-temperature melting. Mo_{eq} and K_β were maintained around 1.00 and 10.00, respectively, which corresponded to the boundary between metastable and α+β structure. Average electron concentrations (e/a) were calculated to be in a range from 4.12 to 4.14, which corresponded to the theoretical minimum value of Young's modulus in Fig.2.8, where other metastable phases were completely suppressed [31]. Thus, in all designed alloys, a fully β microstructure with low Young's modulus was expected upon quenching [150]. The location of calculated $\overline{Bo}$ (mean bond order) and $\overline{Md}$ (mean molecular d-orbital energy level) in the $\overline{Bo} - \overline{Md}$ diagram (Fig.3.1) also indicated that M_s (martensite start temperature) was above room temperature (RT) while M_f (martensite finish temperature) was observed below RT, implying

that the deformation mechanism of all alloys should be dominated by a combined TRIP and TWIP effects.

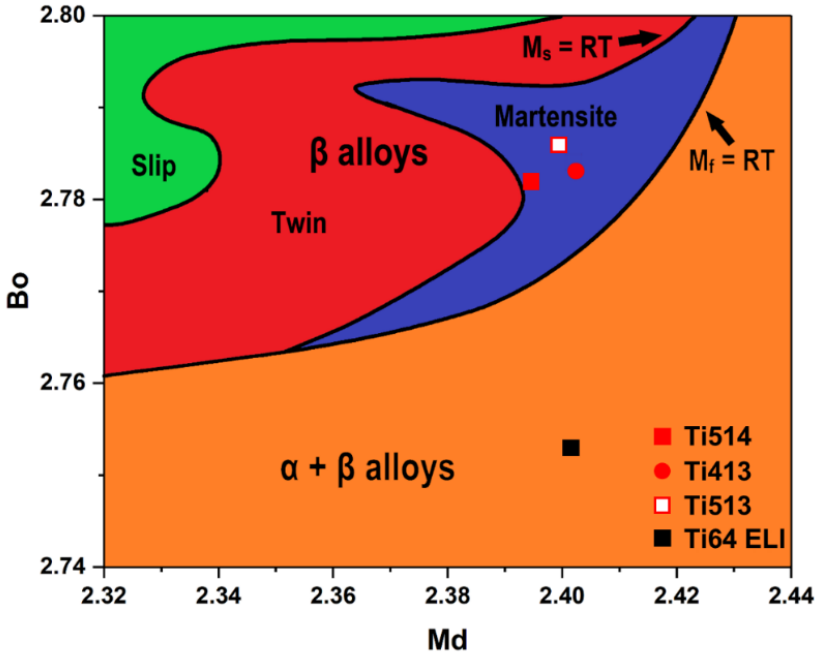

Fig.3. 1. *The position of Ti413, Ti513, Ti514 and Ti64 ELI in d-electron design map.*

3.3 Alloy preparation

3.3.1 Arc melting

All designed metastable Ti alloys were prepared through a non-consumable arc melter (Arc200, USA) in a high-purity argon atmosphere. Raw materials were pure titanium plate (Ti 99.6 wt.%), molybdenum plate (Mo 99.8 wt.%), iron chips (Fe 99.9 wt.%), and tin rod (Sn 99.8 wt.%). Prior to melting, the oxide layer on the raw materials was gently removed using 800 grit SiC grinding papers and then ultrasonically cleaned in isopropanol for 10 minutes. The total weight of each composition was 80 g and accurate to 0.001 g. The copper mould was connected to a water-chilled system which provided a high cooling rate during solidification. The chamber was then evacuated to 3×10^{-5} Torr and backfilled with around 2/3 atmosphere

of pure argon gas. Considering the large difference in melting point between Mo and Sn (3396 K and 505 K, respectively), the small Sn pieces were placed at the bottom of the mould, completely covered by the Ti slices, which prevented weight loss due to evaporation of Sn. During melting, in order to realize elemental homogenization, the ingots were flipped and re-melted at least five times under a magnetic stirring system. The weight loss of each specimen during preparation was controlled less than 0.1 wt.%.

3.3.2 Thermal-mechanical processing

The as-melted ingots were firstly homogenised at 1373 K for 2 hours under flowing argon and hot rolled into a 4 mm-thick plate with a reduction of per pass ~ 50% at 1273 K, followed by water quenching. Subsequently, the received plates were further cold-rolled into a 2 mm-thick plate with a reduction of 50%. As-rolled specimens were annealed at 1173 K for 10 minutes,

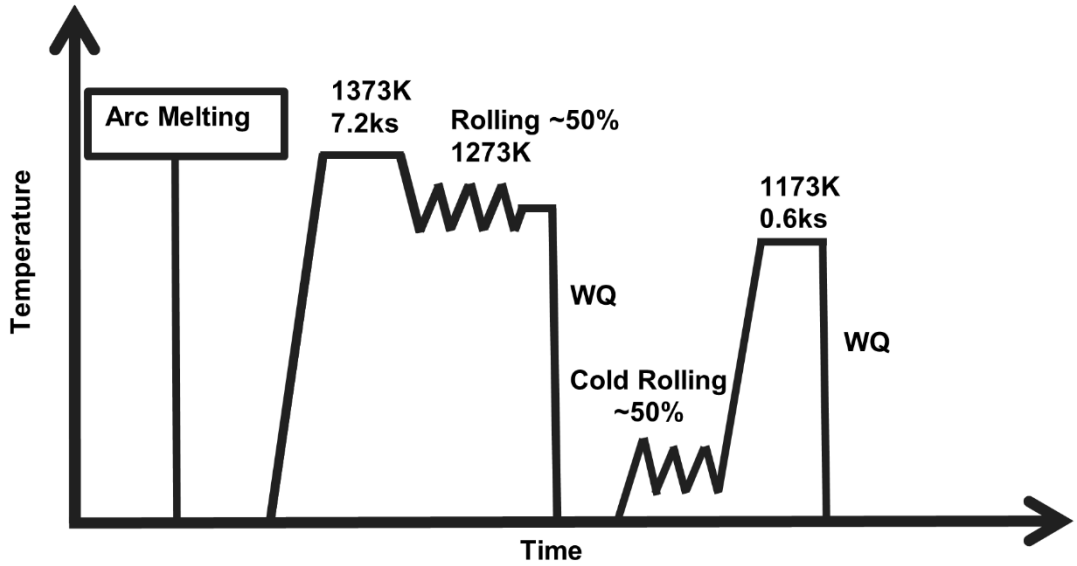

Fig.3. 2. *Schematic of the thermal-mechanical process.*

followed by water quenching. Fig 3.2 briefly illustrates the above thermomechanical processing route.

3.3.3 Benchmark material

A plate of annealed Ti-6Al-4V ELI (ASTM F136, Grade 23) bought from Ti-shop (UK) with a dimension of 250 mm × 250 mm × 4 mm was employed as a benchmark material. Hereafter, denoted Ti64 ELI.

3.3.4 Mechanical polishing

In this study, all flat samples with different dimensions were cold mounted into epoxy resin and followed by three-step metallurgical polishing procedures:

1. Firstly, plane grinding using 400 grit SiC papers to achieve a flat surface.
2. Then, fine polishing on MD-Largo cloth (Struers, USA) with 9 μm diamond suspension to ensure scratches get rid of completely. It was noted that the MD-Largo cloth should be lubricated with water in advance, preventing agglomeration of suspension during polish.
3. Lastly, a mirror-like surface can be acquired through polishing on MD-Chem (Struers, USA) with a final 0.5 μm colloidal silica suspension containing 20 vol.% H_2O_2. To avoid suspension residues on the surface, which may affect further characterisation results, all as-polished specimens were water polished using a new MD-Chem plate for 5 minutes and subsequently cleaned in isopropanol by ultrasonic wave for 10 minutes.

3.3.5 Surface modification via selective laser melting (SLM)

Laser modification was carried out on a mechanical-polished surface through a continuous laser in a high-purity Ar atmosphere at a power of 130 W (Aconity Mini, USA). Gaussian refined laser beam had a focused spot size of around 65 μm, and scan speed was set to 3 m/s. The scanning pattern was established in a basic grid (the angle between X and Y directions was 90 degrees), in which hatching spacing distance was controlled ~ 200 μm along both scan directions.

3.4 Phase and composition characterisation

3.4.1 X-ray analysis (XRD)

Phase constitution analysis was conducted on D2 Phaser (Bruker Corporation) using average Cu-K_α radiation at 2θ angle ranging from 30° to 80°. The operating voltage and current were 30 kV and 10 mA, respectively. Note that standard pdf cards of metastable phases such as martensite and omega phases in Ti alloys are still under development. Meanwhile, the detection limit of the phase amount in XRD is around 2%, indicating that some diffraction peaks may not or fully appear on the pattern. Therefore, XRD analysis was conducted for a brief phase determination in this study.

3.4.2 Composition measurement

The composition was determined using an inductively coupled plasma method (ICP-OES instrument), and O content was analysed via infrared absorption (Leco ONH836 instrument).

3.5 Mechanical characterisation

3.5.1 Nanoindentation

Hardness and reduced Young's modulus mapping of the cross-sectional laser-treated surface were performed on a Hysitron nanoindenter (TI Premier, Hysitron, USA) equipped with a Berkovich diamond tip. The load was set as 10 mg, and dwell time was 15 s. Each map was composed of at least 30 indentations and measured three times to promote data accuracy.

3.5.2 Tensile test

As shown in Fig.3.3, flat dog-bone-shaped tensile specimens with a gauge dimension of 15 mm × 3 mm were prepared via Electrical Discharge Machining (EDM). Room temperature tensile tests were performed on a Zwick universal testing machine (Germany) at an initial strain rate of 3.3×10^{-4} s^{-1}. A laser extensometer was used to measure the strain, and the corresponding Young's modulus was calculated by classic Hooke's Law at the early stage of elastic deformation. Each composition was tested at least three times to demonstrate the repeatability of the data.

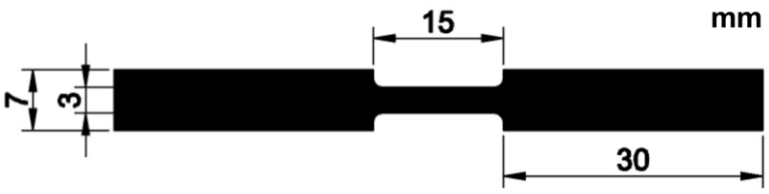

Fig.3. 3. *The dimension of a tensile sample.*

3.5.3 *In-situ* micro-pillar compression test

In order to investigate the difference of mechanical properties between the primary and laser-treated surface, micropillars with 2.5 μm in top diameter and a diameter-to-height ratio of ~1:3 were fabricated through a focused ion beam to conduct *in-situ* micropillar compression tests in an FEI Nova NanoSEM 450 scanning electron microscope. An Alemnis *In-situ* indenter with a 10 μm diamond flat punch was used, and all tests were performed at an axial strain rate of 1 $\times 10^{-3}$ s^{-1}. Prior to measurement, the average drift rate was stabilized below 0.1 nm $s^{-1,}$ and the total displacement of punch was 1.5 μm, equivalent to about 20% strain of compressive deformation.

3.6 Tribocorrosion behaviour characterisation

3.6.1 Lubricant (Electrolytes)

All tribocorrosion tests were carried out in phosphate-buffered saline (PBS) solution, containing 25 vol.% of new-born calf serum (BCS, supplied by Fisher Scientific, UK). One PBS tablet (1814.5-2005.5 mg) was firstly dissolved in 200 ml ultra-pure water (High-Performance Liquid Chromatography, HPLC, Sigma-Aldrich, UK) that yields 0.01 M phosphate buffer, 0.0027 M potassium chloride and 0.0137 M sodium chloride at room temperature. After that, the received solution was mixed with 50 ml BCS and followed by the addition of 0.4 g sodium azide to prevent protein degeneration. PBS solution with BCS can maintain the bioactivity of biomolecules and is more similar to the actual human body than Ringer's solution and Hank's solution [151].

3.6.2 Experimental procedures

Square discs with a dimension of 25 × 25 mm were cut from an as-annealed plate and followed by mechanical polish. Ball-on-flat reciprocating-sliding tests were carried out in a Universal Mechanical Tester (Tribolab, Bruker, USA) at a temperature of 37 ± 1℃. As shown in Fig.3.4, the sample was fitted into a three-electrode cell connected to a potentiostat. The sample, a pure platinum rod and an Ag/AgCl electrode performed as a working electrode, counter electrode and reference electrode, respectively. A Grade10 polycrystalline alumina ball with a diameter of 4 mm was chosen as a counterface. The stroke length was set 2 mm (imposed sliding amplitude), and a normal load of 0.5 N was applied. The specimen was rubbed at reciprocating frequencies of 2.5 Hz and 5 Hz. The total sliding distance was 216 m, corresponding to 54000 cycles. All tests were conducted under open circuit potential (OCP) mode.

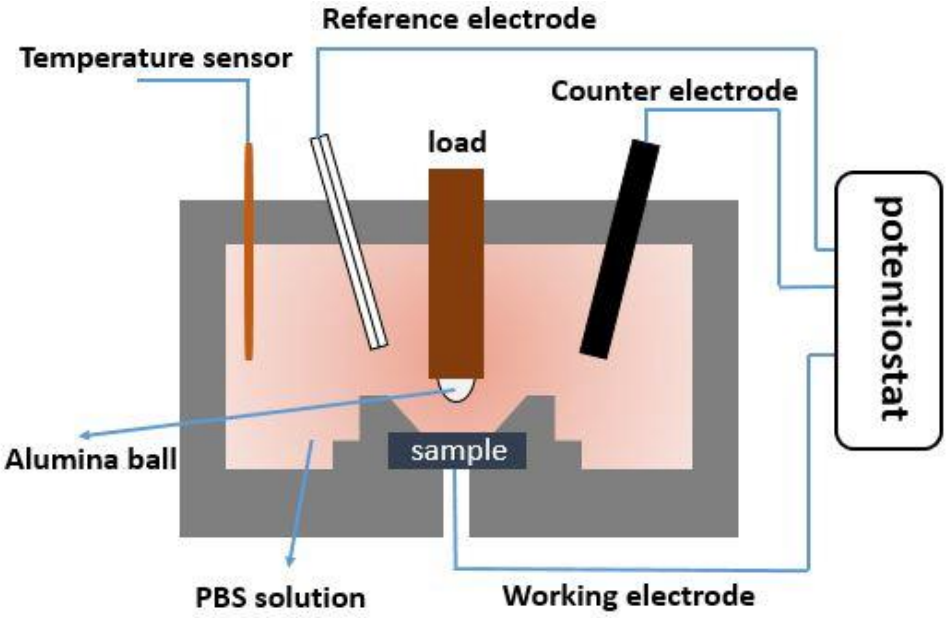

Fig.3. 4. *Schematic illustration of set-up of tribocorrosion experiment.*

Each experiment consisted of the following stages:

1. OCP stabilization for 1800 s before rubbing
2. Rubbing experiment for 10800/21600 s
3. Subsequent potential measurement for 1800 s when rubbing stopped
4. Repeated at least three times to ensure the repeatability of data.

3.7 Electrochemical characterisation

Electrochemical properties were evaluated by the open circuit potential and potentiodynamic polarisation. Each composition was repeated at least three times to promise data repeatability.

3.7.1 Open circuit potential measurement (OCP)

OCP (E_{ocp}) measurements of fresh samples were performed for 1800 s in the same cell (Fig.3.4), followed by potentiodynamic polarisation.

3.7.2 Potentiodynamic polarisation

Potentiodynamic polarisation was carried out at a scan speed of 0.1 mV/s from -500 mV to +3000 mV vs. E_{ocp}. According to the Tafel extrapolation method, corrosion potential E_{corr} and current I_{corr} were determined at the intersection of cathodic and anodic current curves extrapolated from the Tafel region, and the corrosion rate was calculated based on Faraday's law:

$$R_M = \frac{M}{nF\rho} I_{corr} \quad (3.1)$$

Where R_M is corrosion rate, M is the atomic weight of the sample, n is charge number that indicates electrons exchanged within dissolution reaction, F is Faraday constant (96.485 C/mol), ρ is bulk density and I_{corr} is corrosion current.

3.8 Structural characterisation

3.8.1 Optical microscopy

Investigations of the worn surface of the alumina ball after tribocorrosion test and of the alloy surface after laser treatment were carried out in Nikon Eclipse LV 150 (Nikon, Japan) with differential interference contrast (DIC).

3.8.2 3D optical microscopy

Morphology of wear track and SLM surface were evaluated through a 3D optical microscopy (Contour GT, Veeco Instruments). To minimize the number of no-measurement points (main error in non-contact technique), as received data was modified through a post-process software: Mountains Map (Digital Surf, France). The surface was firstly releveled, and non-measurement points were filled based on infinitesimal calculus. After that, the wear volume was estimated, and the corresponding specific wear rate could be calculated. Similar to the above measurements, each composition was tested at least three times to ensure data repeatability.

3.8.3 Scanning electron microscopy (SEM)

Samples after heat treatment, tensile deformation and tribocorrosion tests were investigated in an SEM (Inspect F50, FEI company) with an operating voltage of 10 kV (secondary electron mode) and 20 kV (backscattered electron mode), respectively. It should be noted that as-annealed and deformed samples were prepared via the above mechanical polish procedures. On the contrary, the morphology of the worn surface was directly examined after the experiment in order to avoid any influence of the external environment.

3.8.4 Electron backscatter diffraction (EBSD) and transmission Kikuchi diffraction (TKD) in SEM

The deformation mechanism was investigated through EBSD and TKD, which were conducted in a field emission gun SEM (Jeol 7900F, Japan). As shown in Fig.3.5, compared to the conventional EBSD technique, TKD has the same hardware except for the sample size. Bulk samples after mechanical polishing could directly be observed in the SEM (Fig3.5a) while the TKD sample should be as thin as below 100 nm. The thickness reduction could be realized via the focused ion beam (FIB) machining. In this work, compressed micropillars were thinned along the compression direction (normal direction) and then transferred to a copper grid. The thin foil sample was fixed in a specific sample holder, in which the EBSD detector could collect enough transmission signals during mapping. Step size ranged from 1 μm to 0.008 μm depending on the area of interest.

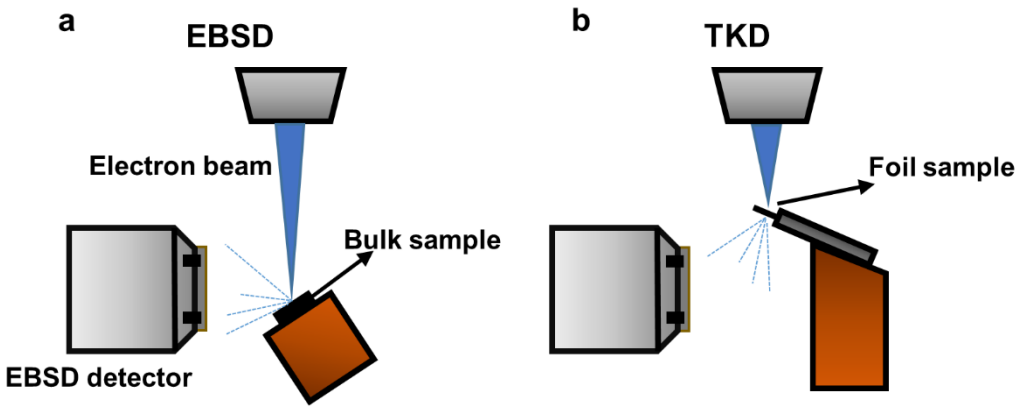

Fig.3. 5. *Schematic of EBSD and TKD process.*

3.8.5 Transmission electron microscopy (TEM)

3.8.5.1 Preparation of samples from the worn surface via focused ion beam (FIB)

To investigate the structural evolution of the worn surface. FIB samples were prepared using FEI Helios (SEM/FIB the Netherlands). Herein, we aimed to observe the subsurface. Thus, prior to etching, a rectangle Platinum (Pt)/Carbon (C) coating with a thickness of 2 μm was patterned to prevent the surface from ion damage. The area of the FIB sample was selected along the direction of reciprocation. Then the slice was transferred to the copper grid and it was milled as thin as below 100 nm using Gallium ions (Ga). Details of this process are illustrated in Fig.3.6.

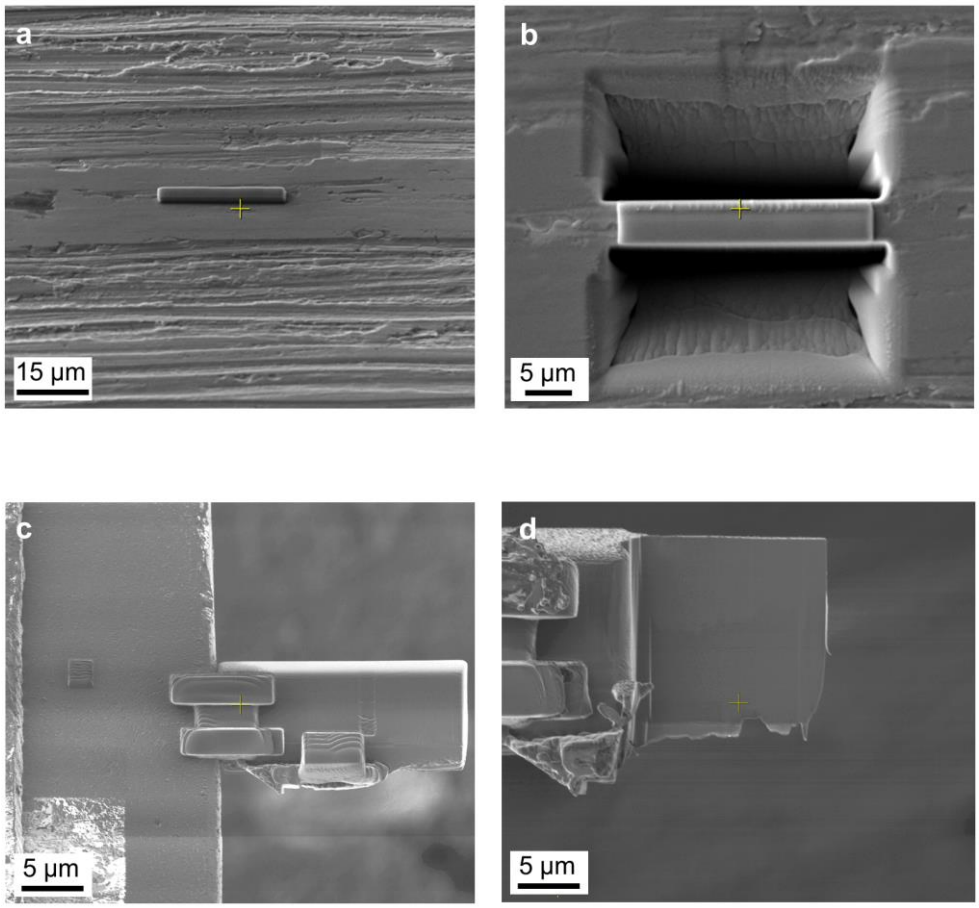

Fig.3. 6. *Schematic illustration of FIB process on worn surface.*

3.8.5.2 Preparation of samples via electropolishing

In terms of preparing TEM foil from the deformed sample, such as the tensile bar, electropolishing was chosen to avoid subsequent deformation, which may cause misunderstanding in observation. Prior to the electropolish, sliced samples were firstly ground to as thin as 120 μm and punched into a disc with a diameter of 3 mm using a disc puncher (Gatan, USA). After that, the foils were gently ground to a finale thickness of around 80 μm by 2400 grit grinding SiC papers, then ultrasonically cleaned three times in methanol. Twin-jet electropolishing was conducted on Tenupol-5 (Struers Ltd.) at -35 ℃ in an electrolyte consisting of 60 vol.% methanol, 5 vol.% perchloric acid and 35 vol.% 2-butoxyethanol. The

working voltage and flow rate were controlled at 20 ± 5 V and 12 ± 2 to ensure polish initialized from the central area. Lastly, the polished foils were cleaned by ion-milling (Gatan Model 600) for 1 min in order to remove contaminations completely. Beam energy and angle were set as 0.5 keV and 6°.

3.8.5.3 Warm-up analysis

Warm-up TEM investigations were performed on Tecnai T20 (FEI, Netherlands) and EM420 operated at 200 kV and 120 kV, respectively. The main purpose was to check the quality of foils quickly and confirm the area of interest, such as deformation twins and stress-induced martensite, in preparation for the subsequent analysis.

3.8.5.4 High-resolution transmission electron microscopy (HRTEM) and scanning transmission electron microscopy (STEM)

Most TEM investigation, including HRTEM and STEM, were performed in a cold-field emission transmission electron microscope JEM-F200 (JEOL, Japan) operating at 200 kV. This advanced microscope could provide spatial resolution as high as 0.19 nm, which promised direct observation of atomic structure.

3.8.5.5 Electron energy loss spectroscopy (EELS)

EELS mapping was carried out in JEM-F200 to investigate the elemental distribution of the tribofilm. Core loss edges: C-K, O-K and Ti-$L_{2,3}$, and corresponding zero-loss peak were recorded.

3.8.5.6 TEM Orientation Imaging

Unlike conventional EBSD techniques, the newly developed ASTAR detector (Nanomegas, France) can collect information of diffraction patterns from the TEM sample, automatically matching them with the target phase, which provides an orientation-phase map with excellent resolution as high as 1 nm (minimum step size). For mapping, the TEM spot size 7 was selected, with a 10 μm condenser aperture, a precession angle of 0.7 degrees and a step size of 2.5-10 nm, depending on the scan area. Diffraction patterns were recorded using the external camera, with an exposure time of 20 ms. Precession electron diffraction (PED) is a technique to collect quasi-kinematical diffraction patterns which are suitable for crystal structure determination using direct methods algorithms.

Chapter 4 Mechanical Properties and Deformation Behaviour of Ti-Mo-Fe-Sn Alloys

4.1 Introduction

Thanks to a combination of good excellent mechanical and biocompatible properties, Ti and its alloys are generally accepted as the best choice for implant bio-materials. However, due to the mismatch of stiffness between the metallic implant and human cortical bone (10-20 GPa), governed by stress shielding, the poor bone-remodelling process can result in loosening shortly after implantation [2]. Currently, Ti-6Al-4V ELI (Ti64 ELI) and Ti-12Mo-6Zr-2Fe (TMZF) are the two most popular Ti alloys for orthopaedic applications. However, their high Young's modulus (~110 GPa and 80 GPa, respectively), poor ductility (i.e., associated with limited working hardening), and potential risk derived from the release of toxic metal ions (such as Al and V in Ti64) limit their further applications [148]. Therefore, the development of new Ti alloys with low Young's modulus and enhanced ductility is required. The Young's modulus of Ti alloys mainly depends on their crystal structure. Athermal ω phase formed during quenching has the highest Young's modulus because the lattice misfit between ω and matrix leads to higher strain at the coherent interface. Hexagonal closed packed (hcp) α phase and hcp martensite (α') exhibit a higher Young's modulus than body-centered (bcc) phase and orthorhombic martensite (α'') [28]. Therefore, extensive work has focused on the development of metastable β Ti alloys through stabilising high-temperature β or β+α'' to ambient temperature, such as Ti-24Nb-4Zr-8Sn (Ti2448) and Ti-29Nb-13Ta-4.6Zr (TNTZ) presenting very low

Young's modulus [30]–[35]. However, on the basis of relatively weaker β stabilising effects, most developed compositions rely on significant additions of Nb and Ta, not only contributing to the accelerating price growth of raw materials, but also to increase the bulk density of implant.

Recently, enhanced plasticity in metastable beta Ti alloys has been realized via transformation induced plasticity (TRIP) and twinning induced plasticity (TWIP) effects[66], [152]. {332}<113> or/and {112}<111> twinning systems and stress-induced martensite (SIM) can be activated individually or simultaneously. With further deformation, the extent of twinning and/or SIM increases, which decreases the mean free path of dislocation movement, resulting in a dynamic strengthening effect. This dynamic strain hardening behaviour is well known as the dynamic "Hall-Petch" effect [66]. However, the enhanced ductility often comes at the expense of low yield strength (below 500 MPa) [152], which is ascribed to the low critical resolved shear stress (CRSS) for martensitic transformation and/or promotion of twinning. More recently, it was found that initial deformation by primary twinning combined with the formation of martensite at a higher strain can effectively tune the strength of β Ti alloy via adjusting the beta phase stability [68], leading to an excellent combination of yield strength and ductility.

Considering the biocompatibility requirements of metallic implants and the synergistic effects in multicomponent alloys, it is an arduous process to obtain the balance of strength, Young's modulus and ductility. In this chapter, the mechanical properties of novel three Ti-Mo-Fe-Sn (at.%) alloys designs were evaluated via the uniaxial tensile test. Effects of Sn on suppressing

athermal ω phase were determined by transmission electron microscopy (TEM) and high-resolution transmission electron microscopy (HRTEM). Electron backscatter diffraction (EBSD), Backscattered electron (BSE) imaging and TEM analysis were also performed to investigate the deformation mechanism.

4.2 Results

4.2.1 Phase and microstructure analysis

Table 4.1 lists measured compositions of Ti413, Ti513 and Ti514 in at.%. It was found that actual concentrations of alloying elements were close to nominal values. This validated the melting procedure detailed in the experimental section, which successfully prevented both elemental segregation and evaporation during melting. In addition, the oxygen content was measured, and the effects of it are discussed later.

Table 4. 1 *Measured composition of prepared Ti-Mo-Fe-Sn alloys in at.%.*

Alloy	Ti	Mo	Fe	Sn	O
Ti413	Bal.	4.1	1.0	3.0	0.2
Ti513	Bal.	4.6	1.0	3.3	0.4
Ti514	Bal.	4.9	1.0	3.9	0.4

The XRD spectra of as-annealed samples are plotted in Fig.4.1a, in which Ti64 ELI presents α + β diffraction peaks, and other three designed alloys exhibit similar diffraction peaks of β (110), β (200) and β (211). The corresponding microstructures were also observed via BSE

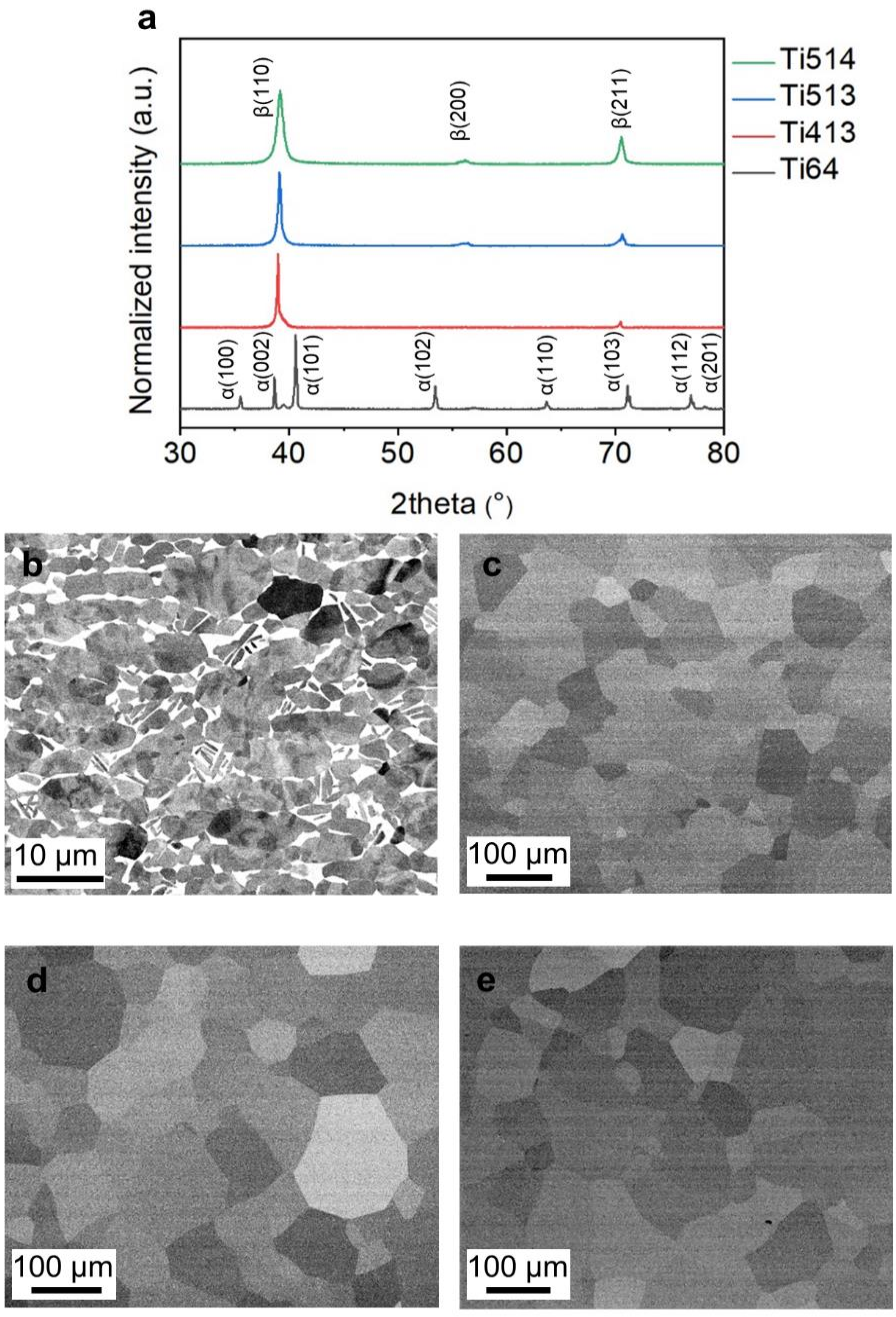

Fig.4. 1. *Microstructural analysis of benchmark and designed alloys. (a) XRD diffraction patterns. (b-c) The corresponding BSE images of Ti64 ELI, Ti413, Ti513 and Ti514 respectively.*

imaging. As shown in Fig.4.1b-e, Ti64 ELI exhibits an α + β equiaxed microstructure and transformed β phase (bright) homogenously dispersed between primary α grains (dark). Meanwhile, Ti413, Ti513 and Ti514 all display a fully β equiaxed grain structure with a mean grain size of 48, 59 and 61 μm respectively.

It should be noted that athermal ω phase was not found in either XRD or BSE results because the detection limit of phase amount in XRD was around 2%, which is insufficient to detect such a small amount of nanoprecipitation.

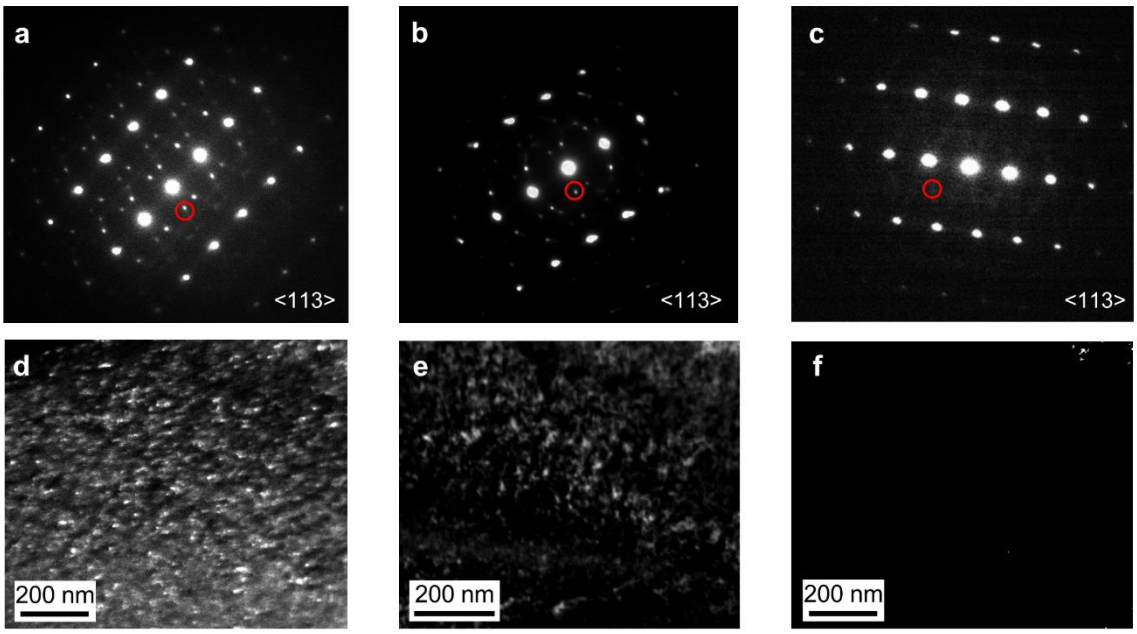

Fig.4. 2. *TEM analysis of omega phase in Ti514, Ti413 and Ti513. (a-c) Selected area diffraction patterns (SAED) of Ti514, Ti413 and Ti513 along <113> zone axis respectively. (d-f) Corresponding dark field images taken from red circles.*

In order to give more comprehensive evidence, the selected area electron diffraction (SAED) patterns of developed alloys were taken along [113] zone axis. In the SAED of Ti514 (Fig.4.2a), apparent ω reflections were found at the 1/3 and 2/3 location between (000) and {112} reflection of β planes, and corresponding dark-field (DF) image from red circle revealed that ω phase on the order of several nanometres was dispersed homogeneously in the beta matrix. In comparison, ω reflections in SAED patterns of Ti413 became weaker, resulting in a reduced number of nanoprecipitation in DF image (Fig.4.2e). Contrary to the existence of the athermal ω phase in Ti413 and Ti514, there was no indication of ω phase from secondary diffraction in the SAED and no nanoprecipitation was observed in the DF image of Ti513, which indicated that the formation of ω phase was expected to be completely suppressed.

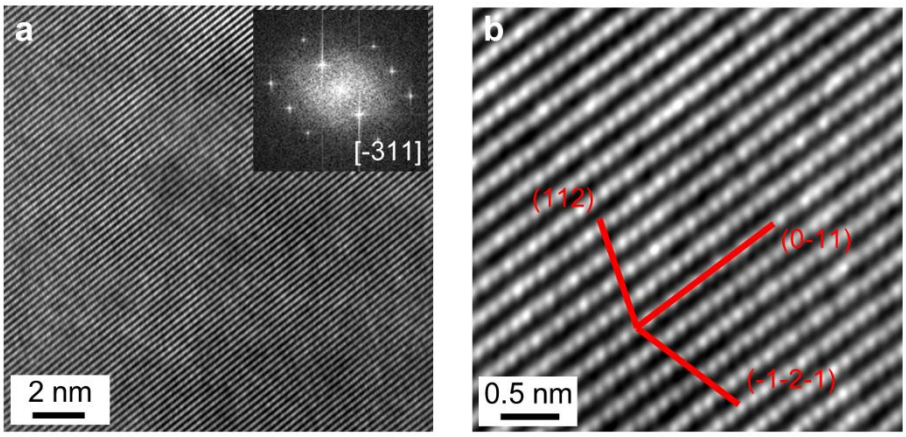

Fig.4. 3. *(a) HRTEM image from Ti513 and corresponding FFT pattern (inset of (a)). (b) Magnified IFFT image from (a).*

To further confirm this belief, an HRTEM image was obtained along the [-311] zone axis. Fast Fourier transformation (FFT) pattern (inset) as well as inverse FFT (IFFT) image in Figs.4.3a-b, confirms that Ti513 has the ideal bcc structure at the atomic scale, without any spinodal

decomposition and lattice modulation. It has been reported that the formation of athermal ω phase is associated with the commutative collapse of $\{222\}_\beta$ planes in quenched metastable beta Ti alloys, and the coherent interface between β and athermal ω phase fulfils the relationship of $<111>_\beta//<0001>_\omega$, $\{1\text{-}10\}_\beta//\{11\text{-}20\}_\omega$ [21], [43], [44], [153]. Generally, the athermal ω phase has a dispersive distribution in the matrix and plays a significant effect on the Young's modulus of the material. Therefore, as the ω phase has been fully suppressed in Ti513, the low Young's modulus is retained.

4.2.2 Mechanical performance of alloys

Figs.4.4a-b show the true stress-strain curves and corresponding strain hardening rate curves of Ti413, Ti513, Ti514 and Ti64 ELI respectively. It could be seen that Ti64 ELI exhibited a higher yield strength (YS, $\sigma_{0.2}$) around 850 MPa, however, plasticity was reduced because the strain hardening rate of the Ti64 ELI decreased monotonically upon yielding (Fig4.4b). This

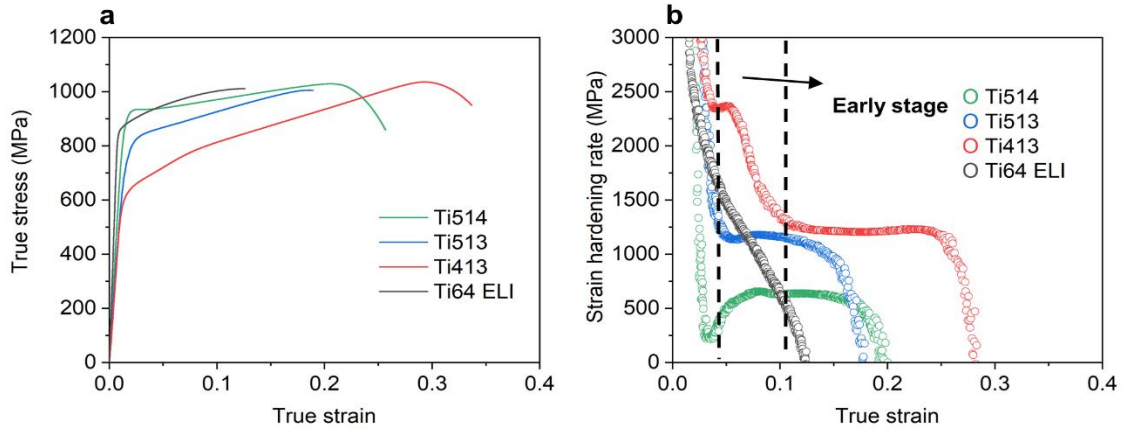

Fig.4. 4. *(a) True stress-strain tensile curves of designed alloys and Ti64 ELI. (b) Corresponding strain hardening rates.*

limitation is attributed to the simple deformation mechanisms involved in α+β Ti alloys. In α+β Ti alloys, the strain is accommodated by dislocation slip in the α phase, and the consistency of the glide direction in both prism and basal planes guarantees the activation of the cross-slip, thus leading to the low strain hardening rate and reduced plasticity [154], [155]. In comparison, my Ti413, Ti513 and Ti514 alloys all presented a good combination of strength and enhanced plasticity. Much stronger strain hardening behaviour was observed in Ti413 (Fig.4.4b). At the early stage of uniaxial tensile deformation, the decreasing strain hardening rate of Ti413 reached a maximum value of 2300 MPa at a true strain of 5%. Then, the rate continued decreasing and stabilised at 1200 MPa between 10% and 25 % strain. Beyond 25% strain, it decreased gradually and reached zero at 28%. Similarly, Ti513 and Ti514 also displayed a plateau around 1300 MPa (5~15%) and 600 MPa (5~18%) respectively, but the sudden increase of strain hardening rate at the early stage was not observed. According to the previous studies of metastable Ti alloys, the peak and plateau of strain hardening rate during deformation could be ascribed to the synergistic effects of SIM and deformation twinning [73], [74], [152].

The mechanical properties of the investigated alloys are summarised in Table 4.2. It was found that the calculated Young's modulus of Ti513 (52 GPa) was less than half the value of Ti64 ELI (110 GPa). The Young's modulus of Ti413 and Ti514 were 65 and 75 GPa, respectively, still lower than Ti64 ELI. Meanwhile, the YS, tEL (total elongation) and uEL (uniform elongation) of Ti413 were measured as 585 MPa, 40% and 31% respectively, which indicated significant strain hardening effects as well as enhanced plasticity. On the contrary, Ti514 had the highest YS (852 MPa) and still good ductility (tEL: 29%) but a negligible strain hardening

effect (uEL: 2.4%). It should be noted that Ti513 seemed to maintain a good balance between all the parameters in comparison to Ti413 and Ti514, where YS, tEL and uEL were measured as 740 MPa, 30% and 15%. To describe their potential for biomedical applications, a new index has been defined, namely, the elastic admissible strain, defined as the ratio of yield strength to Young's modulus, which was recently considered to be an important factor of materials for orthopaedic applications [148]. A higher value gives the induction of a good balance between yield strength and Young's modulus [148], [156]. The elastic admissible strain of Ti513 (1.42%) was the highest among all the alloys, indicating a significant promise as a metallic implant. To give a better understanding, the general trend in elastic admissible strain versus ductility for recent developed biomedical Ti alloys is summarised in Fig.4.5. Clearly, Ti513 stands out from the general trend, where a high elastic admissible strain is associated with a low total elongation and visa versa [9,21–34].

Table 4. 2 *Mechanical properties of Ti-Mo-Fe-Sn alloys and Ti64 ELI, including yield strength (YS, $\sigma_{0.2}$), ultimate tensile strength (UTS), Young's modulus (E), elastic admissible strain (EAS), total elongation (tEL) and uniform elongation (uEL).*

Alloy	YS (MPa)	UTS (MPa)	E (GPa)	tEL (%)	uEL (%)	EAS
Ti413	585 ± 13	778 ± 22	65 ± 8	40 ± 5	31 ± 6	0.92
Ti513	740 ± 8	844 ± 10	52 ± 5	30 ± 2	15 ± 3	1.42
Ti514	852 ± 22	917 ± 18	75 ± 5	29 ± 3	2.4 ± 0.2	1.14
Ti64 ELI	844 ± 6	910 ± 5	110 ± 3	20 ± 3	8 ± 2	0.77

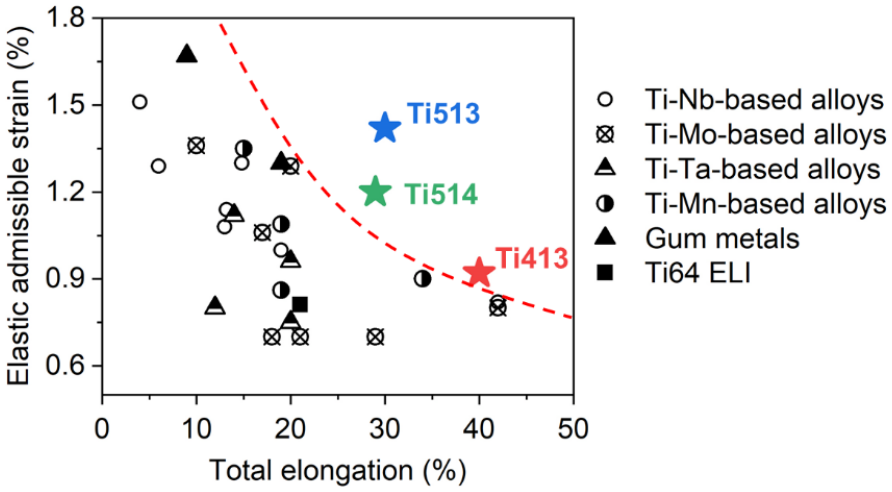

Fig.4. 5. *Comparison of elastic admissible strain and elongation in various established Ti alloys.*

4.2.3 Microstructural analysis of Ti413 strained to 5% and 15%

EBSD mapping was carried out at a strain of 5% and 15% to investigate the deformation mechanism of Ti413, which corresponded to the regions of peak and plateau observed on the curve of strain hardening rate (Fig.4.4b). As shown in Fig.4.6a, 5% strained Ti413 displays a heterogeneous distribution of band-like deformation products. Some grains are free of microscopic bands, while others show a parallel pattern. The phase map (Fig.4.6b) confirms that the nature of the bands is the martensite. In a selected inverse pole figure (IPF) map (Fig.4.6c) with higher magnification, together with phase and band contrast (BC) map, it has been found {332}<113> twins are also formed within martensitic deformation bands, in which the twinning boundaries are highlighted in red lines (Fig.4.6e). Besides, Fig.4.6f further gives a close-up view of another individual deformation product. It can be noted that there are two

martensite variants inside the band, resulting in a triple junction between martensite and {332}<113> twin. Corresponding {111} pole figure shown in Fig.4.6g reveals martensite variants fulfil the Burgers relationship showing {111} type I martensite twinning plane, indicated by the solid black circle.

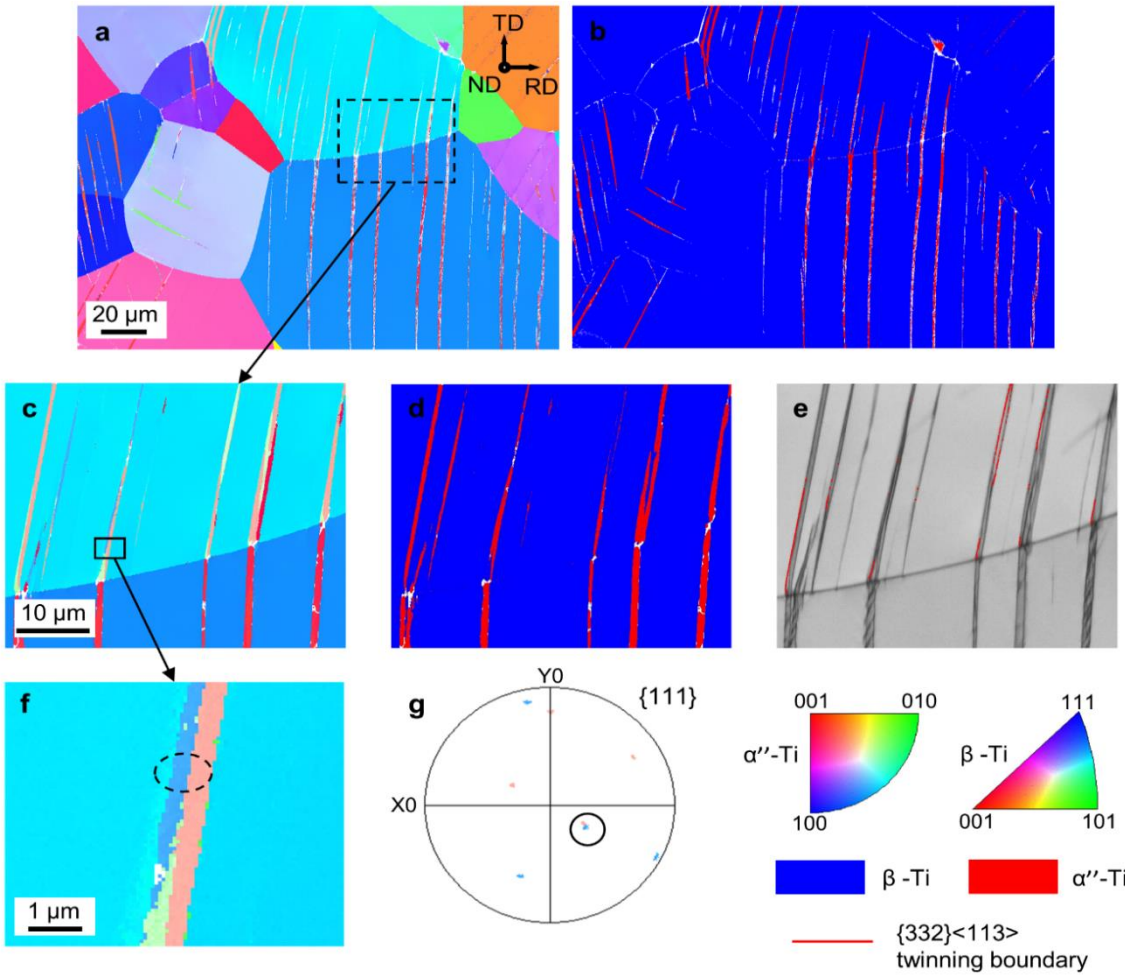

Fig.4. 6. *(a) EBSD IPF and phase map (b) of 5% strained Ti413. (c) (d) The enlarged IPF and phase maps from dashed black rectangle indicated in (a). (e) Corresponding BC map and {332}<113> twinning boundaries are highlighted (red lines). (f) The further enlarged IPF map from solid black rectangle indicated in (c). (g) {111} pole figure illustrating the Burges relationship between two martensite variants with dashed black circle in (f).*

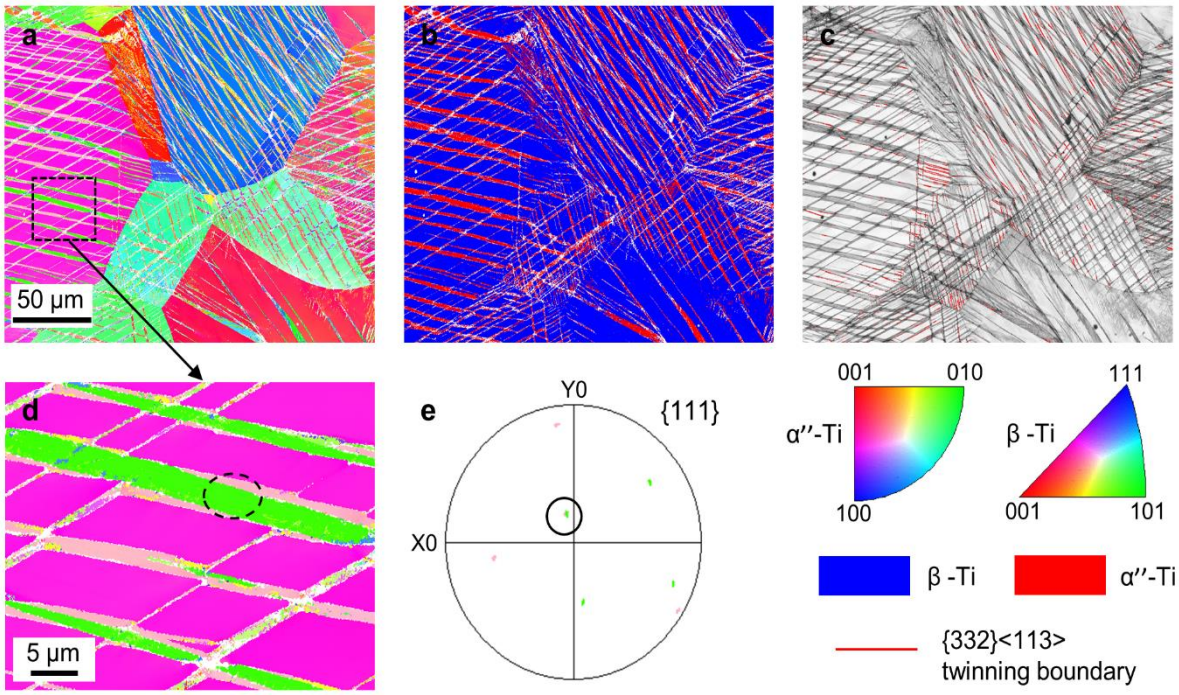

Fig.4. 7. *(a) (b) IPF and phase map of 15% strained Ti413. (c) Corresponding BC map and {332}<113> twinning boundaries are highlighted in red lines. (d) The enlarged IPF map from the dashed black rectangle indicated in (a). (e) {111} pole figure illustrating the Burges relationship between two martensite variants with a dashed black circle in (d).*

Figs.4.7a-e present the structural evolution of another sample deformed to 15%. Apparently, the IPF and phase map indicate the fraction of intragranular deformation products (martensite and {332} type twin) increases significantly. Subsequent martensite variants were extensively activated and started networking in grains, resulting from the higher critical resolved shear stress (CRSS) during deformation. Similarly, the {111} type I martensite twinning structure was identified again in an enlarged IPF map with {111} pole figure (Figs.4.7d-e). In addition, the width of these primary combined deformation bands also grew from sub-micron to several micro scales, which was believed to be a result of strain accommodation. Therefore, it could

be concluded that at both early and later deformation stages, Ti413 was dominated by martensite transformation, including {111} martensite twinning and {332} twinning inside of the primary martensitic band.

4.2.4 Microstructural analysis of Ti513 after straining to 10%

In order to investigate the deformation mechanism during the plateau region, a 10% strained Ti513 sample was chosen and well prepared for EBSD mapping. Fig.4.8a provides the IPF map of the deformed Ti513 microstructure at a strain of 10%. In comparison to previous results, there was no martensite detected in the deformed microstructure. The misorientation angles between matrix and deformation bands highlighted by the solid red lines were determined to be around 50.5°, corresponding to {332}<113>twinning systems.

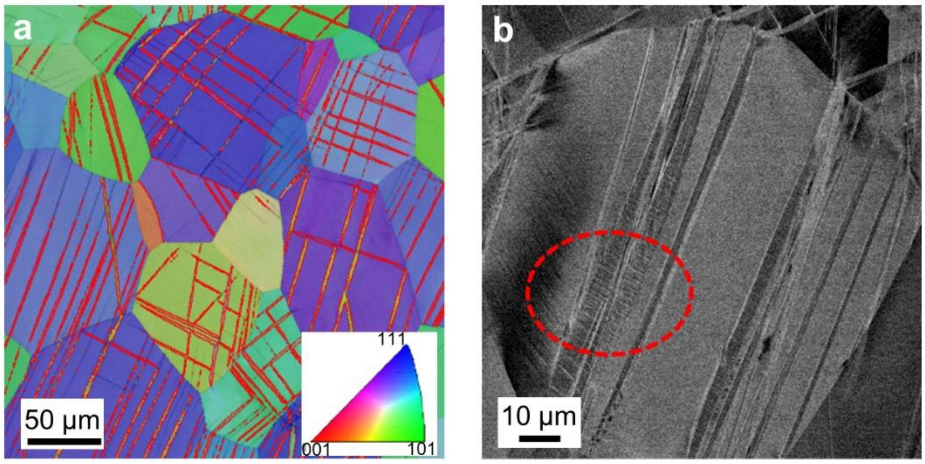

Fig.4. 8. *EBSD mapping of Ti513 deformed at a strain of 10% (a) IPF + IQ. (b) BSE image. {332} twin boundaries are marked by red solid lines in (a) and the band-like structures inside primary twin are marked by dashed red circle in (b).*

Generally, the networking of {332} type twins is denser at higher strains, leading to stable strain hardening and thus the large uniform elongation. Moreover, it can be found from the BSE image in Fig.4.8b that there is a high density of secondary deformation products inside of the coarse twins, which also contributes to the enhanced strain hardening rate and plasticity. As these fine secondary products are beyond the resolution of EBSD, TEM was employed to investigate these fine structures further.

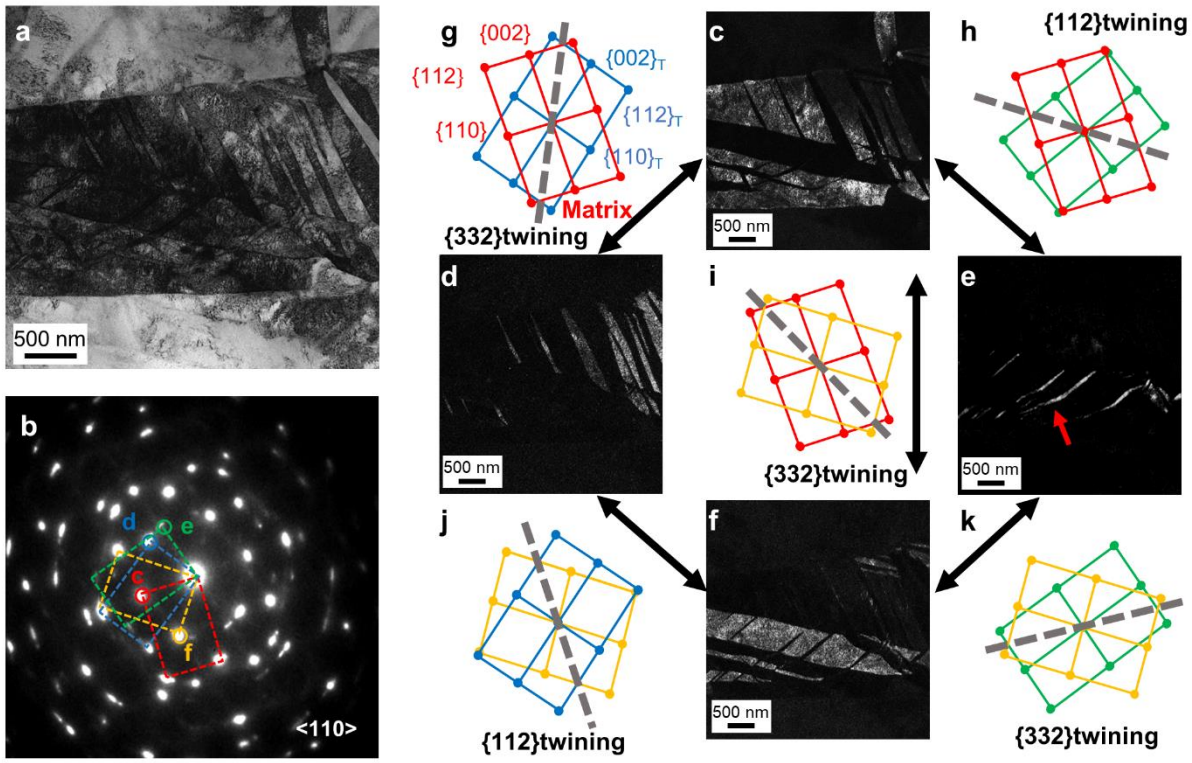

Fig.4. 9. *(a) Bright-field image of a primary deformation twin. (b) Corresponding SAED pattern inside the band along [110] zone axis. (c-f) Dark-field images taken from the solid circles indicated in (b). (g-k) The schematic illustration of relationships between deformation bands.*

Figs.4.9a-k give TEM micrographs of internal deformation bands in the 10% strained sample. Within the primary {332}<113> twin, the bright-field TEM image (Fig.4a) clearly reveals the existence of secondary deformation bands inside. The SAED pattern in Fig.4.9b indicates four sets of diffraction patterns along the <110> zone axis, and they are highlighted in red, blue, green and yellow solid rectangles, respectively. The corresponding DF images taken from the solid circles confirm the formation of three different deformation products (Figs.4.9c-f). According to the key diagrams in Figs.4.9g-i, these deformation products are defined as {112}<111> twin and two different variants of {332}<113> twins with respect to the primary deformation band. Interestingly, the schematic diagrams shown in Fig.4.9j and Fig.4.9k reveal that one of secondary {332}<113> twin shown in Fig.4.9f also fulfils the relationship of {112}<111> and {332}<113> twinning system with two other twins. Considering the geometric relationship between these band structures, the sequence of activation can be concluded as follows: primary {332}<113> twins were activated first during the early stage of the plastic deformation. An increase of strain resulted in the growth of primary {332}<113> twins and the activation secondary {332}<113> twins in coarse primary {332}<113> twins. With a further increase of stain, ternary {112}<111> twins were nucleated in secondary {332} type twins.

4.2.5 Microstructural analysis of Ti514 after straining to 10%

Fig.4.10a provides the IPF map of the deformed microstructure of Ti514 at a strain of 10%. It has been found that there were not any visible deformation products, which suggested neither twinning nor SIM formed during deformation. However, the BC map in Fig4.10b displays bands with distinct contrast, and they are widely distributed in most of the grains. The corresponding special grain boundary map in Fig.4.10c reveals that the localised misorientations of these bands are all less than about 15 degrees that have a similar characteristic to low angle grain boundaries. This finding was in agreement with previous work that the nature of the bands was expected to be slip bands attributed to massive dislocation events inside [158]. Therefore, further TEM analysis was carried out to give more detail.

TEM foil was firstly tilted to obtain [-111] zone axis under TEM mode (Fig.4.11a), and then switched to STEM mode. Fig.4.11b presents an overview of the observed band near the grain boundary (indicated by the white dashed line), whereas planar dislocations glide in (211) plane, corresponding to the {112}<111> slip system. Additionally, it should be noted the density of

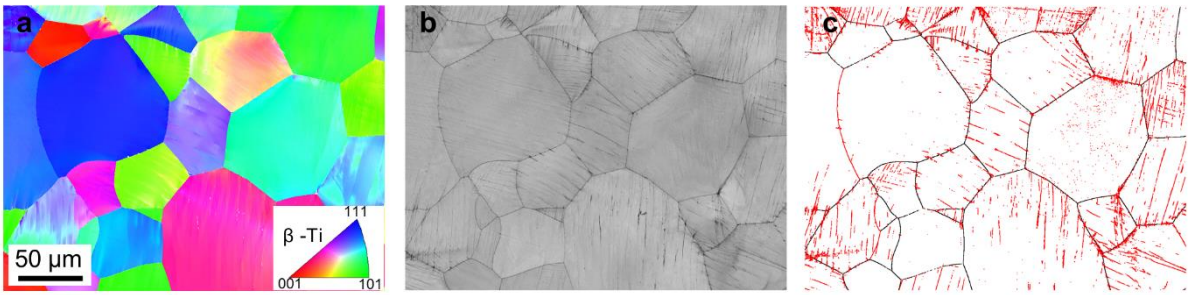

Fig.4. 10. *(a) (b) IPF and BC map of 10% strained Ti514. (c) Corresponding grain boundary map and low angle (<15 °) grain boundaries are highlighted in red lines.*

dislocations at the grain boundary was not concentrated, which indicated that current slip dislocation motion was suppressed. As seen from the enlarged view, dislocation loops with respect to {110} cross slip were found (marked by arrow). It was also observed that the multiplication of dislocations also contributed to the dynamic pile-up (marked by white dashed lines), which was in agreement with the previous reports that mobility of screw dislocation in Gum metal and some beta Ti alloys could be impeded [159], [160].

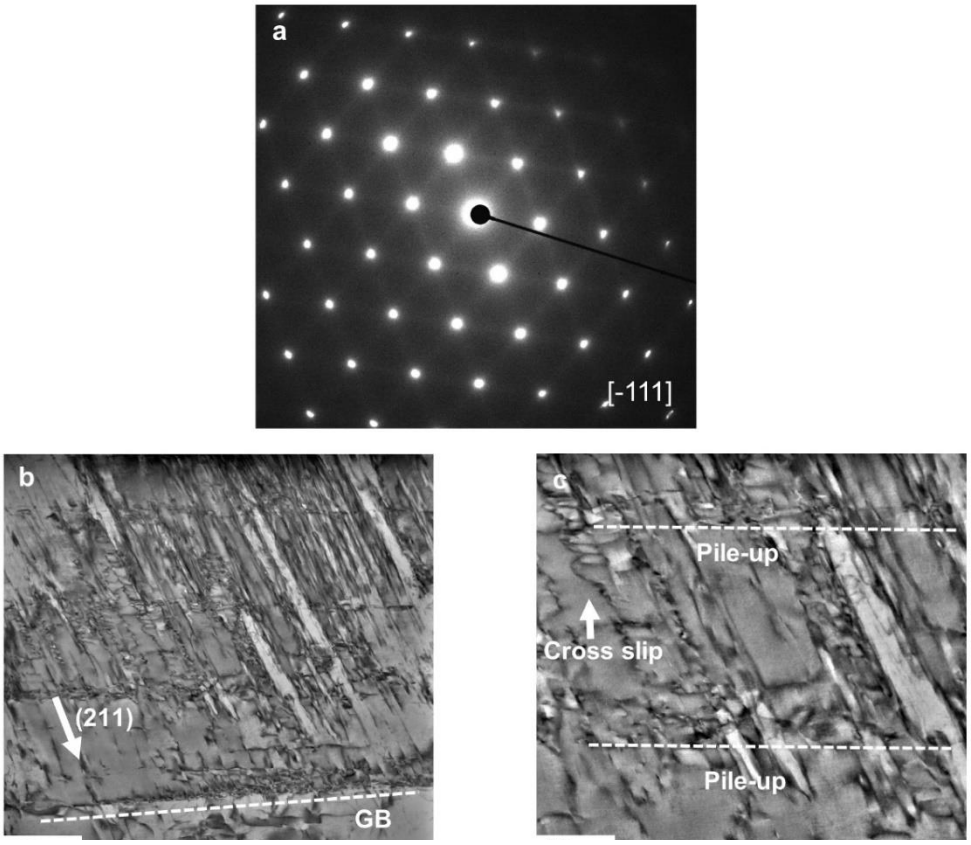

Fig.4. 11. *(a) SAED of 10% strained Ti514 taken along [-111] zone axis. (b) Corresponding STEM image indicating deformation band observed in BC image consisting of extensive dislocation events, grain boundary is highlighted in white dashed line. (c) Enlarged micrograph from (b), dislocation cross-slip and pile-up are indicated by white arrow and dashed lines respectively.*

4.3 Discussion

4.3.1 Effects of oxygen

It is worth noting that β Ti alloys could absorb all residual oxygen during high-temperature processing, including melting, hot rolling and annealing (even at high vacuum). According to previous work, the oxygen would affect the deformation mechanism in beta Ti alloys through the formation ω phase and martensite suppression, which was responsible for the improved yield strength and poor plasticity [18], [53], [161]. In my designed alloys, the maximum content of O (0.4 at.%) equalled around 0.12 mass%, which was usually recognized as a very low level of oxygen in many reported Ti alloys. Thus, its effects on mechanical performance could be considered negligible in this work.

4.3.2 The reduction of cost

It is known that the composition of the implant should consist of non-toxic elements. That is why many β stabilisers such as Nb, Ta, Mo are widely used in biomedical Ti alloy design. Table 4.3 illustrates the price of several metals used for producing Ti alloy, and it is found that all these rare metal elements are very expensive compared to Al and Fe. As mentioned above, recently developed Ti alloys for biomedical applications always contain a large amount of Nb and Ta due to their relatively low β stabilising potency. Thus, when designing a new composition based on these two elements, it still remains challenging to achieve a reasonable cost. By contrast, the stronger β stabilising effect of Mo is more favourable to industrialisation. Although another potential alloying element Mn is much cheaper than Mo, its biocompatibility

effects still need further investigation. Furthermore, the raw material cost of Ti413, Ti513 and Ti514 were compared to commercial biomedical Ti alloys, as shown in Table 4.4. It can be observed that the raw material cost of Ti-Mo-Fe-Sn alloys is lower than the majority of current options and very close to the lowest one, i.e., Ti-6Al-7Nb.

Table 4. 3 *The price of several commonly used metals used for biomedical Ti alloys [162].*

Material	Price (USD/kg)
Aluminium	1.9
Iron	0.12
Molybdenum	26
Vanadium	320
Tin	18.5
Niobium	42.3
Titanium	4.8
Tantalum	151.8
Zirconium	22

Table 4. 4 *Comparison of the cost of the new alloys and commercial biomedical Ti alloys.*

Alloy	Price (USD/kg)
Ti413	7.3
Ti513	7.6
Ti514	7.9
Ti64 ELI	17.2
Ti-6Al-7Nb	7.3
Ti-13Nb-13Zr	11.9
Ti-15Mo	8.0
Ti-12Mo-6Zr-2Fe	8.3
Ti-35Nb-7Zr-5Ta (TNZT)	26.5

4.3.3 On the origin of the low Young's modulus in Ti513

Previous work has suggested that Sn and Zr can effectively facilitate the prevention of omega-phase formation by suppressing the collapse of $\{222\}_{\beta}$ planes. Especially, the appropriate addition of Sn was also proved favourable to reduce phase instability, which could introduce lattice expansion via increasing lattice parameters, thus leading to elastic moduli softening [43]. Furthermore, the ultra-low Young's modulus can also be attributed to the electron/atom ratio (e/a, average valence electron per atom) of ~ 4.14. Decreasing e/a is favourable to get a low Young's modulus due to the correlated lattice softening effect of metastable beta titanium

alloys but negatively affected by the formation of α″/ α′ and ω related to the increased β phase instability [31], [163]. Thus, with a low e/a value, a minimum Young's modulus would be achieved when these metastable phases are completely suppressed. Lastly, the absence of athermal ω phase not only decreased Young's modulus to 52 GPa but also minimized the risk of embrittlement due to room ageing of β Ti alloys, which is significantly essential for long-term implantation [29], [148].

4.3.4 Contribution of Fe to the high yield strength in Ti513 and Ti514

The high yield strength of Ti513 and Ti514 were believed to be associated with the solid solution hardening effects of Fe. In a Ti-10Mo alloy, the addition of 2 wt.% of Fe increased the yield strength from 572 to 902 MPa by increasing the CRSS for twinning [164]. It is well known that the deformation mechanisms of metastable β Ti alloys change from SIM and twinning to slip as the β phase stability is increased. However, it does not mean more alloying elements addition is required because Fe is a eutectoid β phase stabiliser. During rapid solidification or heat treatment at high temperature, too much addition has the risk of forming "beta fleck", which is caused by segregation of β stabilisers and can facilitate the crack nucleation during deformation, deteriorating mechanical properties [165], [166]. The amount of Fe was chosen to be 1% to avoid the segregation and consequent poor plasticity in the current work. However, it was the synergy of the combined addition of Sn and Fe, which gave the excellent low Young's modulus, high yield strength, and enhanced plasticity. This strategy also has the potential to be introduced to other binary metastable Ti alloys, e.g., Ti-Nb and Ti-Ta.

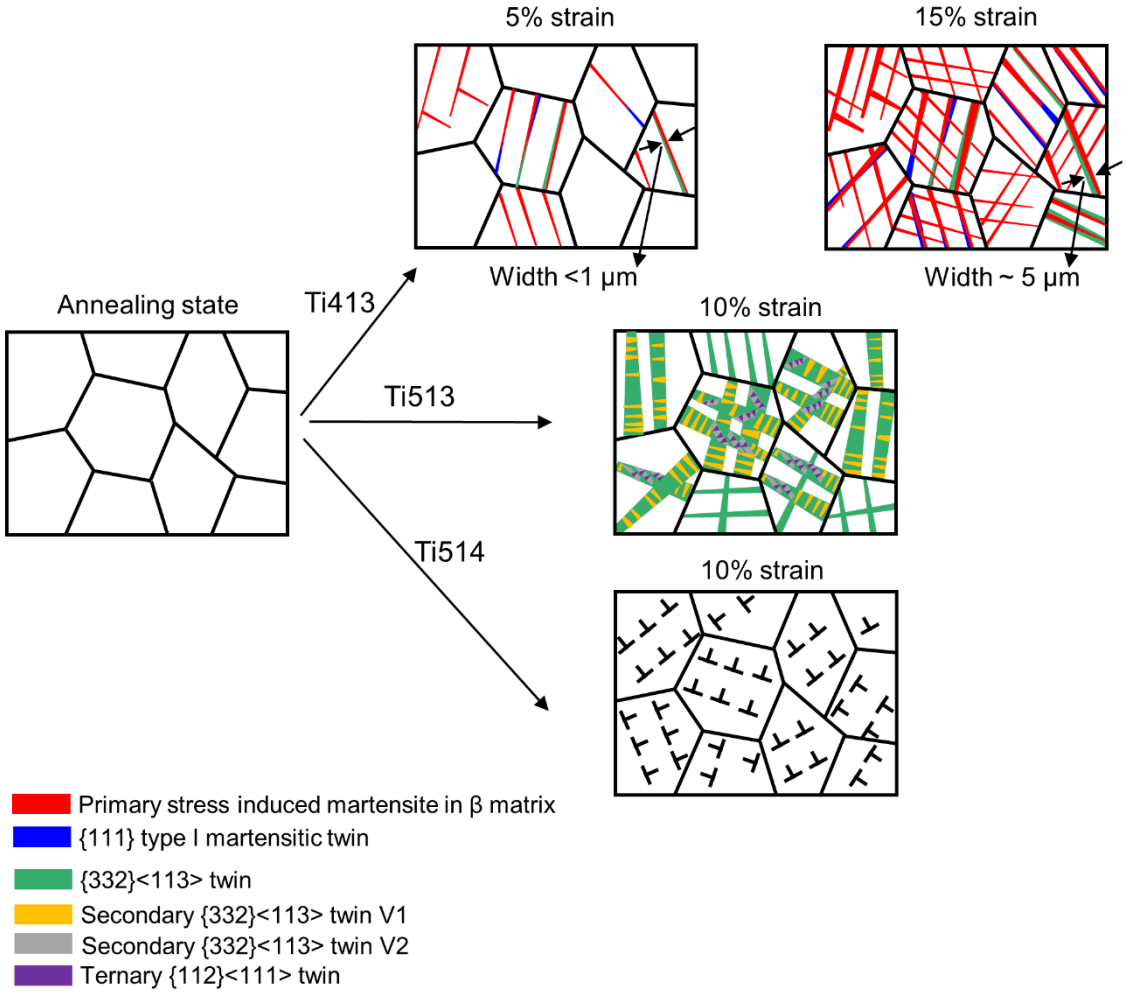

Fig.4. 12. *Schematic illustration of deformation mechanism of Ti413, Ti513 and Ti514 respectively.*

4.3.5 Effects of TWIP, TRIP and dislocation slip on mechanical behaviour in Ti413, Ti513 and Ti514.

Fig.4.12 displays a schematic diagram of the microstructural evolution of Ti413, Ti513 and Ti514 with different deformation stages. Their various deformed microstructure represented three main deformation mechanism in β Ti alloys: SIM, twinning and slip, consistent with the variation of β phase stability. In Ti413, TRIP and TWIP were both observed at early and later

deformation stages. These combined effects were shown to result in the strongest strain hardening behaviour in comparison to the other two alloys. The formation of primary martensite mainly contributed to the observed peak in the strain hardening curve. The continuous activation of secondary martensitic variants, as well as the growth of primary bands, were responsible for the stabilizing plateau during 10 ~ 25% strain (Fig.4.4b).

In Ti513, the deformation mechanism was dominated by multiple twinning, i.e., primary {332}<113> twin, secondary {332}<113> twin and ternary {112}<111> twin. The primary twins had relatively large sizes (width between 1 and 3 μm), which was like a subgrain in the recrystallized grains. The formation of secondary and tertiary twins efficiently subdivided the micro twins down to the nanoscale (Fig.4.9c). Thus, the continuous activation of subsequent deformation products could strengthen the primary twins and together contribute to a persistent dynamic Hall-Petch effect, which was responsible for the high and stable work hardening rates observed between 5% and 12% strain (Fig.4.4b). However, the formation of primary {332}<113> twins in metastable Ti alloys is quite complicated and is still not fully understood. As previously reported, the nucleation and propagation of twins are a function of grain orientation as well as other deformation products, such as SIM and {112}<111> twins [68], [74], [167]. The sub-twins appear to be a result of enhanced local stress condition and strain accommodation. Besides, the {112}<111> twin is known to have higher CRSS than that of {332}<113> twin [168]. Thus, the formation of ternary {112}<111> twin is attributed to the synergistic effect of enhanced local stress and higher Schmid factor (SF) due to local plastic deformation-induced grain reorientations. This explains why {112}<111> always nucleate

inside secondary twins [169]. Therefore, the *in-situ* evolution of SF inside the primary deformation bands should be investigated using precession diffraction in the TEM.

In comparison to TRIP and TWIP effects, simple dislocation in Ti alloys is usually not recognized as an effective way to realize enhanced plasticity. Dislocation can start to glide and concentrate upon yielding, resulting in the formation of microscopic slip bands. Recent studies found that the motion of screw dislocations in β Ti alloys was complicated, in which jogged dislocation could glide in a jerky fashion. The main reason for the low mobility was attributed to the extensive cross slip and pinning effects from the atomic cluster [159], [170]. Herein, similar multiplication of dislocations was also observed, and the contribution of dislocation slip to the ductility could be explained as follows. Dislocation cross-slip and glide were favourable to the formation of 3-D dislocation core configurations. Continuous "cross-glide" of dislocations requires more energy compared to conventional slip, which thus results in enhanced ductility [159], [171], [172]. However, it should also be noted that low mobility has a negligible effect on hardening because the multiplication of dislocations is not applicable to reducing the dislocation mean free path.

4.3.6 Discrepancy in $\overline{Bo} - \overline{Md}$ diagram

The *d*-electron theory is the most popular current approach to design Ti alloy composition. The $\overline{Bo} - \overline{Md}$ diagram derived from the cluster DV-Xα method [28], [32] clearly demonstrates the transition of deformation mechanism in metastable β Ti alloys, i.e., SIM, twinning and dislocation slip. Notably, as seen in the previous chapter, the calculated $\overline{Bo}$ and $\overline{Md}$ of Ti413,

Ti513 and Ti514 indicated their positions in Fig.3.1 were located in the martensite region, suggesting the deformation mechanisms should all be dominated by SIM. However, EBSD and TEM results showed that deformation mechanisms of Ti513 and Ti514 were dominated through twinning and dislocation glide respectively. There was no evidence of the formation of SIM. As previously suggested, it was found that the part of $\overline{Bo} - \overline{Md}$ diagram with low values, especially the martensite zone, still needs the investigation of more compositions to perfect the boundary positions [173]. It was also reported that Sn could decrease the martensite starting temperature (Ms) and acted as a β stabiliser in some cases [28], [43]. Thus, one explanation is believed that the addition of Sn in Ti-Mo based alloys prevents the SIM initiation when phase ability overcomes a critical level, which can be sketched through Mo_{eq} (>10). Another possibility is expected to be associated with the reversion of martensite that transfers to {332}<113> twin when the stress is released, which has been demonstrated by in situ synchrotron x-ray diffraction [174].

4.4 Summary

In summary, a new series of metastable β Ti alloys were successfully developed. They all exhibited very low Young's modulus and attractive plasticity, resulting in competitive elastic admissible strain compared to recent established biomedical Ti alloys. The main findings can be summarised as follows:

1. All designed alloys displayed a fully β equiaxed microstructure after the thermo-mechanical process route.

2. The enhanced plasticity of Ti513 was attributed to the network of primary {332} twins as well as the activation of various sub-twins, i.e., {332}<113> and {112}<111> twins. This was the first time to report the primary {332} twin consisted of two secondary {332} twins and {112} twins, which provided a new strain mediation strategy in metastable β Ti alloys.

3. Dislocation multiplication decreased the mobility of screw dislocations and improved plasticity. However, their effects on strain hardening behaviour could be negligible.

4. The combined addition of Sn and Fe was found to completely suppress the formation of the athermal ω phase and improve yield strength in Ti513, which promoted the highest elastic admissible strain (1.42%). Therefore, Ti513 was regarded as a competitive candidate for biomedical applications.

Chapter 5 Tribocorrosion Behaviour of Ti-Mo-Fe-Sn Alloys

5.1 Introduction

In recent years, β type Ti alloys with low Young's modulus have been widely studied with the emphasis on their corrosion and tribocorrosion performance [175]–[178]. However, the poor wear resistance of Ti alloys compared to ceramic and CoCrMo makes it difficult for them to be used as bearing surface materials [9]. Nevertheless, they are important components of the joint implant because of the superior corrosion resistance and specific strength.

Currently, the widespread adoption of modular design in hip prostheses provides flexible neck-stem combinations, which meets the growing demand for joint arthroplasty in various age levels [1], [179], [180]. However, the extra contact area, as well as the differences in mechanical properties, could lead to irreversible material degradation, thereby increasing the amount of wear particles, which raises more clinical issues after implantation [3], [5].

In this Chapter, the tribocorrosion behaviour of Ti413, Ti513 and Ti64 ELI were examined using a ball-on-disc reciprocating apparatus. The worn surface, the formation of tribofilm and the subsurface structure were also investigated in a specific sample. It is worth noting that the main factor that makes Ti514 unacceptable for further testing is attributed to the weak strain hardening ability (uEL~2.4%). Single-dislocation deformation mechanism without concomitant obstacles, such as twinning and stress-induced martensite, would easily initiate the surface cracking and lead to the accelerated material loss.

5.2 Results

5.2.1 Electrochemical behaviour

5.2.1.1 Open circuit potential (OCP)

Fig.5.1 shows the evolution of OCP versus time for Ti413, Ti513 and Ti64 ELI, respectively. Note that all alloys exhibited similar behaviour in which the potentials slightly changed in the positive direction upon immersion in the PBS solution containing proteins. As previously suggested [181], [182], this pathway involves the spontaneous formation of TiO or Ti_2O_3, anodic transformation to TiO_2 and corresponding oxide growth. Table 5.1 summarises the mean OCP values obtained for alloys after three tests. It is seen that Ti513 has the noblest OCP (-162 ± 17 mV) compared to Ti413 and Ti64 ELI, indicating a better protection characteristic of the passive film.

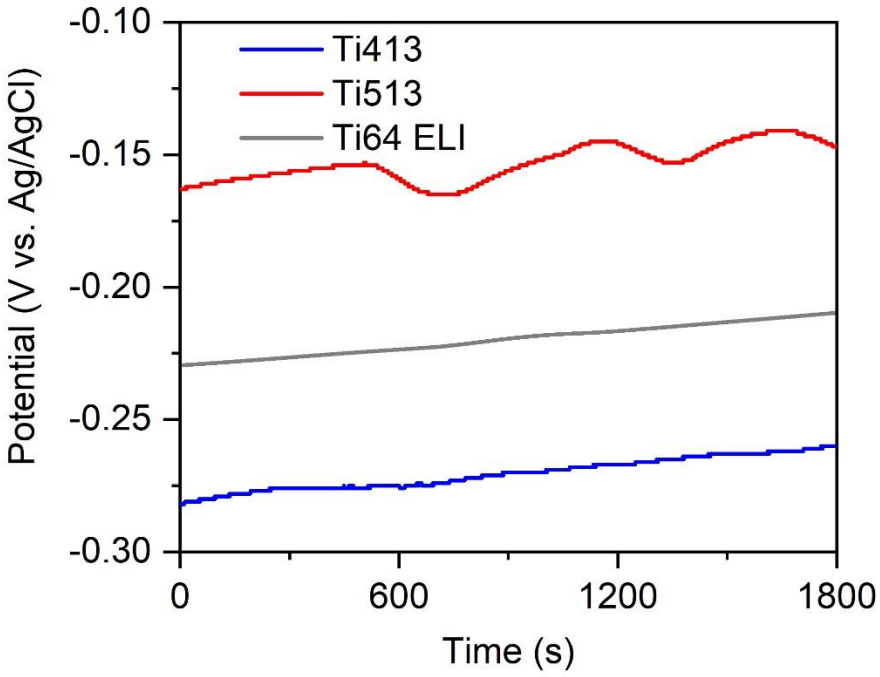

Fig.5. 1 *OCP curves for the Ti413, Ti513 and Ti64 ELI samples.*

Table 5. 1 *OCP values for the Ti413, Ti513 and Ti64 ELI samples.*

Sample	E_{ocp} (mV)
Ti413	-252 ± 41
Ti513	-162 ± 17
TI64 ELI	-230 ± 32

5.2.1.2 Potentiodynamic polarisation

Fig.5.2 shows the potentiodynamic polarisation for Ti413, Ti513 and Ti64 ELI. All samples displayed a similar active-passive transition and self-passivation behaviour. There was no observed breakdown potential or pitting until the upper limit of scanning potential, suggesting the formation of a stable and compact passive film in solution at 37 ℃. Ti413 presented a wider passive region (0.28 ~ 1.5 V) compared to Ti513 (0.56 ~ 1.5 V) and Ti413 (0.59 ~ 1.5 V). However, Ti513 and Ti64 ELI possessed a more positive E_{corr} (-0.50 V for Ti513 and -0.66 V for Ti64 ELI) and notably lower I_{corr} (0.052 μA/cm^2 for Ti513 and 0.033 μA/cm^2 for Ti64 ELI). The mean values of their corrosion parameters with standard deviation are shown in Table 7.2. E_{corr} of Ti413, Ti513 and Ti64ELI are -0.957 ± 0.036 V, -0.493 ± 0.023 V and -0.632 ± 0.045 respectively. It was also found that Ti513 had the lowest I_p implying faster repassivation kinetics without mechanical disruption. Thus, given these observations, it can be concluded that the Ti513 sample presented a better corrosion resistance.

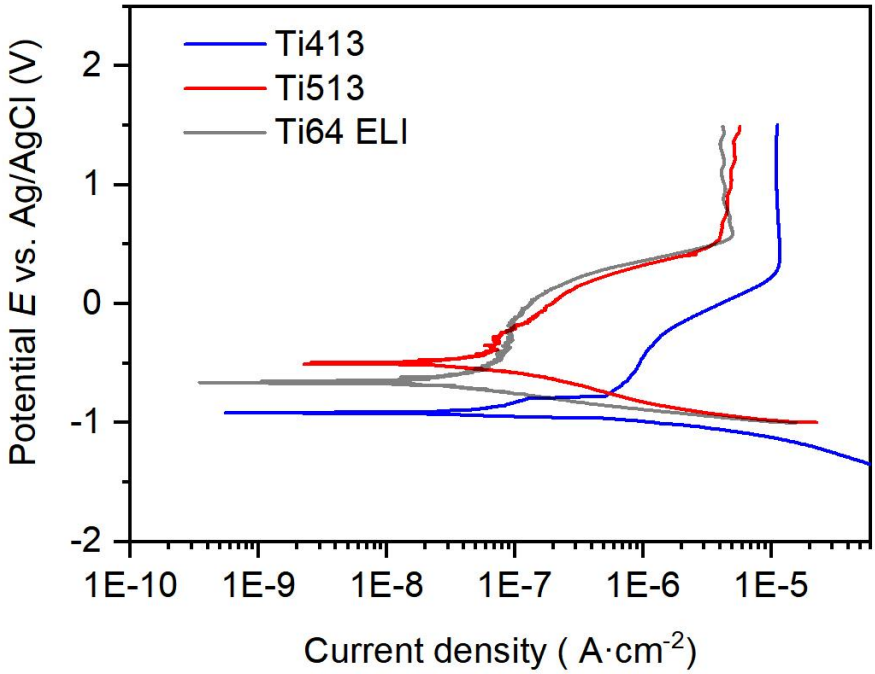

Fig.5. 2. *Potentiodynamic polarisation curves for the Ti413, Ti513 and Ti64 ELI samples.*

Table 5. 2 *Corrosion parameters of the Ti413, Ti513 and Ti64 ELI samples in potentiodynamic polarisation.*

Sample	E_{corr}	I_{corr} (μA/cm^2)	I_p (μA/cm^2)
Ti413	-0.957 ± 0.036	0.105 ± 0.010	12.285 ± 0.552
Ti513	-0.493 ± 0.023	0.057 ± 0.006	3.223 ± 0.114
Ti64 ELI	-0.632 ± 0.045	0.035 ± 0.008	3.485 ± 0.089

5.2.2 Tribocorrosion behaviour

5.2.2.1 -Tribocorrosion under OCP condition

Tribocorrosion behaviour of Ti413, Ti513 and Ti64 ELI were examined under the OCP condition at reciprocating-sliding frequencies of 5 Hz and 2.5 Hz, which corresponded to sliding velocities of 10 mm/s and 5 mm/s respectively.

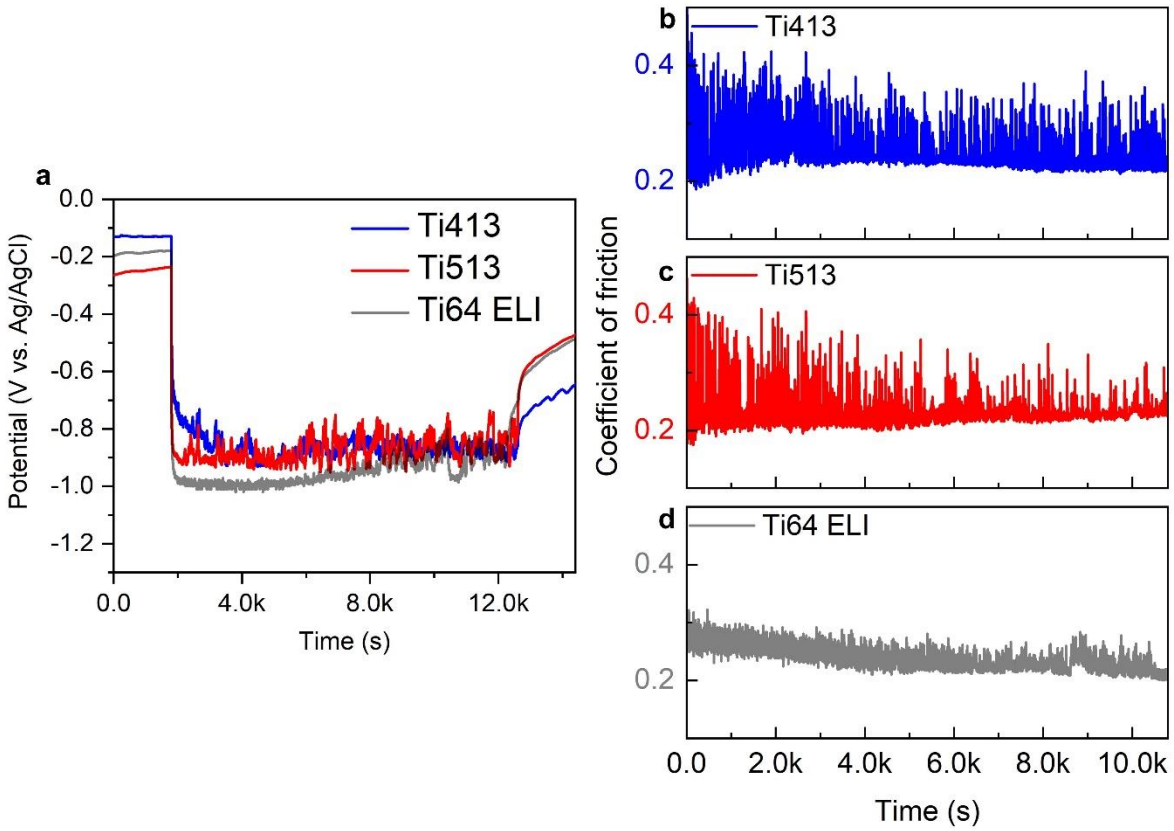

Fig.5. 3. *The evolution of the OCP (a) and the COF (b-d) during the tribocorrosion test at 5 Hz.*

Fig.5.3 shows the time dependence of the OCP and COF variation during reciprocating motion at 5 Hz. At the start of the mechanical disruption, the potential instantaneously moved to negative values in all alloys, corresponding to the breakdown of the passive film, i.e., depassivation (Fig.5.3a). Then, spontaneous repassivation was observed, as expected for passive metallic materials such as Ti alloys. The potential was observed to oscillate, i.e., the

actual surface degradation could be described as a dynamic depassivation and repassivation [79], [129], [183]. The potential oscillation for Ti513 and Ti413 was larger than Ti64 ELI. Similarly, the oscillation in the COF curves for the Ti513 and Ti413, Fig.5.3b and c was larger than in the Ti64 ELI curve, Fig.5.3d, which appeared to mirror the changes in the potential. The average COF for the Ti513 and Ti413 remained approximately constant throughout the test (~0.2), while there was a slight decrease from 0.3 to 0.2 for Ti64 ELI.

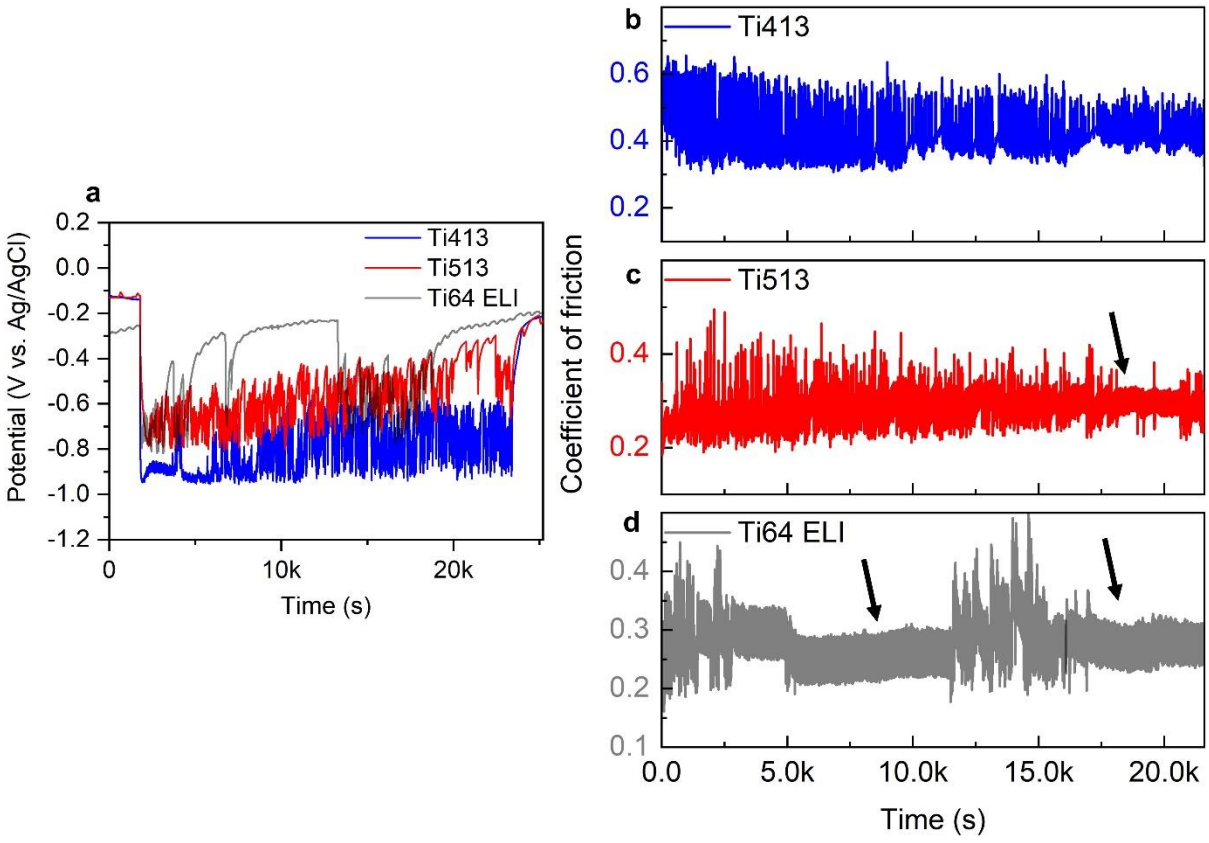

Fig.5. 4. *The evolution of the OCP (a) and the COF (b-d) during the tribocorrosion test at 2.5 Hz.*

Furthermore, OCP and COF results at 2.5 Hz are shown in Fig.5.4. As with the 5 Hz test, the potential dropped at the initial point of testing, after which there was a competition between

depassivation and repassivation. The oscillations in the potential were greater at 2.5 Hz than at 5 Hz. This is not surprising because a slower reciprocating speed gives more time for repassivation. For the Ti64 ELI, the repassivation was much stronger at 2.5 Hz than 5 Hz and much greater than for the Ti513 and Ti413. Moreover, the repassivation events lasted much longer for this alloy, Fig.5.4a. The corresponding COF curves (Fig.5.4b), the resulting COF (indicated by arrows) respond accordingly, being smoother with reduced signal noise, supporting the assumption that the formation of debris and ploughing effects from hard asperities are suppressed. As with the 5 Hz test, the COFs of Ti413, Ti513 and Ti64 ELI tested at 2.5 Hz exhibited oscillations that tended to mirror the potential behaviour, Fig.5.4b-d. The average COF values are summarized in Table 5.3, which shows that speed did not significantly alter the average COF. The lowest average COF was 0.23 ± 0.03 for Ti513 tested at 5 Hz, and the highest value was 0.34 ± 0.11 for Ti413 tested at 2.5 Hz.

Table 5. 3 *Average COF values for the Ti413, Ti513 and Ti64 ELI samples.*

Sample	5 Hz	2.5 Hz
Ti413	0.29 ± 0.06	0.34 ± 0.11
Ti513	0.23 ± 0.03	0.25 ± 0.01
TI64 ELI	0.28 ± 0.07	0.26 ± 0.03

The specific wear rates are presented in Fig.5.5. Ti513 exhibited the lowest wear rate (K = 1.80 × 10^{-4} ± 0.28 mm^3 N^{-1} m^{-1}) when tested at 5 Hz. Decreasing the sliding speed to 2.5 Hz led to a lower total material loss for all samples. A significant reduction in wear rate was observed

for Ti513 ($0.77 \times 10^{-4} \pm 0.03$ mm^3 N^{-1} m^{-1}) and Ti64 ELI ($0.31 \times 10^{-4} \pm 0.05$ mm^3 N^{-1} m^{-1}), and this was mainly attributed to the recovery of the passive state during tribocorrosion, which could play an important role in enhancing resistance to mechanical, as well as corrosive damage.

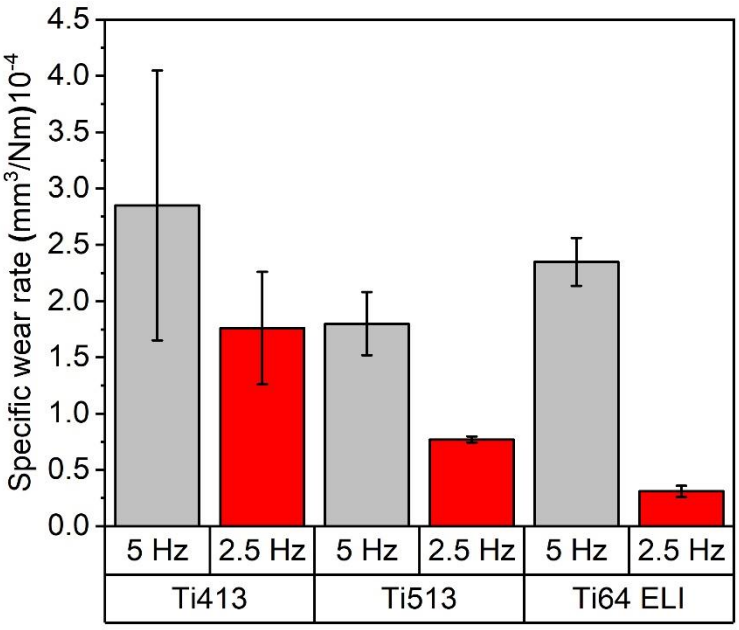

Fig.5. 5. *Comparison of specific wear rate between the Ti413, Ti513 and Ti64 ELI samples tested at 5 Hz and 2.5 Hz.*

5.2.2.2 Morphologies of the worn surface

In order to gain a better understanding of the wear mechanism, the morphologies of the worn surfaces were investigated using secondary electron imaging in the SEM. For Ti413 samples, there were visible grooves along the sliding direction under both test conditions (Fig.5.6). However, the worn surface tested at 2.5 Hz displayed more pronounced abrasive features than the 5 Hz test, including grooves and the flake-like debris near the edge of the grooves. It is clear that the formation of wear debris can act as third body particles and eventually accelerates

material loss in simulated body fluid (SBF) [184]. Additionally, a region exhibiting dark contrast was heterogeneously distributed on both worn surfaces, the extent of which was larger at the slower sliding speed. It is known that the organic matter has poor conductivity and so would appear dark in the SEM. Previous studies suggested that the dark region on the worn surface could be attributed to the formation of protein-enriched tribofilm [118], [185], [186]. Similarly, the oxide layer also exhibited dark contrast in SE images, which cannot be differentiated from the proteinaceous material [187], [188]. Therefore, it is necessary to investigate the tribofilm using FIB, which can provide direct cross-sectional observation at high magnification.

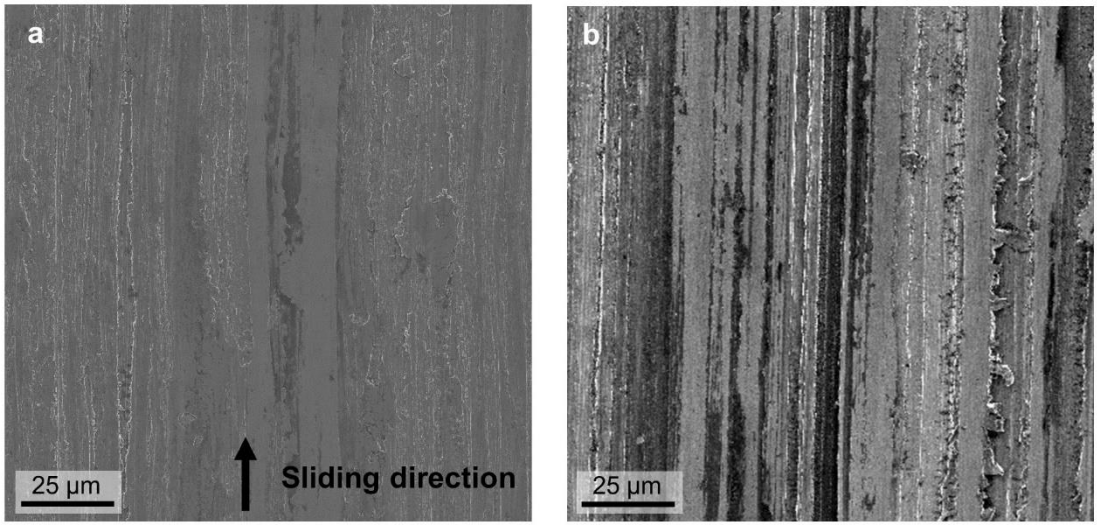

Fig.5. 6. *SE images of worn surface for Ti413 tested at (a) 5 Hz and (b) 2.5 Hz, respectively.*

The wear tracks of Ti513 and Ti64 ELI are shown in Fig.5.7 and Fig.5.8, with similar abrasion-dominated morphologies also observed. A closer examination of the Ti513 wear track at 2.5

Hz showed that the region with dark contrast was raised from the surface and generally had a much smoother surface.

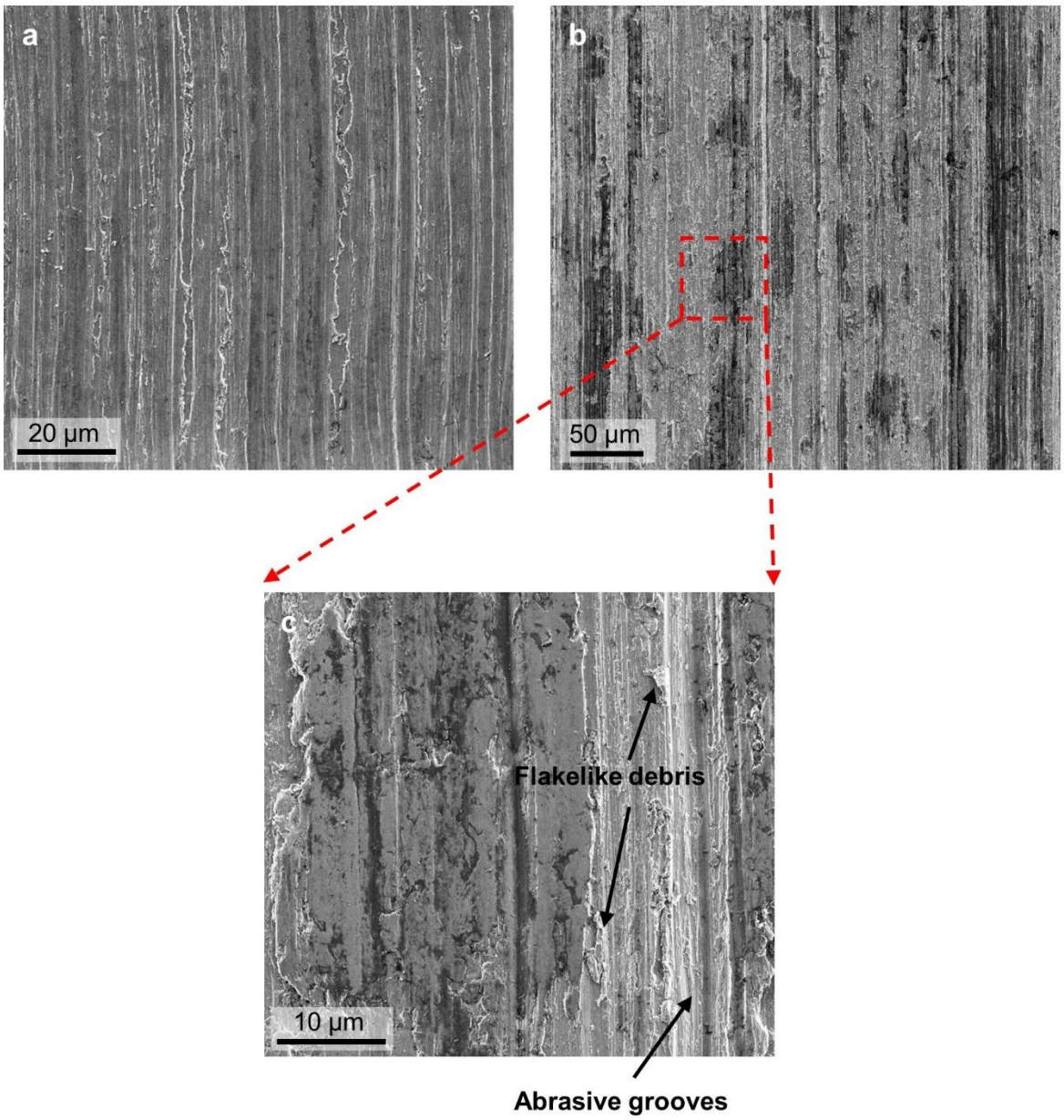

Fig.5. 7. *SE images of worn surface for Ti513 tested at 5 (a) Hz and (b) 2.5 Hz, respectively, (c) Enlarged SE image selected from the dashed box in (b).*

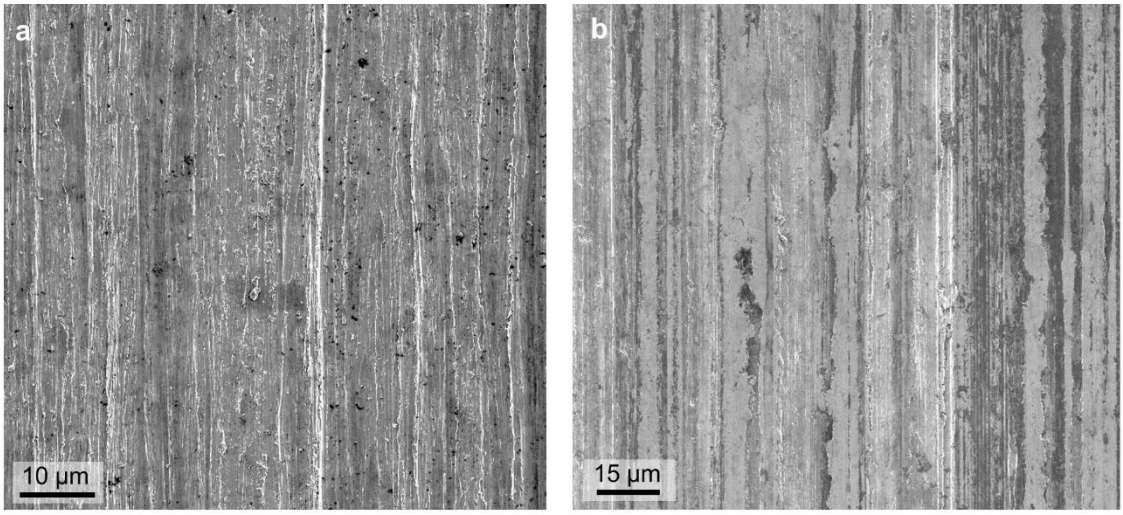

Fig.5. 8. *SE images of worn surface for Ti64 ELI tested at (a) 5 Hz and (b) 2.5 Hz, respectively.*

5.2.2.3 The formation of tribofilm

To further investigate the tribofilm and surface oxide structure, a FIB sample for TEM as prepared from the Ti513 tested at 2.5 Hz. As shown in Fig.5.9, a smooth region exhibiting darker contrast and raised up from the surface was located from the wear track centre. The surface was then covered by a protective carbon coating, and a lamella perpendicular to the worn surface along the sliding direction was milled by the ion beam. The polishing current was decreased step by step from 200 to 50 pA, which promoted the final thickness of ~50 nm and avoided the ion damage as much as possible.

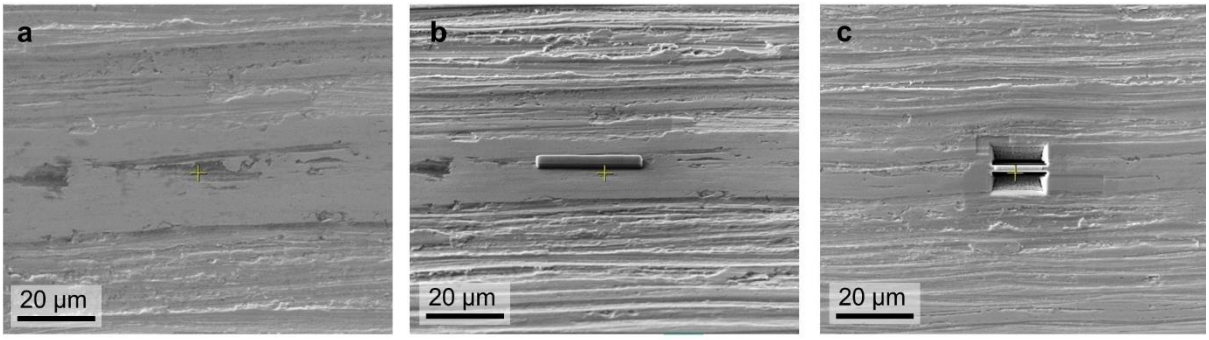

Fig.5. 9. *SE images illustrating the location of the FIB sample.*

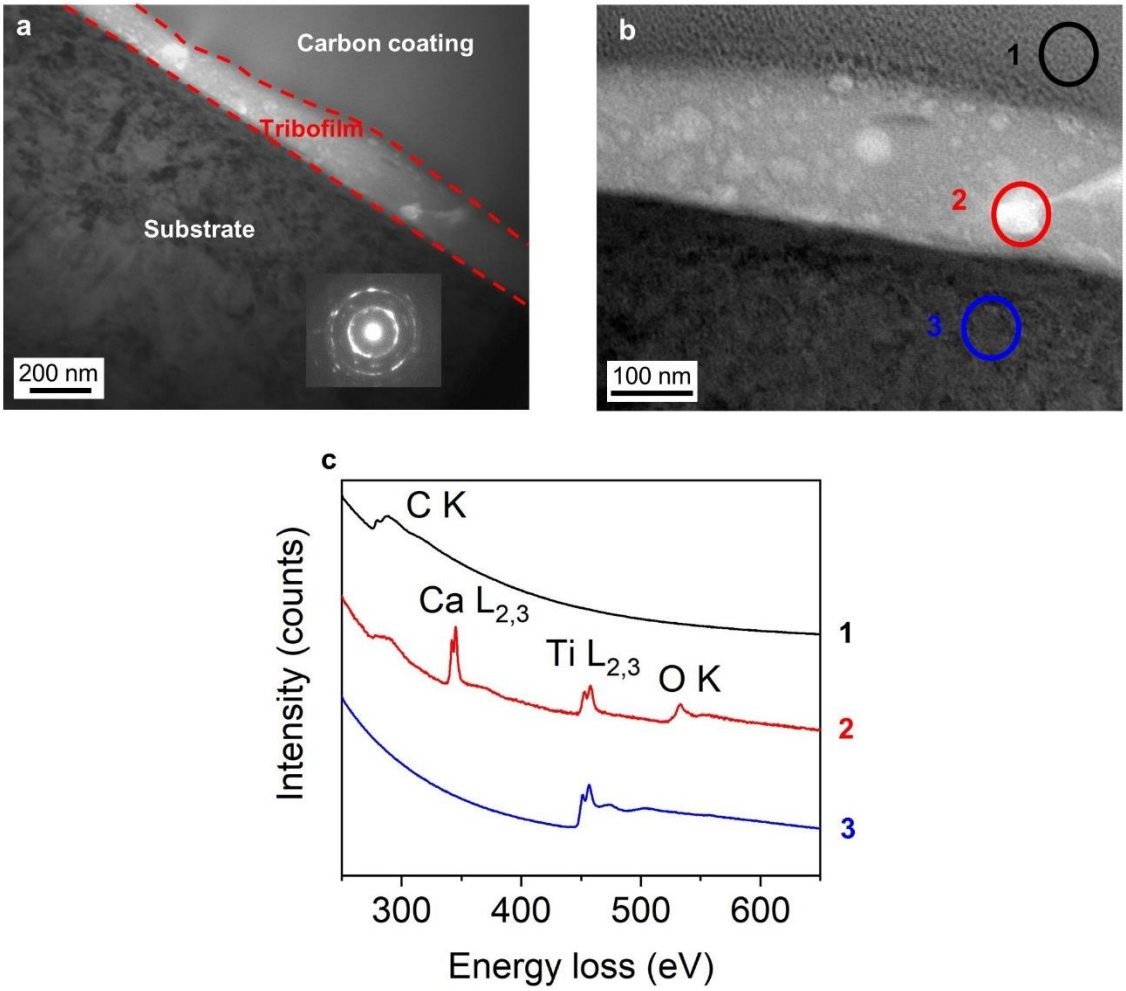

Fig.5. 10. *(a), (b) Bright-field TEM micrograph taken from longitudinal cross-section showing surface and subsurface microstructure of Ti513 tested at 2.5 Hz. (c) EELS spectra taken from marked regions in (b).*

Fig.5.10a and b show the bright-field TEM image of the cross-sectional surface. It can be seen that a tribofilm with a thickness of ~200 nm was formed on the topmost surface and a high density of nano-sized particles embedded inside. These smooth and oval particles were found to have a homogeneous distribution in the tribofilm with a diameter ranging from a few to tens of nanometres. Underneath the tribofilm, a nanocrystalline layer was present, with the corresponding selected area electron diffraction (SAED) pattern showing a wide range of

crystal orientations within the crystallites. Nanocrystalline layers form in response to the shear loading during reciprocating contact [90], [189].

In order to understand the material constituents comprising the tribofilm, EELS point analysis was performed from the deposition through to the substrate. Fig.5.10c displays the normalized EEL spectra obtained from three sites of interest marked in black, red and blue circles (Fig.5.10b). It should be noted that the red circle was selected to cover an embedded particle, but the collected information also contained the inelastic scattering electrons from the surrounding matrix. Only the C-K characteristic edge was present in the carbon coating, and there was no evidence of other metallic components or oxygen. For the target particle, the Ca-$L_{2,3}$, Ti-$L_{2,3}$ and O-K edges were seen with a weak C-K edge. The sample often drifted a small amount (few nm) during EELS measurements so that the Ca-$L_{2,3}$ and C-K represented the main constituents of the matrix of the tribofilm. The O-K edge was only found in this region and was not associated with titanium, and so did not arise from titanium oxides. Rather it must have come from the tribofilm. In the substrate, only Ti-$L_{2,3}$ edges were observed, and there was no trace of C-K edges, implying that the specimen contamination during FIB thinning was negligible.

As shown in Fig.5.11, a heterogenous tribofilm with a total thickness around 100 nm was formed on the worn surface of the Ti64 ELI tested at 2.5 Hz. The tribofilm comprised inner and outer layers. It was found that the outer part of the tribofilm (region 2) displayed weak contrast with a small number of nanoparticles within it. C-K, Ti-$L_{2,3}$ edges and a weak O-K edge were observed in EEL spectra taken from region 2. The stronger strength of the C-K edge

suggested that this layer became enriched in absorbed protein from the BCS solution. It is known that in high angle annular dark-field (HAADF) images, the contrast is approximately proportional to the square of atomic number, i.e., Z contrast [190]. Thus, the dark contrast of this region 2 was consistent with a proteinaceous layer. The inner part of the tribolayer (region 3) had a similar characteristic to that observed on the surface of the Ti513 (Fig.5.10b), also with nanoparticles inside. The corresponding EEL spectra exhibited a weak C-K and O-K edge, with a clear Ti-$L_{2,3}$ present, while the HAADF contrast was similar to the titanium substrate. The weak O-K edge was found in various places, including the substrate, indicating it arose from mild oxidation of the FIB sample and not the formation of titanium oxides. This suggests that this layer was primarily nanocrystalline titanium.

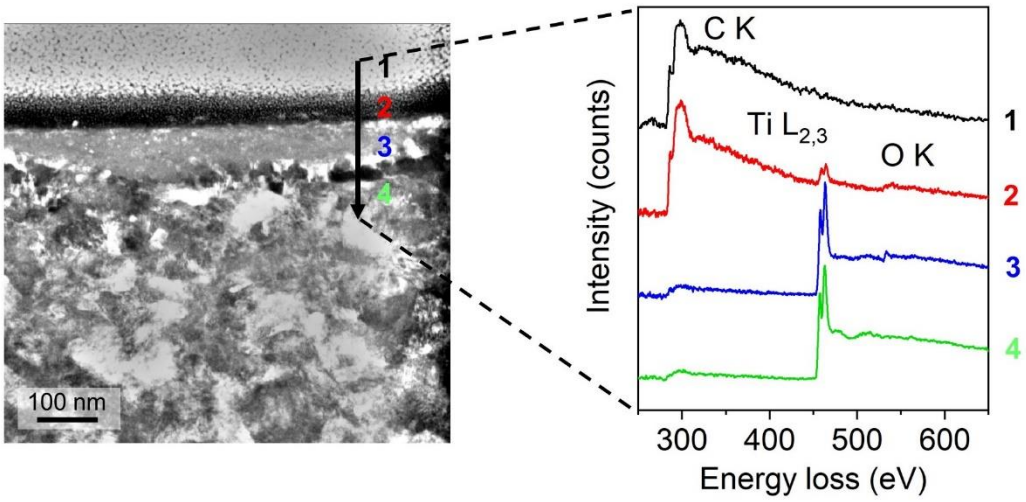

Fig.5. 11. *STEM-HAADF micrograph taken from longitudinal cross-section showing surface microstructure of Ti64 ELI tested at 2.5 Hz. Also shown are the corresponding EELS spectrums taken from deposition to substrate, marked 1 –4.*

5.2.2.4 Structural evolution of subsurface

The largest difference in wear rate was between the Ti64 ELI tested at 5 Hz and 2.5 Hz. To understand the difference in substrate evolution, FIB cross-sections were examined using ion channeling contrast and also in the TEM. As illustrated in Fig.5.12a, the region of interest in the wear track centre was first covered by a protective coating to prevent ion beam damage. A half-sided hole with a dimension of 20 µm × 20 µm × 20 µm was drilled, and the section parallel to the sliding direction was carefully polished until the microstructure appeared. It was found that both samples displayed a near-surface nanocrystalline layer, but the nanocrystalline layer was much thicker at 2.5 Hz compared to 5 Hz (the measured thickness for 5 Hz was 1-1.5 µm and for 2.5 Hz was ~2-3 µm).

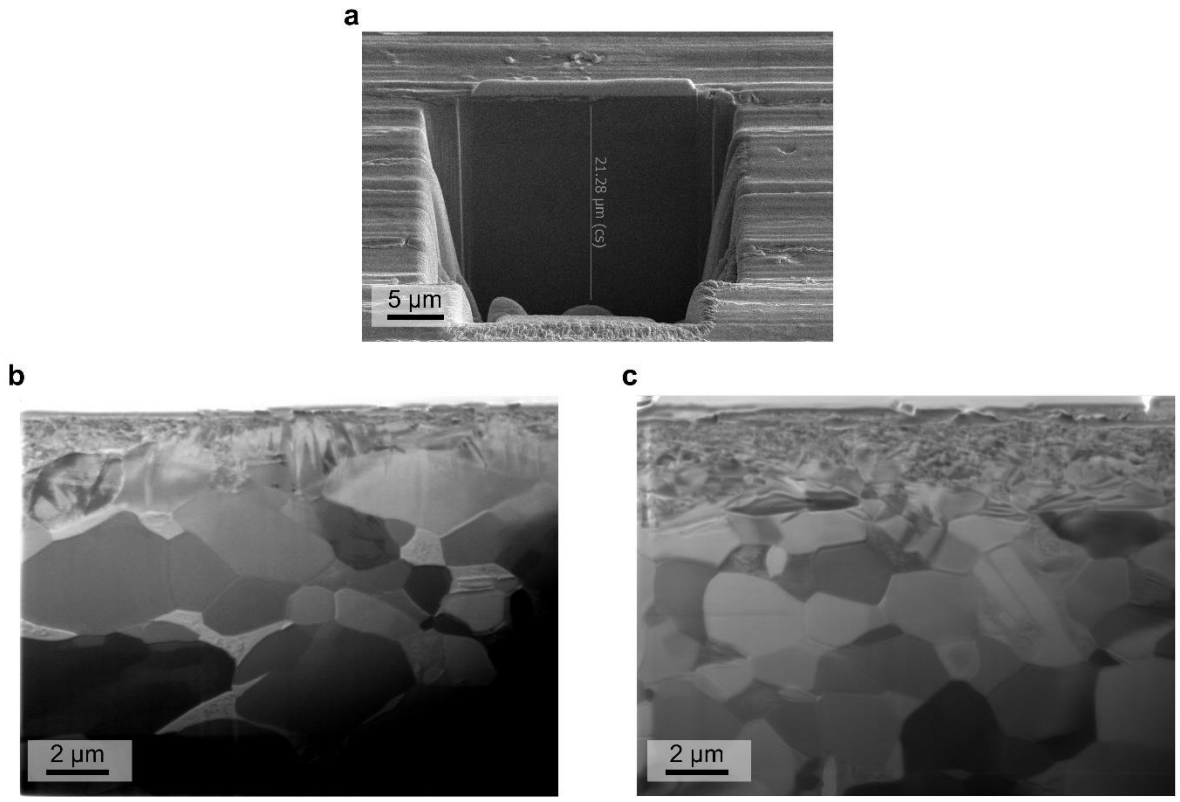

Fig.5. 12. *(a) SE image showing the cross-sectional FIB preparation along the sliding direction. (b), (c) Ion channelling contrast images of Ti64 ELI tested at 5 Hz and 2.5 Hz.*

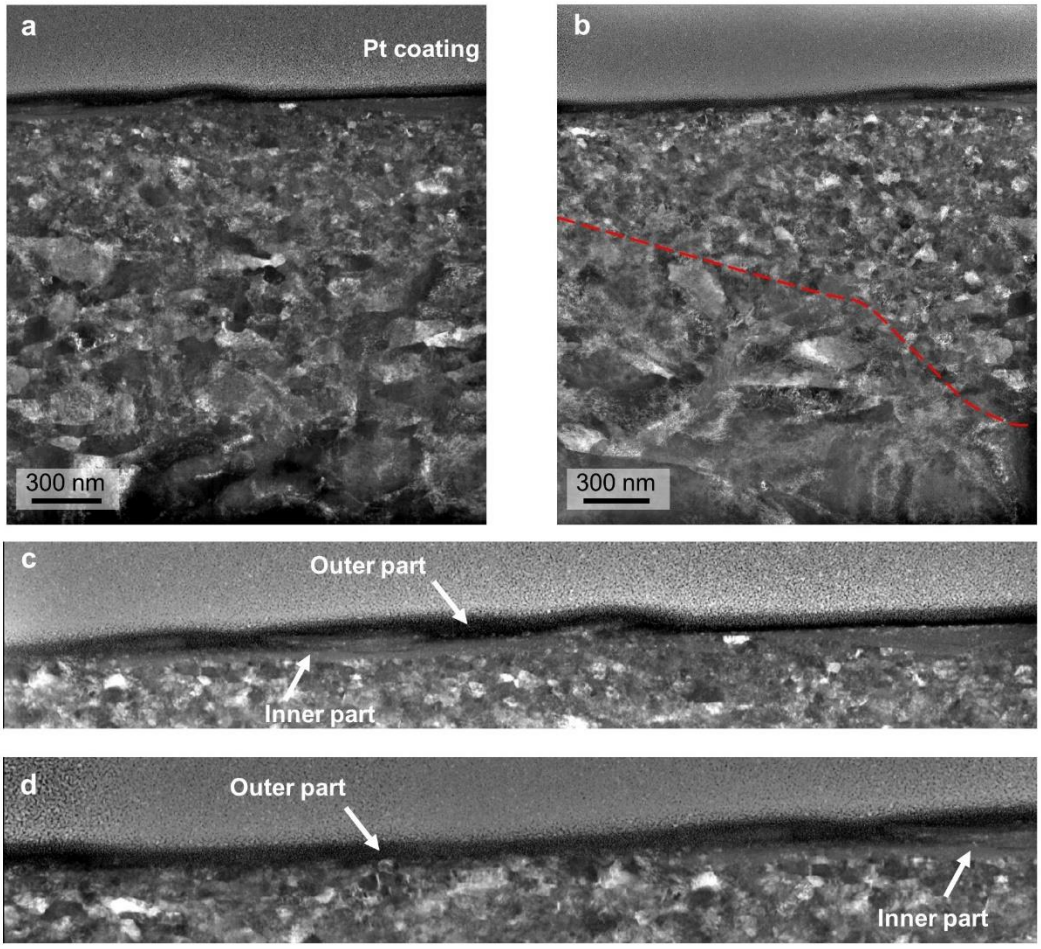

Fig.5. 13. *STEM-HAADF micrographs taken from a longitudinal cross-section of Ti64 ELI tested at 2.5 Hz showing the influence of inner-part tribofilm on subsurface microstructure. (c) and (d) a closer look at interface taken from (a) and (d), respectively.*

Fig.5.13 shows STEM images from a FIB TEM lift-out sample taken from the 2.5 Hz test to obtain a more detailed examination of the surface microstructure. An ultra-fine nanocrystalline structure is clearly visible underneath the tribofilm. In Fig.5.13a, the grain size in the nanocrystalline layer gradually increases with depth below the contact surface. Fig.5.13b shows a region with a thinner nanocrystalline layer when the tribofilm comprises just the outer part. In this region, a thinner nanocrystalline layer (average grain size <50 nm) was observed,

which had a more abrupt interface between the nanocrystalline and substrate layers. The same observations were made in other places, namely that a thicker tribofilm, having both inner and outer parts, coincided with a nanocrystalline thicker layer.

5.3 Discussion

5.3.1 The effect of speed on contacting interface conditions

The wear rate of Ti413, Ti513 and Ti64 ELI was about 39 %, 57 % and 85 %, respectively, lower at 2.5 Hz compared to 5 Hz. The lower wear rates at 2.5 Hz were also associated with a much smoother worn surface morphology. In addition, alloys tested at 2.5 Hz exhibited a more widespread tribofilm compared to the tests at 5 Hz. Thus, it can be concluded that the greater formation of tribofilm may be the key factor to the improved wear resistance. To explain the greater formation of a tribofilm at 2.5 Hz and its effect on material degradation, the difference in interfacial conditions between 2.5 Hz and 5 Hz must be understood.

Firstly, the effect of sliding speed on interface temperature must be considered. In non-conforming contact, such as ball-on-disc configuration, rubbing surfaces with very small contact area will experience a localised rapid increase in temperature when two asperities are in contact, i.e., the flash temperature. Under lubricated conditions, based on a steady-state heating model, the averaging temperature of the lubricant film T_L (℃) can be given as follows [191], [192]:

$$T_L = 0.1665 \frac{\mu W U}{\pi a^2} \frac{h}{2k_{lub}} + T_{surface} \qquad (5.1)$$

Where μ is the coefficient of friction, W is the normal load, *U* is the speed of heat source or sliding speed, *h* is the lubricant film thickness, k_{lub} is the thermal conductivity of the lubricant and *a* is the contact area.

Furthermore, surface temperature $T_{surface}$ can be expressed by:

$$T_{surface} = T_{lub} + \Delta T \tag{5.2}$$

Where T_{lub} represents the bulk temperature of the lubricant, here, that is 37 ℃. ΔT is surface temperature increase due to reciprocating contact, which can be further evaluated based on the dimensionless Peclet number (L)

$$\Delta T = \frac{\mu WU}{4ka} \quad , \qquad L = \frac{Ua}{2\chi} \qquad L < 0.1, \tag{5.3}$$

$$\Delta T = [0.35 + (5.0 - L)\frac{0.5}{4.9}]\frac{\mu WU}{4ka} \qquad 0.1 < L < 5.0, \tag{5.4}$$

$$\Delta T = \frac{0.308\mu WU}{4ka}\sqrt{\frac{\chi}{Ua}} \qquad L > 5.0, \tag{5.5}$$

Where χ is the thermal diffusivity at the asperity contact and k is the thermal conductivity. The Peclet number describes the speed criterion of a single contact area [191]. The temperature distribution is locally inhomogeneous across the various asperity contacts, and it is difficult to

calculate the absolute value of T_L. But in simpler terms, assuming mixed lubrication with comparable h, it is clear that the temperature T_L is proportional to the normal load and sliding speed. 5 Hz is therefore expected to provide a greater heat generation leading to a higher interfacial temperature between contacting asperities. It has been reported that viscosity of globular protein solution is very sensitive to the temperature [193]. Thus, an increase in speed would be expected to increase flash temperature and decrease the viscosity of the lubricant and thereby weaken the protein aggregation. In other words, the formation of tribofilm could be suppressed. As discussed later, the formation of the tribofilm was far less at 5 Hz compared to 2.5 Hz.

Secondly, the effect of strain rate on lubricant should also be taken into account. Currently, there is some controversy about the effects of strain rate on shear denaturation. The globular protein denaturation has been found to require an extraordinary shear rate up to ~ 10^7 s^{-1} [194]. This suggests the difference in strain rate between 5 Hz and 2.5 Hz is insignificant. However, an increase in strain rate can result in an increase in viscosity of the bovine serum, which may enhance protein aggregation and be responsible for the greater tribofilm formation [193], [195]. Finally, the change in speed could change the lubrication conditions with a change in the Hersey number in going from 2.5 to 5 Hz. For the Ti513 and Ti64 ELI, the change in speed did not change the friction measurably, suggesting that there was no change in the lubrication conditions. Indeed, changes in friction were controlled far more by passivation/depassivation events rather than sliding speed. However, for the Ti413, friction decreased from ~0.5 at 2.5Hz

to ~0.3 at 5Hz. This may suggest a change from boundary lubrication towards a mixed lubrication regime at a higher speed.

5.3.2 On the nature of repassivation

The surface of Ti alloys can form a local galvanic couple as a result of the passive film being removed by the wear process while the surrounding area remains passivated [112], [176], [184], [196]. At 5 Hz, all materials in this study depassivated at the start of the test, Fig.5.3a. The Ti64 ELI exhibited a marginally more cathodic potential than the two β titanium alloys. Although the potential oscillated for the two β titanium alloys during the test, there was no real evidence of repassivation. The potential of the Ti64 ELI gradually increased as the test progressed, becoming the same as the two β titanium alloys at the end, but there was no evidence of repassivation. Thus, at this sliding speed, the time in between asperity contact was too short for passivation to occur. Moreover, the general absence of a tribofilm at 5 Hz limited the ability to repassivate.

The observed oscillation of the potential for the 2.5 Hz test (Fig.5.4) is attributed to the dynamic depassivation and repassivation process. Major differences were seen in the extent of repassivation and the time for repassivation between the Ti413, Ti513 and the Ti64 ELI, Fig.5.4a. As shown in Fig.5.4a, Ti413 depassivated at the start of the test and, although there were major fluctuations in the potential during the test, it remained depassivated throughout. The increases in friction appeared to be associated with the production of plate-like wear debris, Fig.5.6b. The extent of depassivation for Ti513 was less, with a gradual increase in potential throughout the test, reaching near (but unstable) repassivation towards the end of the test after

20 ks sliding. In comparison, the Ti64 ELI test at 2.5 Hz exhibited extended periods of repassivation, but periodic events occurred leading to depassivation. In all cases, the friction coefficient tended to follow the same trend as the potential, for example, the Ti64 ELI exhibited abrupt increases in the friction coefficient associated with the depassivation events.

The extent of depassivation of the Ti413 was similar to that expected from its corrosion behaviour, Table 5.1, with this material exhibiting the poorest corrosion resistance. However, the Ti64 ELI exhibited superior repassivation compared to the Ti513, in contrast to the expectations from the corrosion tests, where Ti513 had the lowest I_p implying a faster repassivation kinetic without mechanical disruption. This result is consistent with that observed by Khan et al. [197], [198], where the extent of repassivation was shown to not follow the corrosion resistance under wear conditions. Indeed, several researchers have shown that proteinaceous solutions affect the dynamic recovery of the rubbing potential, which can lead to better than expected wear resistance [79], [112], [176], [196]. In the current work, there was therefore, some additional reasons for the difference in repassivation behaviour between Ti513 and Ti64 ELI, most probably associated with the manner in which each material reacted with the bovine serum during rubbing. It is believed that this was associated with the difference in materials ability to form a tribofilm on the surface, as discussed below.

5.3.3 Tribofilm formation and relationship to passivation

Tribofilms have been widely found in metal hip prosthesis. As described previously, the formation of a tribofilm could improve corrosion resistance by hindering the transport of oxygen [199]. Where present, a graphite-like structure is also believed to act as a solid lubricant

and is responsible for a lower COF compared to the test without the addition of protein [109], [200]–[202]. Various factors can affect the formation of bio-tribofilm. Zeng et al. [203] reported that a mechanically polished CoCrMo could form thicker bio-tribofilms in comparison to electropolished samples. In other words, the residual stress and difference in surface topography have significant effects on the formation of bio-tribofilm. Wang et al. [204] also found rubbing at cathodic potential was more likely to form thicker bio-tribofilms than at anodic potential because the increased potential decreased the adhesion between protein and surface. The phenomenon also explained the reason for the discontinuous distribution of the bio-tribofilm during the tribocorrosion test. However, these studies mainly focus on CoCrMo and the process of the formation of bio-tribofilm in Ti alloys is not fully understood.

SEM images of the worn surface showed regions of darker contrast, e.g., Figs.5.6b, 7b. As discussed below, these regions of darker contrast were associated with the formation of a tribofilm. The extent of the tribofilm was a strong function of sliding speed, with the tribofilm extensively found on surfaces tested at 2.5 Hz, but much less so on surfaces tested at 5 Hz, for example, compare the worn surfaces for Ti513 in Fig.5.7a and b. As discussed in section 5.3.1, the primary effect appeared to be that the increase in speed increased flash temperature thereby decreasing the viscosity of the lubricant and thereby weakening the protein aggregation, resulting in a suppression of the formation of the tribofilm.

TEM examination of site-specific surface cross-sections showed that the regions of dark contrast in the SEM images corresponded to the formation of a surface tribofilm, Figs.5.10, 11. Detailed chemical analysis by EELS indicated that the tribofilm consisted of carbonaceous

material containing nanoparticle wear debris. The main composition of the matrix of the tribofilm was graphite-like carbon, as shown by the fine structure in the EEL spectra, suggesting that the protein underwent carbonisation/denaturation during tribological contact. It has been reported that the structural stability of protein is associated with various parameters, such as temperature and ionic strength [205]. There was also minor amounts of oxygen in this film which might be thought to be associated with repassivation events of the titanium surface. The oxygen was associated with very fine particles within the carbon-based matrix. For the Ti513, these particles contained calcium and titanium as well as oxygen. This suggests some form of mechanical mixing between titanium wear debris and the bovine serum. It is known that nanoparticles can rapidly interact with proteins because of a higher surface area and enhanced chemical reactivity [206]. The incorporation of these hard oxide particles could reinforce the soft carbonaceous layer. This may produce a more robust tribofilm, enhancing the staged repassivation behaviour.

It could be assumed that these oxide nanoparticles in the tribofilm were mainly from the breakdown of the compact titanium oxide-based passive film, which was continuously formed when the fresh surface was exposed to BCS solution during tribocorrosion. However, despite extensive TEM investigation, no evidence was found of a passivating titanium oxide layer. Thus, mechanical disruption and chemical action together contribute to this complicated tribofilm, with the formation of the tribofilm illustrated in Fig.5.14.

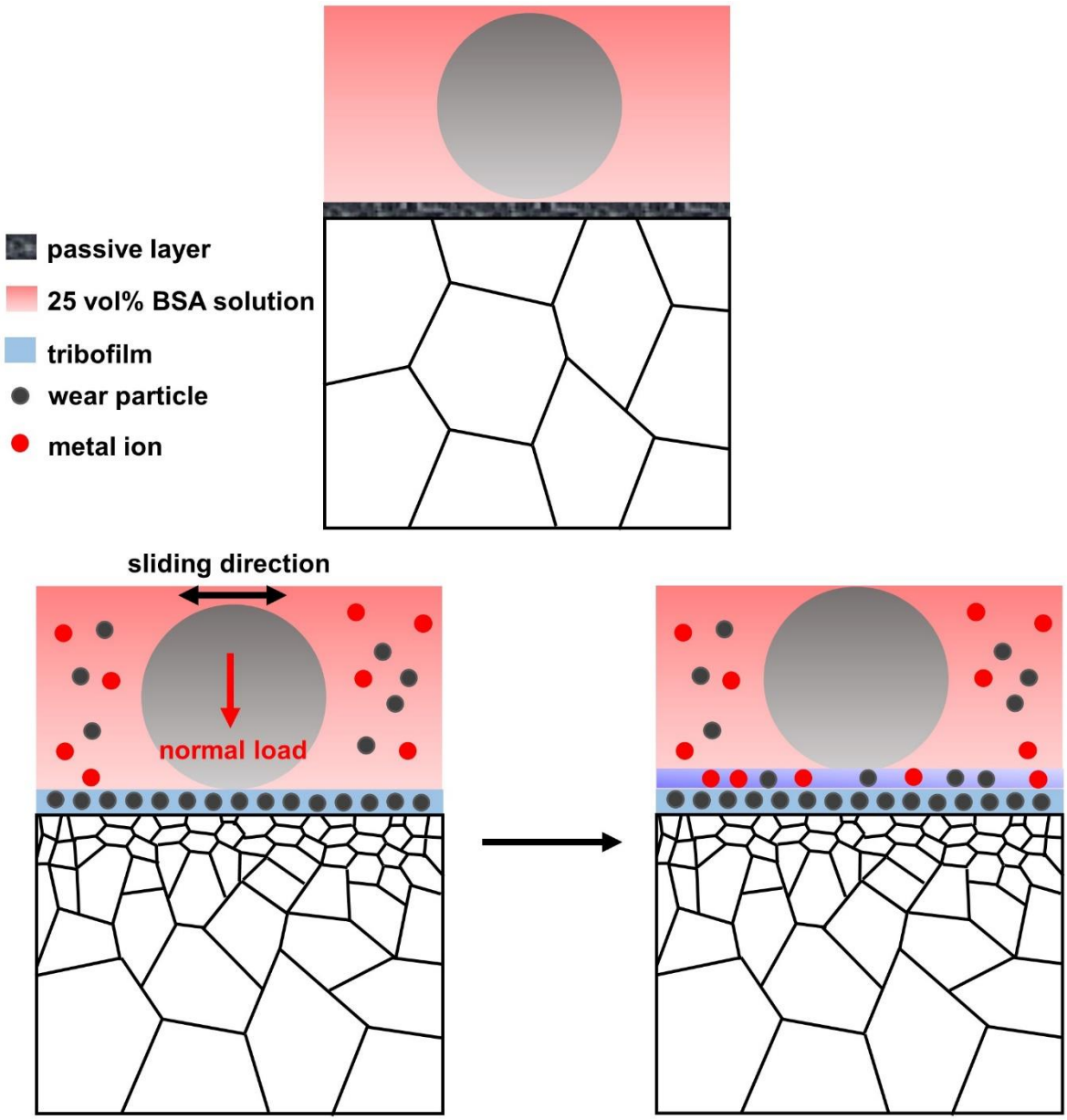

Fig.5. 14. *Schematic illustration of subsurface evolution after the tribocorrosion test.*

The structure of the tribofilm also appeared to be a function of the material, with a two-layer tribofilm found on the surface of the Ti64 ELI (Fig.5.11) compared to the single-layer tribofilm found on the Ti513 (Fig.5.10). The extent of formation of the tribofilm therefore appears to be closely correlated with the extent of repassivation observed during the sliding tests (Figs.5.3, 4) and with the material type. Thus, the current work strongly suggests that the tribofilm

formation is the precondition for repassivation and is responsible for the stronger and stable passive recovery. The formation of the tribofilm and associated repassivation leads to less material loss, thus implying the tribofilm offers protection of the surface to the wear induced mechanical disruption. This is consistent with the work of Khan and Williams [207], who found that the presence of protein reduces the wear rate of all alloys but that the extent was very much alloy dependent.

5.3.4 The effects of sliding speed on the nanocrystalline layer

Apart from the tribofilm, the subsurface microstructure can play a crucial role in controlling wear performance through friction-induced changes that alter the mechanical properties of the surface. As summarised in a review of the effect of fine, and ultra-fine grained structures on wear, Gao et al. [208] showed how such structures could sometimes improve wear resistance, while under different conditions can reduce wear resistance. Improvements in wear resistance are associated with the refined microstructure leading to the greater strength of the surface. However, decreased wear resistance can be a result of decreased ductility, reduced work hardening capability, a greater grain boundary area accelerating corrosion/oxidation and a strain incompatibility with the substrate. There are several examples where a nanostructured surface can give greatly enhanced wear resistance. For example, Chen et al. [209] found that a gradient nanostructure possessed a better capacity of strain accommodation, which reduced ploughing and delamination during dry sliding, leading to a lower COF and superior wear resistance.

In the current work, all samples underwent the same number of cycles and so surface structures can be directly compared. The cross-sectional view of Ti64 ELI worn surface found the thicker nanocrystalline layer formation at 2.5 Hz than at 5 Hz, Fig.5.12. The lower sliding speed was associated with a significantly smaller material loss, Fig.5.5, giving a smaller geometry of the wear track. This would reduce the Hertzian contact pressure compared to the test at 5 Hz, which would be expected to give less surface deformation and, therefore a thinner nanocrystalline layer. However, the opposite was observed.

An interesting observation, particularly for the Ti64 ELI, was that the depth of the nanocrystalline layer was greater where there was a thicker tribofilm on the surface. In particular, the nanocrystalline layer was much thicker when the double tribolayer was present, Fig.5.13. For all materials, the tribofilm was more extensive at 2.5 Hz compared to 5 Hz, which was coincident with a thicker nanocrystalline layer and a lower wear rate. There are several reports for thicker nanocrystalline layers being coincident with a surface film, such as an oxide or tribofilm. For example, Mischler and co-workers have shown a much thicker nanocrystalline layer in the friction of stainless steel for anodic conditions, where an oxide was present, compared to cathodic conditions in the absence of an oxide [210], [211]. It was believed that the surface film acts as a barrier to dislocation glide and dislocation annihilation at a free surface, leading to the formation of a nanocrystalline layer to a greater depth.

5.4 Summary

In this Chapter, the tribocorrosion performance of designed Ti alloys and Ti64 ELI were investigated at 5 Hz and 2.5 Hz under OCP condition. Some main findings can be summarised as follows:

- An improvement of the corrosion resistance was confirmed in Ti513.
- At 5 Hz, Ti513 showed the lowest specific wear rate, and all alloys displayed an abrasive-dominated wear mechanism.
- At 2.5 Hz, repassivation in the form of potential recovery and stabilization of COF was observed in Ti513 and Ti64 ELI. This was mainly attributed to the formation of tribofilm, which entrapped wear debris and increased strain accommodation capacity, resulting in less material loss.
- It should be recognized that Ti alloys have poor abrasion resistance. Although the generation of hard wear debris could be partially entrapped, it cannot essentially meet the clinical requirement to perform as a bearing component.

Chapter 6 Mechanical Properties and Deformation Behaviour of Ti-6Al-4V ELI after SLM Treatment

6.1 Introduction

The newest projection from the United Nations reveals that world population ageing will introduce more than twice the current number of people aged 65 or over by 2050 [212]. It creates a heavy burden of joint replacements to the increasing population, such as total hip replacements (THRs) and total knee replacements (TKRs). This is because osteoarthritis (OA) is regarded as the primary reason for most joint replacements (e.g. hip and knee), and morbidity is strongly associated with the increasing age of persons [1], [82], [125], [179]. There are over a million primary and revision procedures taking place around the world annually, and the primary procedure is increasingly in younger patients. It thus remains urgent to develop new implant materials with enhanced durability. Ti alloys, thanks to the combined high specific strength and superior biocompatibility, are widely used for metallic implants. However, the poor bio-tribological behaviour, as a result of their intrinsic properties, limits their further development in orthopaedic implants [9].

In this work, I designed a new texture on the surface of Ti64 ELI based on selective laser melting (SLM). The mechanical performance of the laser-treated surface was examined via nanoindentation, EBSD mapping and TEM techniques and more information concerning

tribocorrosion behaviour, as well as structural evolution of subsurface, were discussed in Chapter 7.

6.2 Results

6.2.1 Surface morphology

Fig.6.1 shows a top view of the SLM surface at low magnification. The resulting width and hatch spacing of tracks are around 90 and 208 μm, which are close to the processing parameters described in Chapter 3. It was also found there were no visible defects such as balling and thermal cracks on the surface, and the interaction of each track looked very sharp, indicating a smooth surface finish.

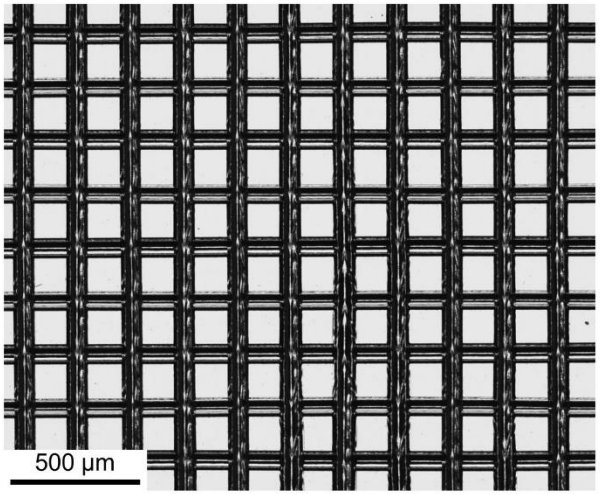

Fig.6. 1. *Optical micrographs of SLM surface from normal direction.*

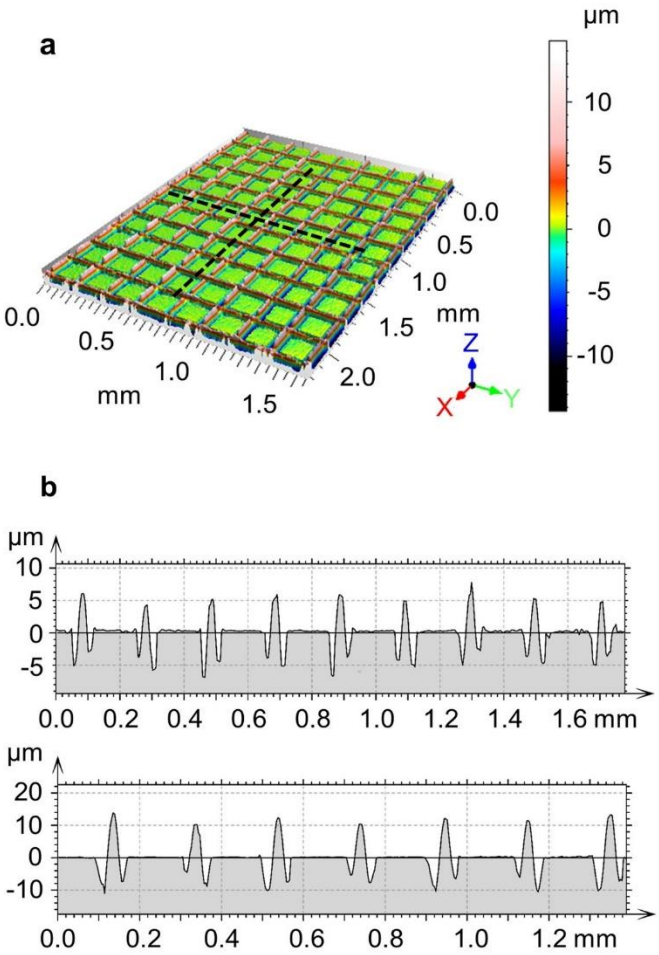

Fig.6. 2. *(a) 3D optical topography image of treated surface. (b) Corresponding profile curves along scanning directions (indicted in dashed lines).*

The 3D optical topography image (Fig.6.2a) suggests that the SLM surface has a uniform structure similar to riblet geometry, in which each successive protrusion along the scanning direction is surrounded by trenches on both sides. The cross-sectional profiles taken from X and Y scanning directions (Fig.6.2b) further confirms that the heights of micro-protrusions across the two scanning directions were ~10 and ±5 μm for X and Y scans, respectively, and the depth of trenches was from 5~10 μm. The comparison of XRD patterns between SLM and the untreated surface is presented in Fig.6.3a, showing that the α+β phase constitution did not

change after SLM. The enlarged profile of α (002) and α (101) in the inset figure shows that the SLM sample has an increase in the full width at half maximum (FWHM) in terms of the shift towards higher diffraction angles, which indicates a slight lattice shrinkage and thus suggests the formation of martensitic structure inside the molten zone [213]–[215]. The cross-sectional EBSD investigation shown in Fig.6.3b gives more representative evidence that the remelted microstructure consists of non-equilibrium acicular α′. It should be noted that α′ is still indexed as α phase in EBSD map because the lattice parameters of α′ are very closed to that of α phase, and the lattice parameter is variable depending on the thermal gradient during solidification.

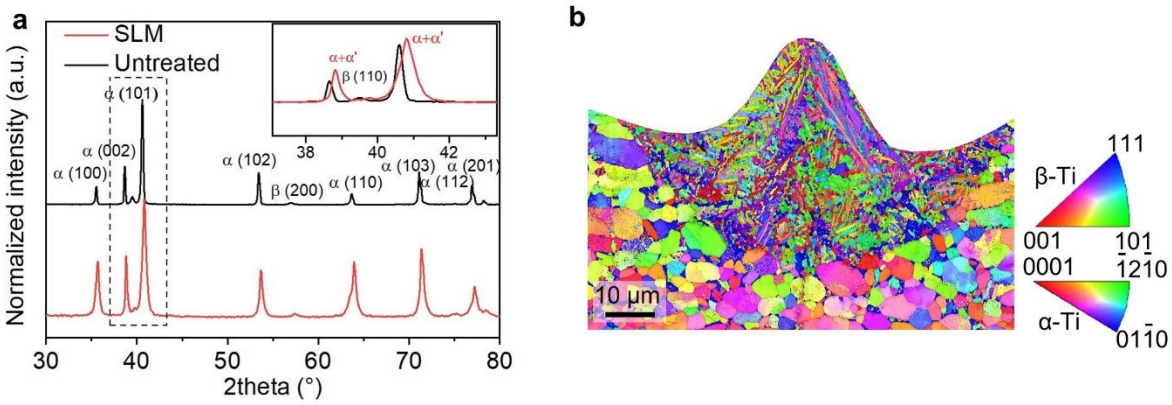

Fig.6. 3. *(a) XRD patterns of untreated and SLM samples, the magnification of α (002) and α (101) peaks is shown in the inset. (b) EBSD Inversed pole figure (IPF) + Image quality (IQ) image of the cross-section of SLM surface.*

6.2.2 Hardness and elastic modulus mapping

Given the gradient structure from surface to substrate, cross-sectional nanoindentation mapping of the SLM sample was performed to examine local mechanical properties.

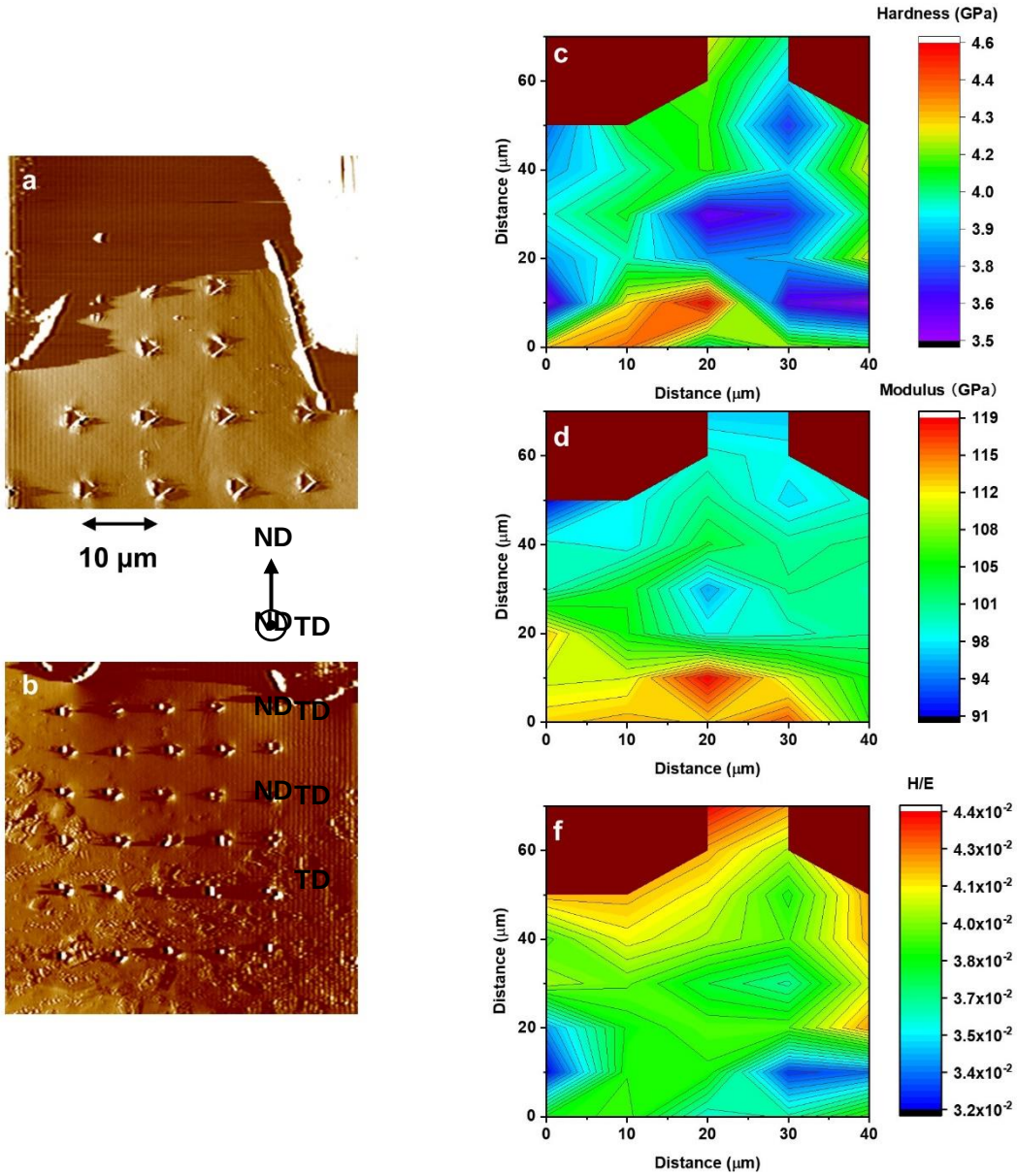

Fig.6. 4. *Nanoindentation analysis of SLM surface. (a) and (b) Atomic Force Microscopy images illustrating the distribution of indents in cross-section. (c-f) Corresponding hardness (H), reduced elastic modulus (E) and H/E map of the target area.*

As shown in Figs.6.4a-b, the array of indents covers protrusion as well as the substrate with an interval spacing of 10 μm. The protrusion region has a homogenous distribution of hardness and modulus around 4.0 GPa and 94 GPa respectively. In contrast, the substrate exhibits localised softening and hardening, the hardness ranged from 3.5 to 4.6 GPa and modulus ranged from 91 to 119 GPa. This inhomogeneous distribution is attributed to the presence of transformed β phase, which is softer than the primary α phase (Fig.4.1b). Generally, harder material presents better wear resistance [216], [217]. However, this assumption is found to be not applicable to some materials with ultralow stiffness, such as elastomers. The high ratio of hardness to modulus (H/E) has been regarded as a suitable parameter for indicating good wear resistance [218], [219]. Thus, another H/E map is also presented in Fig.6.4f, and it is found that the protrusion region exhibits a higher value than that of the substrate.

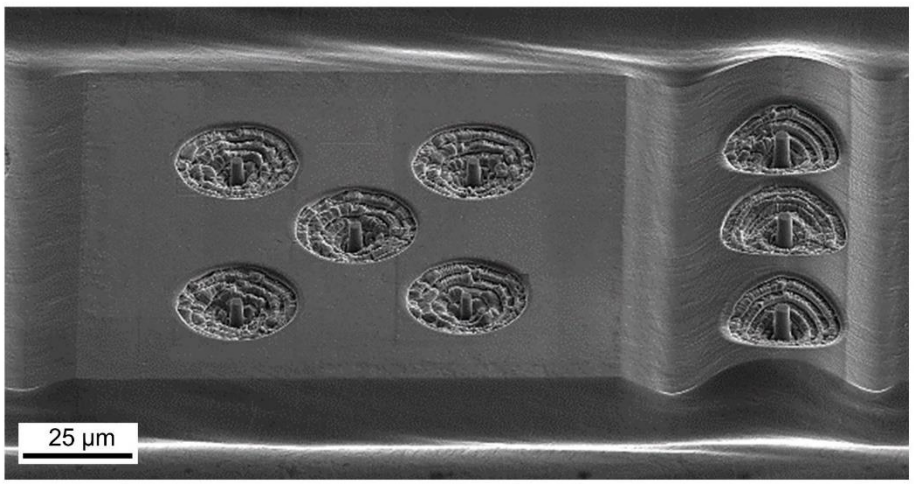

Fig.6. 5. *Schematic illustration of micropillars on SLM and untreated surface prior to compression.*

6.2.3 Comparison of stress-strain behaviours of untreated and SLM-treated surface

To further understand the mechanical performance of the SLM surface, *in-situ* uniaxial compression tests of micropillars were conducted on the untreated and SLM-treated surfaces. As shown in Fig.6.5, SLM micropillars are located along the top surface of protrusion, while untreated surface micropillars are well away from potential SLM effects. Figs.6.6a-b shows SEM images taken from video recordings of the deformation stages of micropillars compressed to ~18%. The untreated surface clearly shows that successive slip steps initiated firstly from the top left of the pillar at a strain of 4% (indicated by a red arrow). With a further increase of strain to 9%, the lower right region also began to form another group of slip step. This heterogeneous behaviour was associated with the strain gradient inside the pillar (decrease from top to bottom), and the different critical resolved shear stress (CRSS) to activate dislocation motion in grains with different orientations. The yield point on the stress-strain curve for the untreated surface pillar is highlighted, and the yield strength was measured to be 993 MPa.

In contrast to the shear localization observed in the untreated surface, the SLM pillar had a more homogeneous flow behaviour during the compression test. There was no evidence of macroscopic slip steps at a strain of 9 %, which was consistent with a significantly higher yield strength (1731 MPa). Even when the strain was increased to 18%, only slight bending of the pillar was observed and the right-lower edge exhibited surface undulations, with no slip steps

found. This therefore demonstrates an attractive strengthening effect from nanocrystalline martensite.

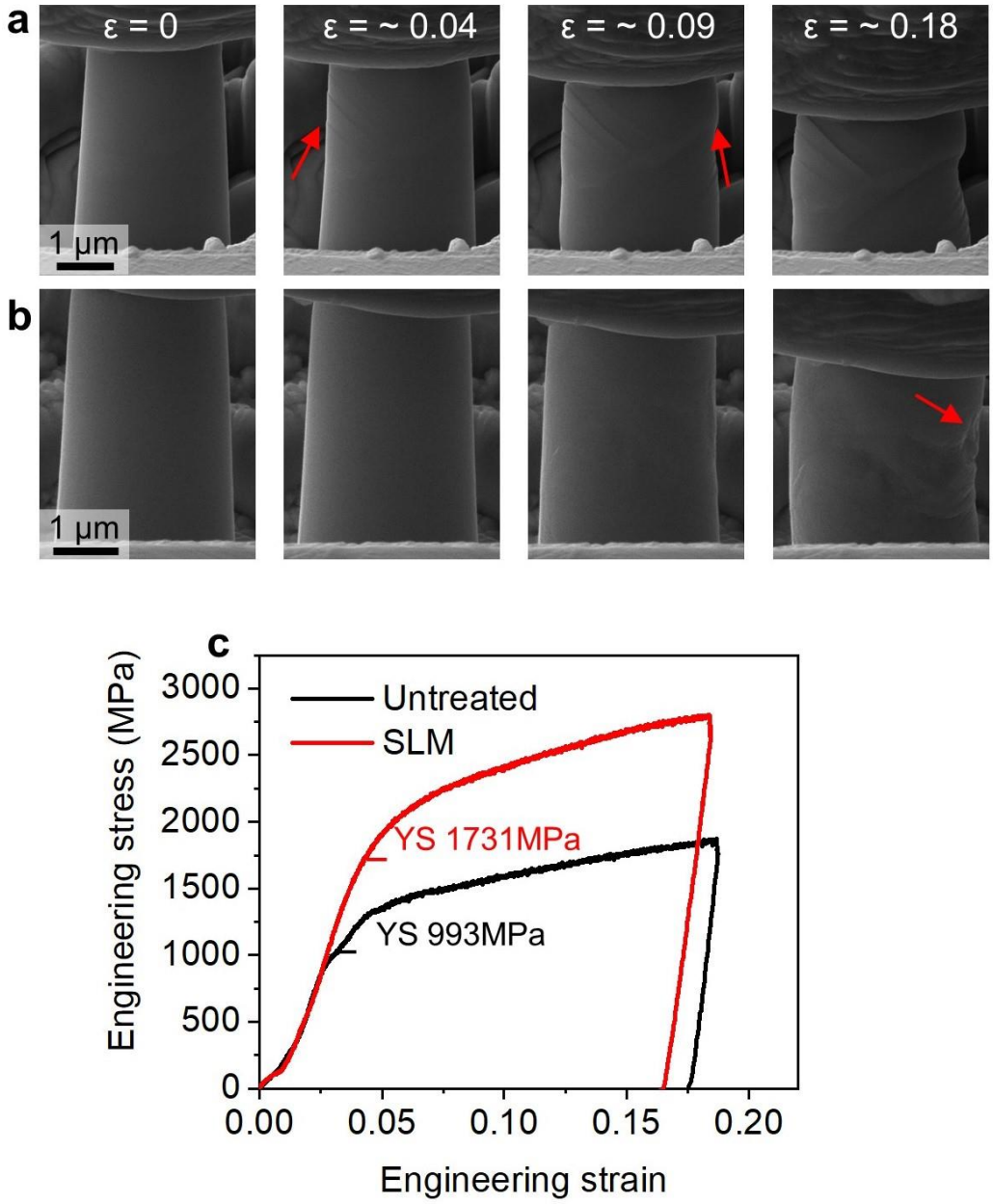

Fig.6. 6. *In-situ compression tests of untreated surface and SLM micro pillars at room temperature: SEM images of real-time deformation stages of (a) untreated and (b) SLM respectively. (c) Corresponding stress-strain curves.*

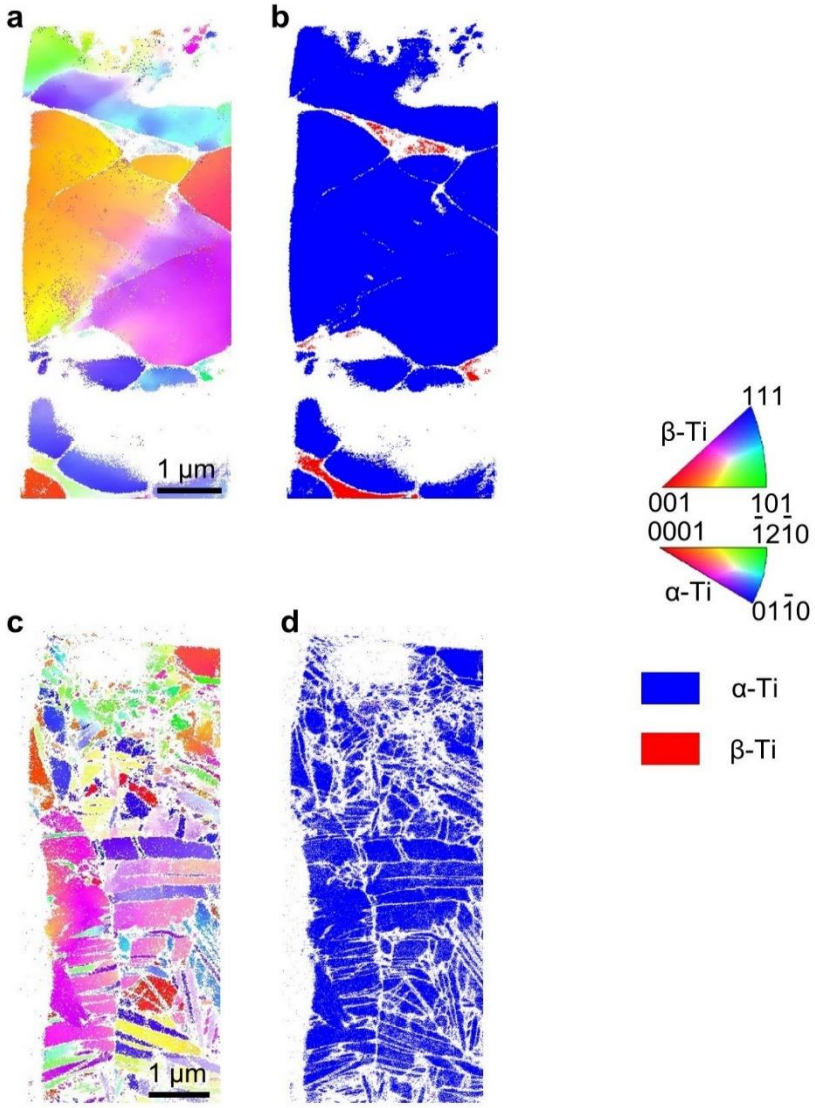

Fig.6. 7. *TKD analysis of compressed micropillars: (a) IPF image of the untreated surface pillar and corresponding phase map (b). (c) IPF image of SLM pillar and corresponding phase map (d).*

6.2.4 The microstructure of deformed untreated surface and SLM micropillars

After compression tests, deformed pillars shown in Fig.6.6 were thinned via FIB for further structural characterisations. Transmission Kikuchi Diffraction (TKD) analysis using the Nanomegas system on the Jeol F200, Fig.6.7a and c, provide an overview of the deformed microstructure. Firstly, it should be noted that insufficient diffraction was obtained in some thinner regions to allow crystal orientation analysis, which appeared white in the image. There were no visible deformation bands in the pillar from the untreated surface (Fig.6.7a), which confirms that the main deformation mechanism was dislocation slip. In contrast to this, the SLM pillar (Fig.6.7c) structure was refined and directional, as expected from the EBSD map. Again, thin regions of the sample could not be indexed. It is also worth noting that there was no β phase in SLM micropillar in contrast to the untreated surface micropillar, as shown in the corresponding phase map (Fig.6.7d). This could be explained by the heating that gives a single phase that completely transforms to martensite on rapid cooling and suppresses the formation of the β phase.

It has been reported that many factors such as the morphology of the α/β interface and corresponding Burgers orientation relationship can strongly affect the CRSS for slip activation and transmission. A higher volume of β phase inside a single pillar usually leads to lower strength and poor hardening. Still, the phase boundary is usually better at acting as an obstacle to dislocation motion and provides sites for dislocation pile-up [220], [221].

Thus, it is important to perform several compression tests to see the variability in behaviour. The measured average YS of the untreated surface pillar after five tests was 978 ± 16 MPa, and that value of SLM was 1650 ± 75 MPa. The untreated surface value was 126 MPa larger than the value measured by the tensile test (852 MPa). This may be due to the small sample area for the micropillars but may also be a result of the sample size dependence effect.

To further investigate the deformation mechanisms, high-resolution TEM analysis was performed on the above TKD samples. Fig.6.8a shows a bright-field TEM image of the untreated surface pillar, in which grain structure is consistent with IPF image in Fig.6.7a and no shear bands were observed. The HRTEM micrograph indicated by the dashed box was selected for closer examination.

As shown in Fig.6.8b, the apparent grain boundary is identified and highlighted by the dashed line. Around the boundary, a square area was selected for further inverse fast Fourier transform (IFFT) using the applied mask of the (1-10-1) plane (Fig.6.8c). It was determined by the presence of edge dislocations as well as distorted plane fringes (indicated by dashed circles). However, it should be pointed out that distortion of the fringe contrast in coherent HRTEM images like this can arise from thickness variations in the sample and bending distortion of the sample. In this case, thickness changes are very unlikely over this length scale with a FIB prepared sample. Although undulations could be present, this appears unlikely as these would be expected to run across the sample, which was not the case here. Thus, it can be concluded that plastic deformation is accommodated by dislocation slip, with grain boundaries acting as barriers when the applied stress increases to reach the CRSS.

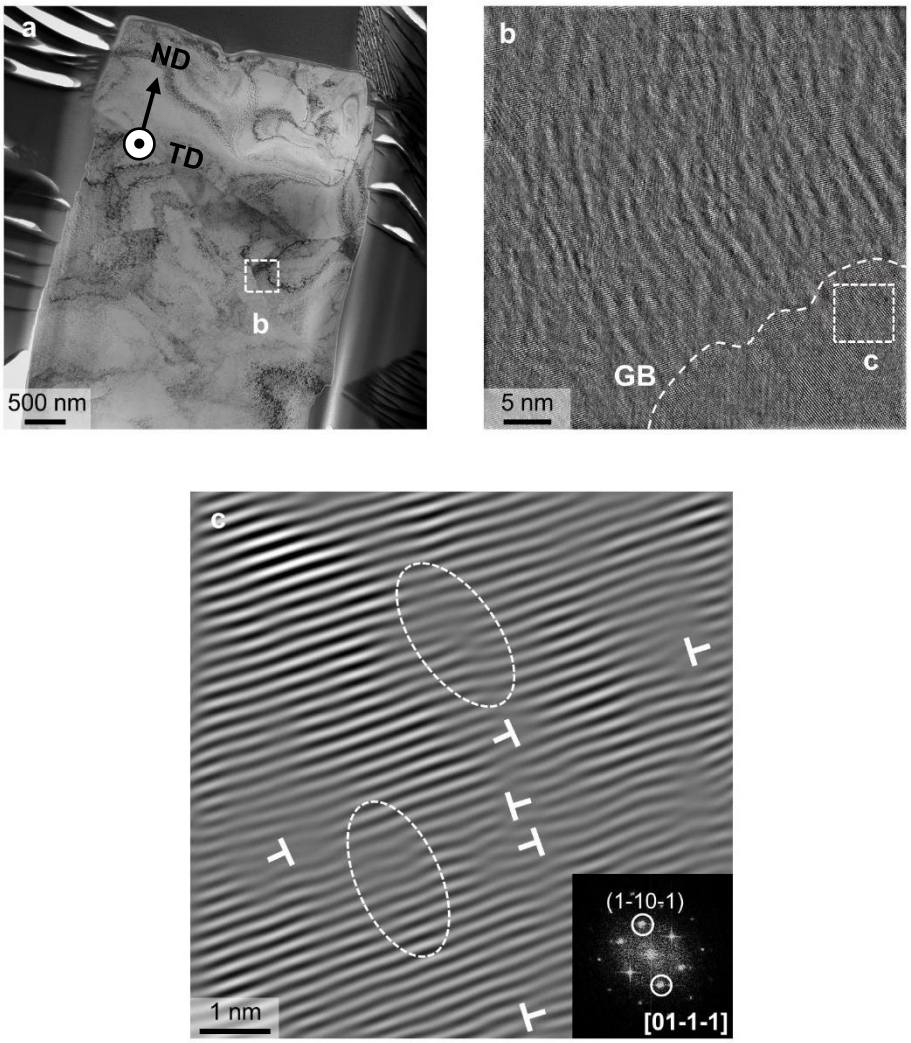

Fig.6. 8. *The deformed microstructure of untreated micropillar: (a) BF image of the deformed pillar. (b) HRTEM selected from a dashed box in (a). (c) IFFT using FFT (inset of (c)) from dashed box in (b).*

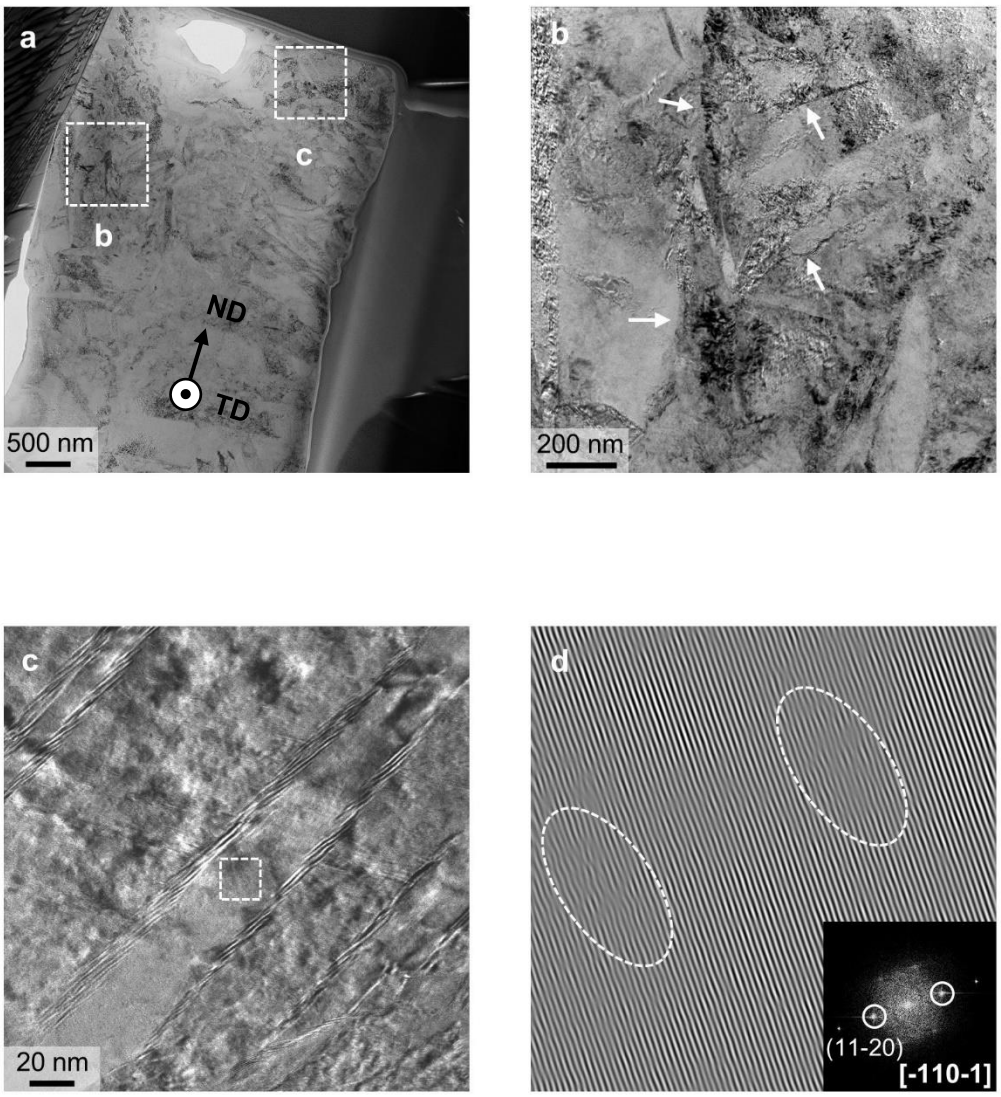

Fig.6. 9. *The deformed microstructure of SLM micropillar: (a) BF image of the deformed pillar. (b) Enlarged BF image selected from the dashed box in (a). (c) HRTEM image selected from the dashed box in (a). (d) IFFT using FFT pattern (inset of (d)) showing an internal atomic structure of martensite.*

For the SLM pillar, profuse α′ martensite is seen, in agreement with the TKD results (Fig.6.9a). Fig.6.9b displays a closer examination of the deformed structure corresponding to the dashed frame in Fig.6.9a. There is a high density of dislocation tangles near the nanograin boundaries

(as indicated by arrows). Additionally, HRTEM from the dashed frame in Fig.6.9c reveals the formation of smaller nanograins with a width that ranged from 10 to 30 nm. The deformation mechanism inside these grains was examined through FFT and corresponding IFFT images. Fig.6.9d shows the IFFT image using applied mask of (11-20) plane in FFT pattern along zone axis [-110-1], in which only lattice distortion was observed with no visible dislocations. Considering the presence of high density of nanograin boundaries, i.e., nanograin boundary, the dislocation starvation often observed in single-crystal micropillar is excluded, and boundary migration should be responsible for the stain accommodation [222].

6.3 Discussion

6.3.1 The formation mechanism of riblet geometry

From the thermal fluid dynamics point of view, the topography during the SLM process is mainly associated with the synergistic actions of recoil pressure and Marangoni effects. During laser scanning, the recoil pressure from the laser beam will firstly generate a depression on the surface where it begins to melt. The accompanying temperature and surface tension gradient inside the molten pool can generate a flow vortex and eventually result in various surface topographies on subsequent cooling [144], [223], [224].

It is believed that the fine adjustment of fast scanning speed (3000 mm/s) and laser power (130W) plays a leading role in suppressing mass transfer around the edge of the depression and trenches are therefore formed. The most common parameter to describe laser melting is volumetric energy density (VED), which could be expressed as the following equation:

$$VED = \frac{P}{vdh} \left[\frac{J}{mm^3}\right] \quad (6.1)$$

Where P is laser power, v is scanning speed of laser beam, d is laser beam diameter and h is the hatch spacing distance. It has been reported that VED has a significant effect on the microstructure during the power-bed fusion process. Carmen et al. [225] investigated the microstructure evolution of the Ti64 component using VED from 24.2 to 71.4 J/mm^3. It was found that relatively lower VED was favourable to the formation of random martensite variants and grain refinement. In the current work, the calculated VED was 7.2 J/mm^3, much smaller than the reported lowest value (24.2 J/mm^3), which explains the formation of an extremely refined grain structure (Fig.6.9c).

However, from the author's viewpoint, the calculation of the effective VED still needs further optimisation due to the difference in energy loss between single track scenario and additive manufacturing conditions. Laser melting undergoes energy input and energy loss, such as reflection from the polished surface. Umberto et al. [226] compared laser tracks with various VED on 316L stainless steel. It was found that VED cannot effectively predict the transition from conduction to keyhole mode, which means large attempts are required to minimize defects during processing [227].

6.3.2 Correlation between deformation mechanism and enhanced strength

It has long been recognised that phase interfaces and grain boundaries are major obstacles for dislocation motion that strongly control plastic accommodation in polycrystalline materials [228]–[230]. The smaller grain size increases yield strength by hindering the activation of dislocation from grain boundaries, according to the classic Hall-Petch effect [231]. In the compressed untreated surface pillar, slip traces imply a lot of dislocation activity on one slip plane, which is commonly associated with the deformation of large grains at low strains. Two types of lattice distortion corresponding to edge dislocations and distorted lattice plane were observed in one-dimensional {1-10-1} plane fringes, which revealed severe strain localization at the grain boundary (Fig.6.8). A similar phenomenon has been previously reported in commercial titanium. It was also found that the type of slip event (transfer or pinning) is strongly related to the geometric alignment of the slip system [232]. Thus, the active deformation mechanism was a classical sequence of dislocation nucleation, propagation and interaction with grain boundaries in response to increasing stress. Additionally, the occurrence of the distorted plane in crystal lattice, also known as nanodisturbances and widely observed in Gum metal and β Ti alloys, signified that {1-10-1} had very low shear resistance, implying the main reason for poor wear resistance in Ti alloys [233], [234].

Rapid solidification during SLM could lead to the formation of martensitic transformation. In the current work, a single layer scanning strategy not only reduces the risk of defects such as cracks and pores caused by energy and strain accumulation but also results in the finest martensitic structure to some extent [235], [236]. From EBSD and HRTEM results, the grain

size inside the remelted region ranged from ~20 to hundreds of nanometres. Therefore, a much higher grain boundary density was introduced. Finer nanostructure implies a lower dislocation density on a particular slip plane and limited dislocation propagation across grain/phase boundaries such that slip steps were not seen at an early deformation stage. The smaller grains would then rotate as deformation continued leading to other slip systems being activated, and the chance of seeing slip steps was greatly reduced. From dislocation-free observation within fine-grained martensitic laths (Figs.6.9c-d), grain boundary mediation is shown to dominate the deformation rather than dislocation slip. This is often termed an "inverse" Hall-Petch effect, which includes grain rotation, migration and sliding, and happens when the grain size is below 40 nm [237]. However, the SLM surface still exhibited nearly 70% greater YS compared with the primary equiaxed structure. This suggests that the average length scale of current grains is very close to the characteristic value $d_{c,}$ which is in the crossover regime [237]. Additionally, thicker nanodisturbances containing about 10 fringes were observed, which can be regarded as another response to increasing plastic flow. Thus, it can be concluded that the deformation mechanism of the SLM pillar was associated with limited dislocation slip, as well as grain boundary sliding, the extent of which depends on the local grain size.

Recently, the Kernel Average Misorientation (KAM) representing local stain distribution was widely used to estimate the density of geometrically necessary dislocation (GND) [167], [238], [239]. In the current work, we did not display the KAM map because ion milling preparation may introduce strain and surface damage even when the final polishing current is below 100

picoamperes. This also explains why measured strength is slightly larger than bulk conditions [240], [241].

6.4 Summary

In summary, the topography of surface after SLM, mechanical properties and deformation mechanism of SLM and untreated surfaces were compared and investigated. The main findings can be summarised as follows.

Single-layer laser scanning based on the appropriate combination of processing parameters effectively suppresses the formation of defects and generates a riblet-like topography. The remelted region consists of acicular α′ martensite, which presents a 70% higher strength than the primary equiaxed structure. The difference in this improvement between the untreated surface and SLM samples can be clearly explained by the deformed structure. The untreated sample exhibits a classic dislocation deformation mechanism, in which dislocations nucleate and propagate, either escaping from the surface or being blocked by grain boundary barriers. In contrast, the deformation mechanism of SLM is characterised by both dislocation and boundary events which depend on the grain size.

Chapter 7 Tribocorrosion Behaviour of Ti-6Al-4V ELI after SLM Treatment

7.1 Introduction

Synergistic effects between mechanical damage and corrosion could contribute to the release of metallic ions after short-term implantation. This is often termed an adverse reaction to metal debris (ARMD) [4]. Recent studies showed ARMD not only frequently appeared in metal-on-metal (MoM) THRs but also non-MoM THRs, such as ceramic-on-metal and metal-on-polyethylene configuration [3]. The aggravated abrasive wear caused by third-body wear debris could decrease the service life of the implant. By comparing tribocorrosion behaviour between Ti-12Mo-6Zr-2Fe (TMZF) and Ti-6Al-4V ELI (Ti64 ELI), Yang et al. [75] found the unacceptable release of wear debris was attributed to the lack of strain hardening in TMZF. The organic layer formation (also called a tribofilm) on the metal surface was always observed in taper junction [126]. However, current results only revealed that the formation of the film could be affected by surrounding potential distribution as well as the residual stress of starting surface conditions. It is still not completely understood whether such tribofilm layers can increase wear resistance [111], [124], [199], [203], [242], [243].

In this chapter, tribocorrosion performance for the untreated and SLM samples tested at reciprocating-sliding frequencies of 5 and 2.5 Hz was examined. The formation mechanism of tribofilm and structural evolution of subsurface were discussed in detail.

7.2 Results

7.2.1 Electrochemical behaviour

7.2.1.1 Open circuit potential (OCP)

The evolution of OCP versus time for untreated and SLM samples was measured in BSA solution at 37 ℃ for 30 min (Fig.7.1). It can be seen that both curves display a similar shift towards the noble region, implying a continuous formation and growth of passive film [113]. Table 7.1 shows that the mean OCP value of the SLM sample (-176 mV) is more positive than that of the untreated surface in a protein-containing solution, indicating a better protection characteristic of the passive film. Similar behaviour was also observed in nanostructured Ti produced by Equal-Channel Angular Pressing (ECAP), a common severe plastic deformation method to obtain ultra-fine grains in metals. However, it is worth noting that the corresponding crystallographic texture may introduce electrochemical anisotropy [244]. In this study, it is unrealistic to investigate localised electrochemical performance because samples could not be prepared from the remelted area (i.e., protrusion and recess).

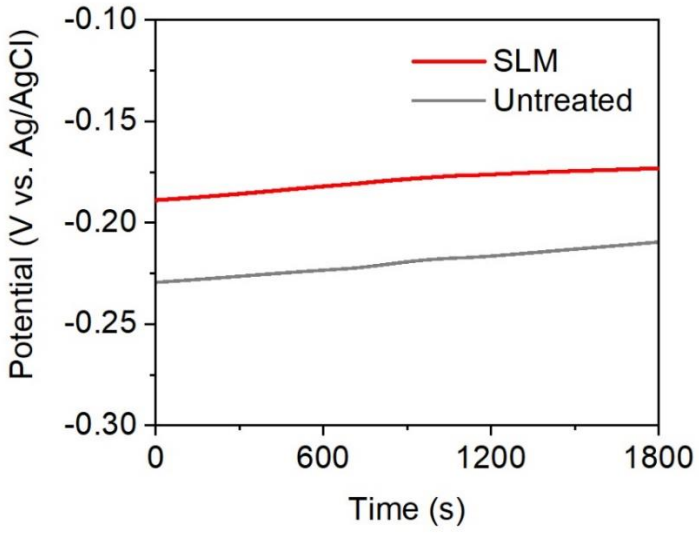

Fig.7. 1. *OCP curves for the untreated and SLM samples.*

Table 7. 1 *OCP values for untreated and SLM sample in PBS solution containing proteins.*

Sample	E_{ocp} (mV)
Untreated	-230 ± 32
SLM	-176 ± 13

7.2.1.2 Potentiodynamic polarisation

Fig.7.2 presents the potentiodynamic polarisation curves for untreated and SLM samples. In the cathodic region, the current density was initially determined by the removal of the passive film and subsequent reduction of oxygen. After that, they both displayed a similar active-passive transition and self-passivation behaviour. No breakdown potential or pitting was observed until the upper limit of scanning potential was reached, implying a very stable passive condition of untreated and SLM surfaces in protein-containing solution at 37 ℃. Furthermore, the SLM possessed a more positive E_{corr} (-0.54 V for SLM and -0.66 V for untreated) and wider passive range (0.25 – 1 V for SLM and 0.61 – 1 V for untreated) while similar values of I_{corr} (0.049 μA/cm^2 for SLM and 0.033 μA/cm^2 for untreated) were detected. For better comparison, the mean values of corrosion parameters with standard deviation are shown in Table 7.2 and in good agreement with the above findings. Thus, given these observations, it can be concluded that the SLM sample exhibits faster repassivation kinetics, suggesting an enhanced corrosion resistance.

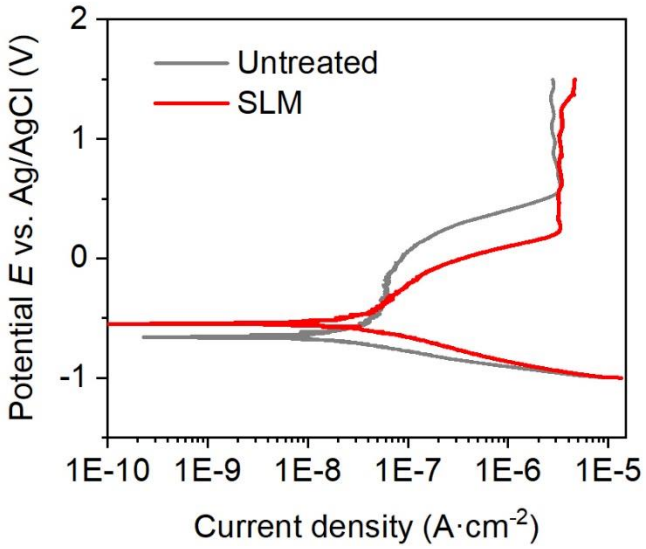

Fig.7. 2. *Potentiodynamic polarisation curves for untreated and SLM samples.*

Table 7. 2. *Corrosion parameters of SLM and untreated samples in potentiodynamic polarisation.*

Sample	E_{corr}	I_{corr} (μA/cm^2)	I_p (μA/cm^2)
Untreated	-0.632 ± 0.045	0.035 ± 0.008	3.485 ± 0.089
SLM	-0.584 ± 0.033	0.041 ± 0.009	3.319 ± 0.073

7.2.2 Tribocorrosion behaviour

7.2.2.1 Tribocorrosion under OCP conditions at 5 Hz sliding frequency

Tribocorrosion behaviour of SLM and untreated samples were firstly examined under OCP condition at a frequency of 5 Hz. Figs.7.3a-b give time dependence of the COF and OCP variation during reciprocating motion. The COF of the untreated sample exhibited a slow downward trend from 0.3 to 0.2 throughout the whole test, resulting in a mean value of COF around 0.25. A similar COF value around 0.25 was also established after an apparent run-in

period in the SLM sample. The potential, Fig.7.3b, exhibited a sharp drop at the start of sliding for both samples, associated with the mechanical disruption that instantaneously destroyed the passive surface layer. It can be seen in Fig.7.3b, the OCP value of the SLM sample oscillates at ~ -0.4 V, which is much smaller than that value of Ti64 ELI (at ~ -1.0 V). This nobler value can be attributed to the reduced exposed contacting surface area due to the laser texture, which contributes to pronounced tribocorrosion performance.

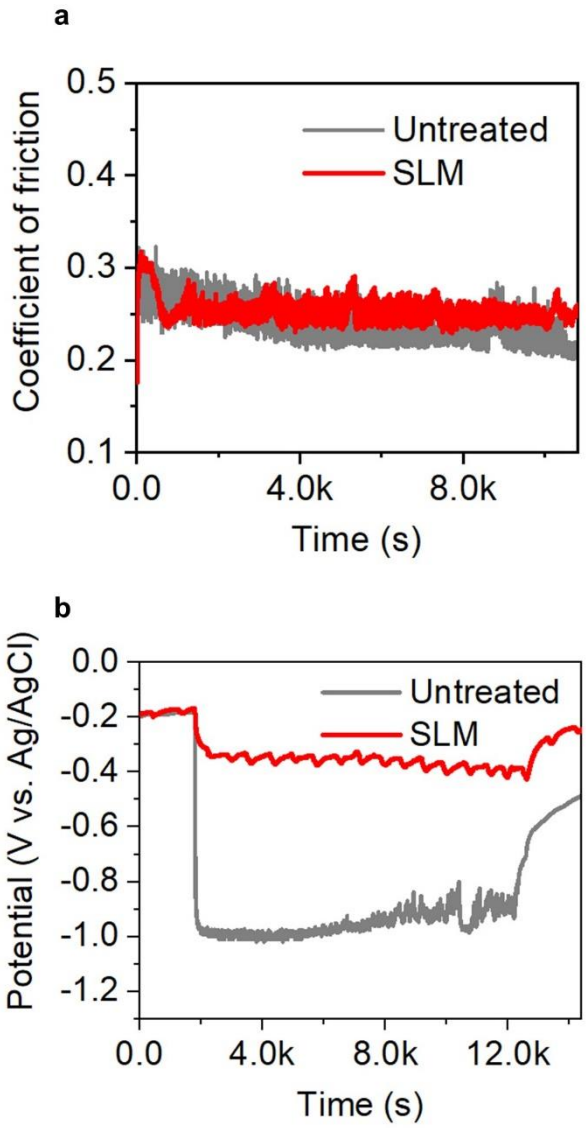

Fig.7. 3. *The evolution of the COF (a) and the OCP (b) during the tribocorrosion test at 5 Hz.*

To understand the tribocorrosion wear mechanism, the morphologies of the worn surfaces were investigated using a 3D optical profiler. As demonstrated in Figs.7.4a-b, the wear track for the SLM sample is narrower than for the untreated surface, and there is no retained texture inside. The maximum measured depth of the wear track is 20 μm, also smaller than the untreated surface value (~ 30 μm), thus suggesting less material loss.

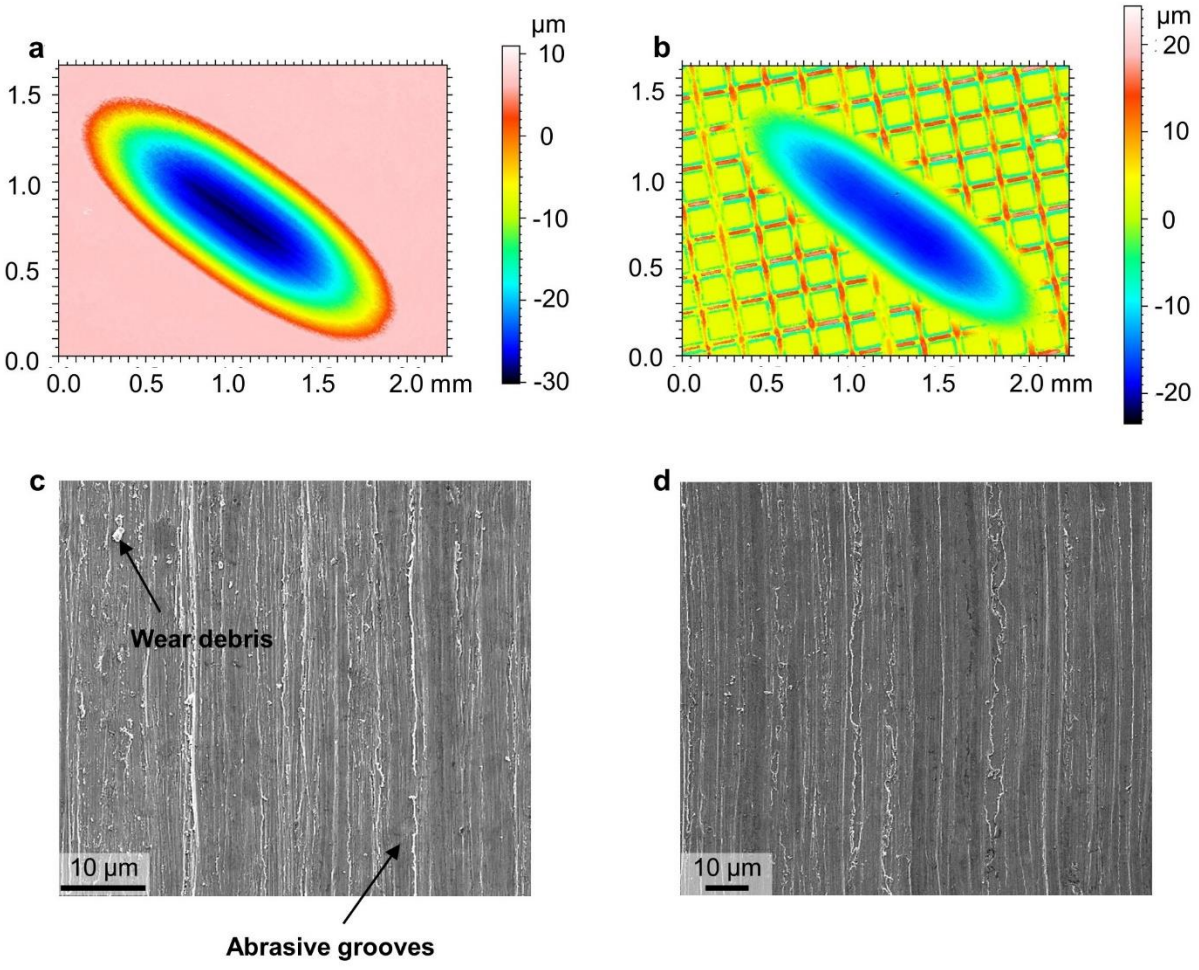

Fig.7. 4. *3D optical profiling images of untreated surface (a) and SLM (b) samples tested at 5 Hz. (c-d) Corresponding SE images of worn surface respectively.*

Fig.7.4c and d show the SE images of the worn surfaces. Pronounced grooves parallel to sliding direction, which is regarded as a key characteristic of two-body abrasive wear, are observed in both samples [111], [245]. Additionally, wear debris with submicron size (as indicated by arrow) can be seen retained on the surface, which provides direct evidence for the activation of the three-body wear mode. Thus, it could be concluded that the predominant wear mechanism of both pairs is combined two- and three-body abrasive wear.

The specific wear rate was obtained by measuring the wear track volume using *MountainsMap*® 8.0, an advanced surface and image analysis for profilers. As illustrated in Fig.7.5, SLM sample displays an evident reduction of ~50 % in specific wear rate ($K = 1.09 \times 10^{-4} \pm 0.28$ mm^3 N^{-1} m^{-1}) in comparison to the untreated surface ($K = 2.35 \times 10^{-4} \pm 0.21$ mm^3 N^{-1} m^{-1}), indicating an enhanced wear resistance.

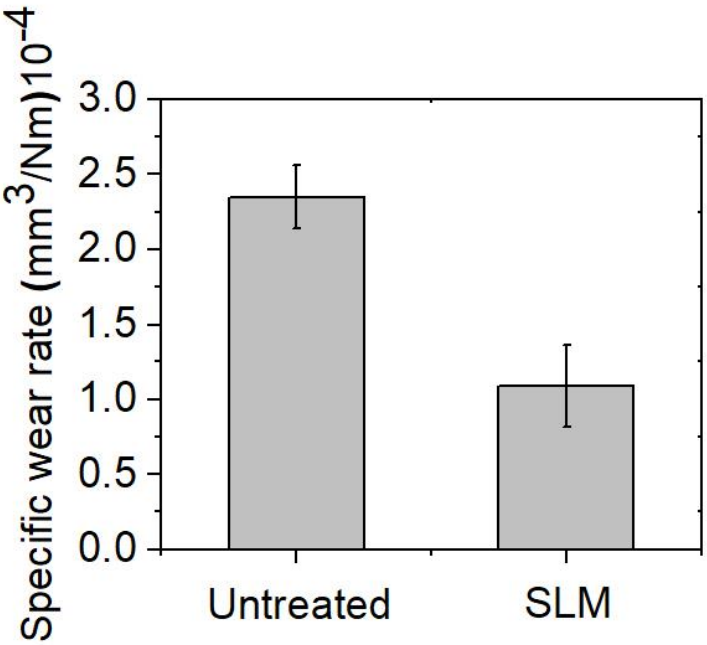

Fig.7. 5. *Comparison of specific wear rate between untreated and SLM surfaces tested at 5 Hz.*

7.2.2.2 Tribocorrosion under OCP conditions at 2.5 Hz sliding frequency

Furthermore, tribocorrosion tests of SLM and untreated samples were carried out under OCP conditions at a sliding frequency of 2.5 Hz. It can be seen that the COF of the untreated surface progressively decreases from 0.35 to 0.25 with intermittent oscillation, Fig.7.6a. In contrast, the curve of SLM seems to be much smoother. The apparent run-in period at the beginning of sliding was observed, corresponding to a sharp increase of the COF from 0.22 to 0.4, then gradually decreased to 0.25, with this value maintained until the end of the test.

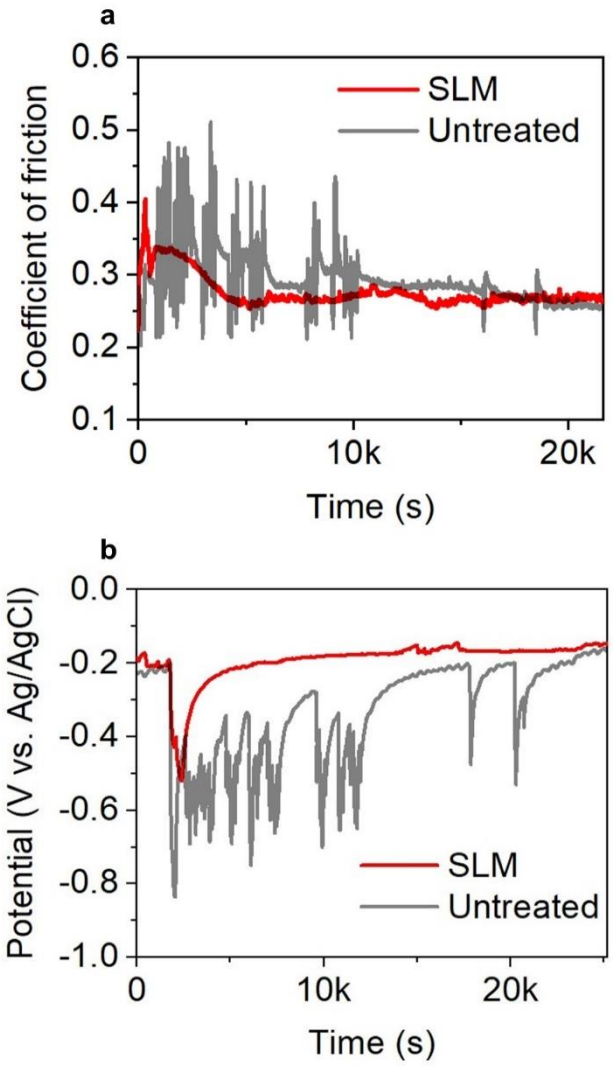

Fig.7. 6. *The evolution of the COF (a) and the OCP (b) during the tribocorrosion test at 2.5 Hz.*

Regarding the potential shown in Fig.7.6b, both curves are found to be consistent with the evolution of their COF. The potential of SLM displayed a steady recovery after the run-in period, implying a better capacity for repassivation. Although the recovery of potential was also observed in the untreated sample, the sudden drop of potential representing partial depassivation still existed, which may accelerate the synergistic effect between mechanical and chemical damage, contributing to the greater material loss in comparison to that of SLM.

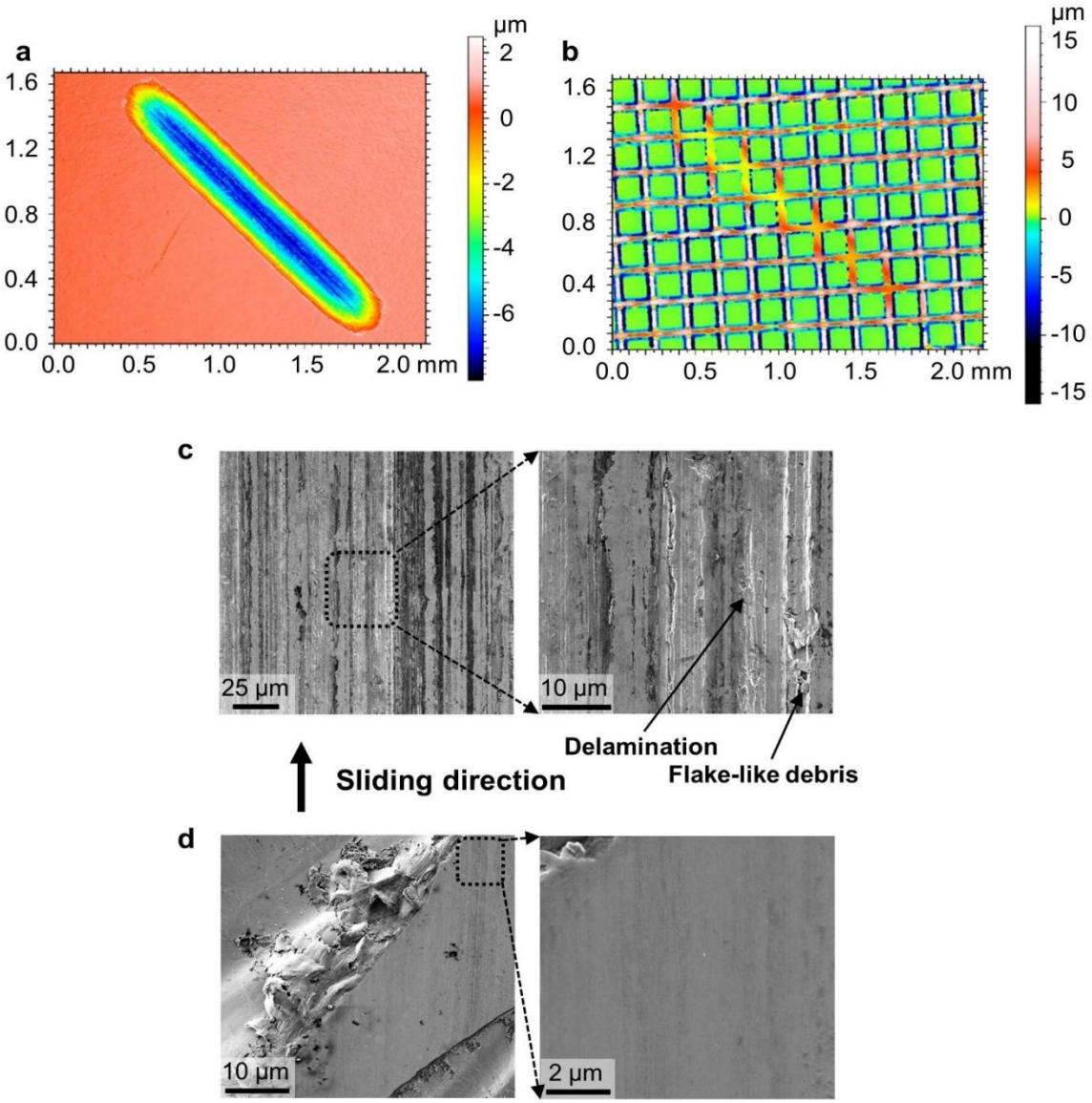

Fig.7. 7. *3D optical profiling images of untreated surface (a) and SLM (b) samples tested at 2.5 Hz. (c-d) Corresponding SE images of worn surface respectively.*

To better understand the wear mechanism of both samples, the worn surface morphologies were examined. The wear track of the untreated surface 2.5 Hz is shown in 3D optical microscopy in Fig.7.7a. SEM of the worn surface, Fig.7.7c, exhibited abrasive wear characteristics, including delamination, ploughing grooves, and flake-like debris (as indicated by arrows), similar to samples tested at 5 Hz. Additionally, a heterogeneous distribution of regions exhibiting dark contrast indicated the formation of tribofilm [185], [186].

Interestingly, the material removal of the SLM sample was within the range of the texture, and no damage was observed on the substrate (Fig.7.7b). Further observation shown in Fig.7.7d confirmed a much smoother worn surface than on the untreated surface. Even at high magnification, the wear surface looked exceptionally smooth, but with the generation of flake-like debris located inside the trench region. Also, close inspection of the ball revealed that there were no visible scratches and retained debris on the ceramic ball run against the SLM surface (Fig.7.8).

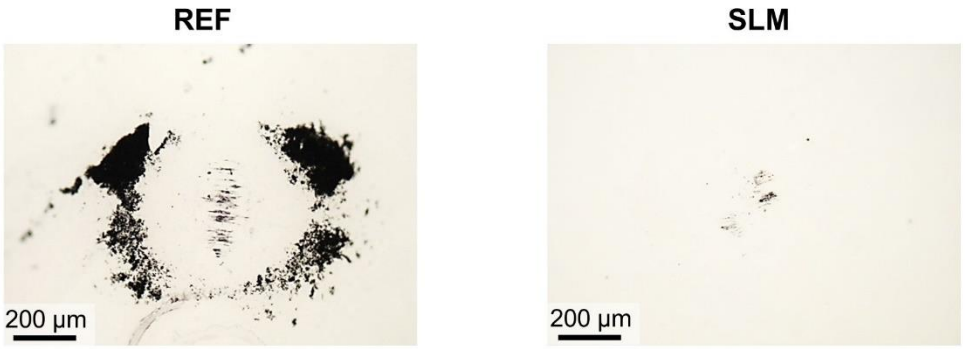

Fig.7. 8. *Optical micrographs obtained from ceramic balls after tribocorrosion at 2.5 Hz.*

Thus, the predominant wear mechanism of the SLM sample tested at 2.5 Hz could be a novel two-body mode, in which riblet texture separated the counterface and substrate by introducing a refined supporting structure and wear debris entrapment in the recesses. This structure therefore suppressed mechanical accelerated degradation and strongly improved tribocorrosion performance. As expected in Fig.7.9, an ultra-low value of $K = 3.39 \times 10^{-8} \pm 0.09$ mm^3 N^{-1} m^{-1} is obtained for the SLM sample, several orders smaller than that of untreated sample ($K = 3.01 \times 10^{-4} \pm 0.54$ mm^3 N^{-1} m^{-1}), which is a significant difference.

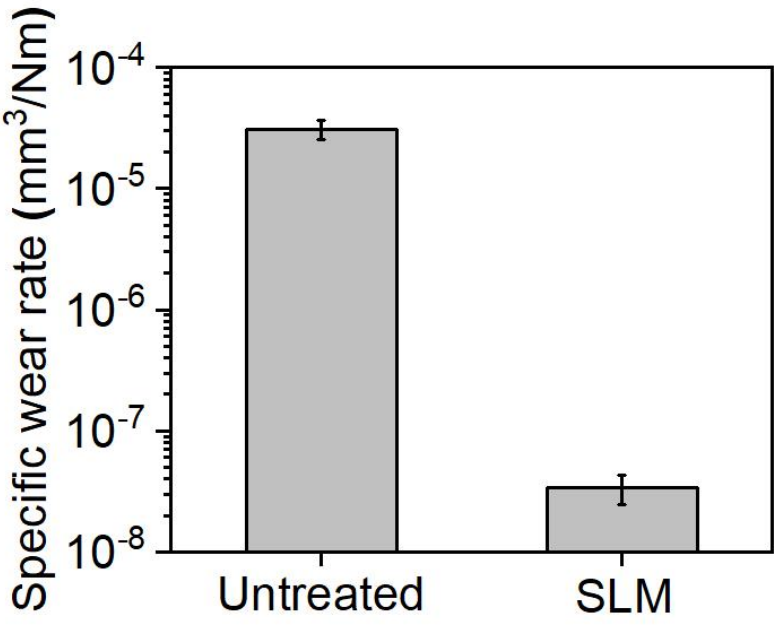

Fig.7. 9. *Comparison of specific wear rate between the untreated surface and SLM tested at 2.5 Hz.*

7.2.2.2.1 The tribofilm formation when testing at 2.5 Hz

FIB samples of the untreated and SLM worn surfaces tested at 2.5 Hz were prepared along the siding direction and cross-sectional TEM micrographs are shown in Fig.7.10. The interface between protective Pt deposition, surface and subsurface was marked by dashed lines. The untreated surface consisted of a two-layer tribofilm, in which the upper part had a thickness of about 40 nm and the bottom part ranged from 20 to 80 nm. For the SLM surface, the tribofilm appeared to be much thinner (~10 nm).

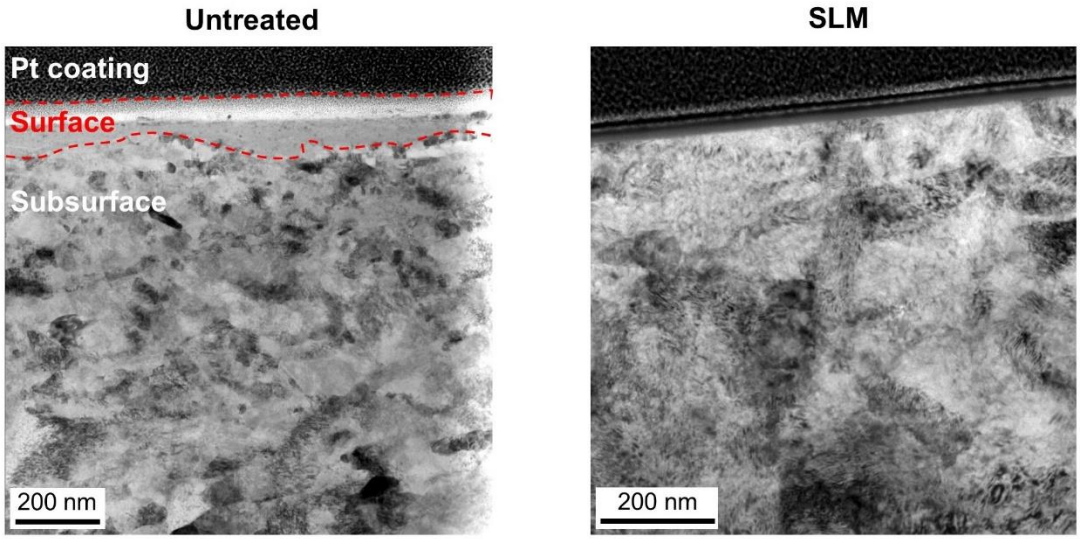

Fig.7. 10. *Comparison of surface structure using BF-TEM micrographs taken from the longitudinal cross-section.*

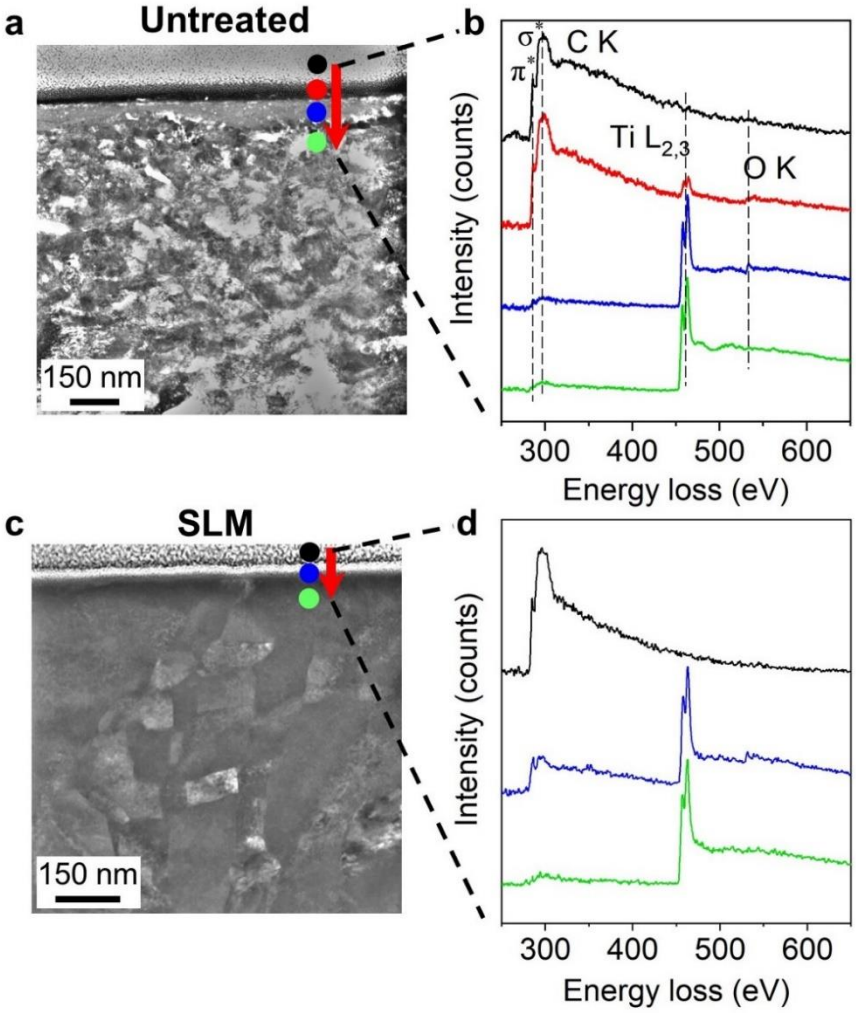

Fig.7. 11. *STEM micrographs taken from longitudinal cross-section showing surface and subsurface microstructure of (a) untreated and (c) SLM samples. (b), (d) Normalised EEL spectra taken along the red arrow.*

To further understand the formation mechanism of the tribofilm, EELS point analysis was carried out from deposition to substrate. As illustrated in Fig.7.11a, normalised EEL spectra of the untreated surface taken from four sites of interest (as indicated by black, red, blue and green circles in corresponding STEM micrograph) are plotted. The upper part of the tribofilm (red label) displays a typical edge consisting of sp^2-bonded π^*, which is often regarded as a key characteristic of graphite-like carbon [201], [202]. Moreover, the presence of Ti-$L_{2,3}$ and O-K

edges were also confirmed, thus indicating a mixture of organic materials and metallic oxides [126], [203]. For the bottom part of the tribofilm (blue label), the intensity of the C-K edge almost disappeared while the Ti-$L_{2,3}$ edge was much stronger, which suggested that this area was predominantly metallic with lower organic content. In the EEL spectra of the substrate, there is no observed O-K edge, as expected. However, the presence of carbon was still detected. This is probably carbon contamination which is common in TEM samples [246], [247]. For the SLM sample, the heterogeneous structure of tribofilm was not observed. Metallic products were found to provide the main contribution to tribofilm (blue curve), with no evidence of oxygen.

7.2.2.2.2 Structural evolution of subsurface

Interestingly, there was a huge difference in subsurface structure between the two surfaces (Fig.7.11): the untreated surface had an ultra-fine nanocrystalline layer, while the worn subsurface of SLM displayed an equiaxed structure. Further TEM orientation analysis, using precession electron diffraction, was carried out of the subsurface. Fig.7.12 shows the evolution of subsurface microstructure after tribocorrosion test. Underneath the untreated worn surface, a nanostructured layer with a thickness of 800 nm was observed, with the size of the nanocrystals increasing with depth below the worn surface. There was an abrupt interface between the nanocrystalline layer and the un-deformed substrate. In the case of the SLM subsurface, there was no observed structural gradient, and the substructure was comparable with the original microstructure, with very little evidence of plastic deformation. Grain size

distribution histograms (Fig.7.12e) revealed that the majority of the grains in the nanostructured layer were below 50 nm in size, and the average diameter was measured to be 31 nm, which was much smaller compared with that of the SLM substructure.

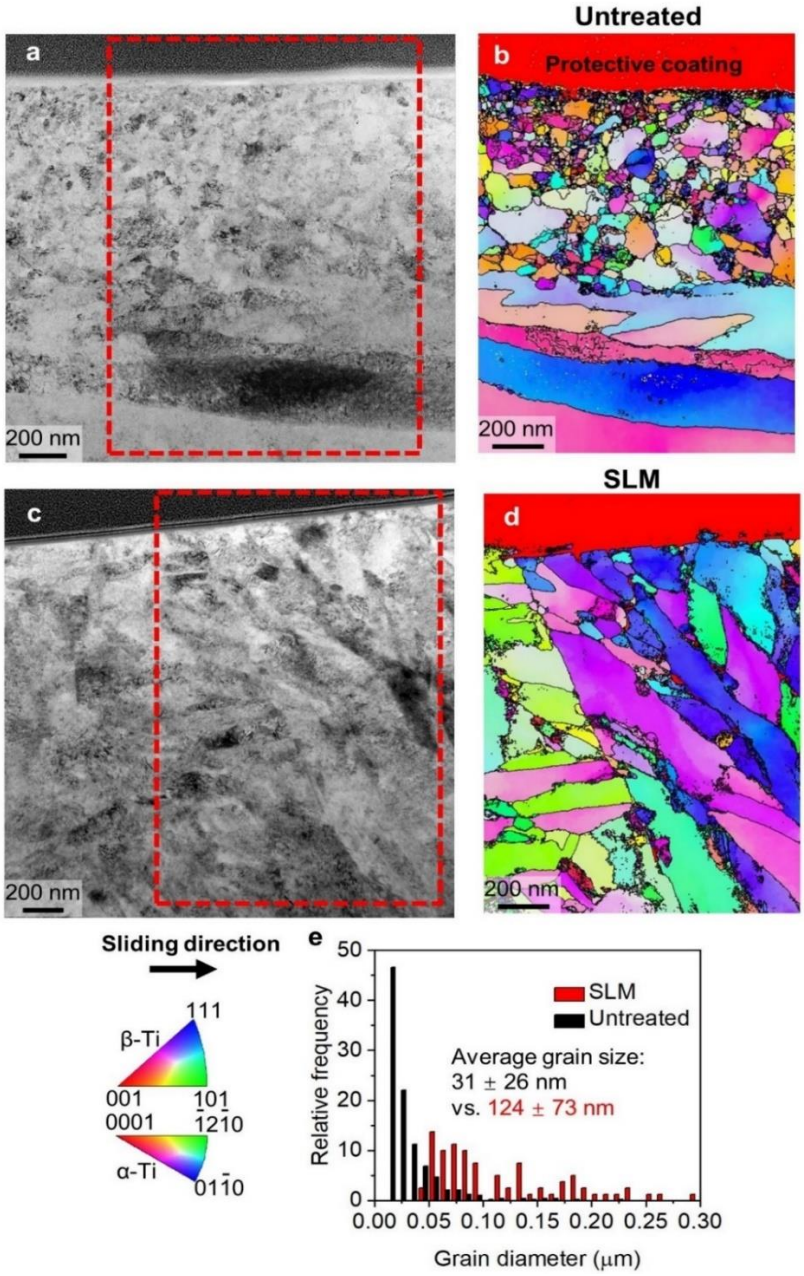

Fig.7. 12. *TEM orientation map taken from cross-sectional worn surface showing the structural evolution subsurface. (a) and (b) BF image and orientation map of the untreated sample (dashed rectangle). (c) and (d) BF image and orientation map of the untreated sample (dashed rectangle).SLM sample. (e) Corresponding statistics of grain size distribution.*

Lastly, an additional phase map (Fig.7.13) was present and suggested that there was no apparent phase segregation in both samples. The subsurface regions that were indexed as amorphous were probably regions where the preparation of the metallic FIB foil resulted in Ga ion damage.

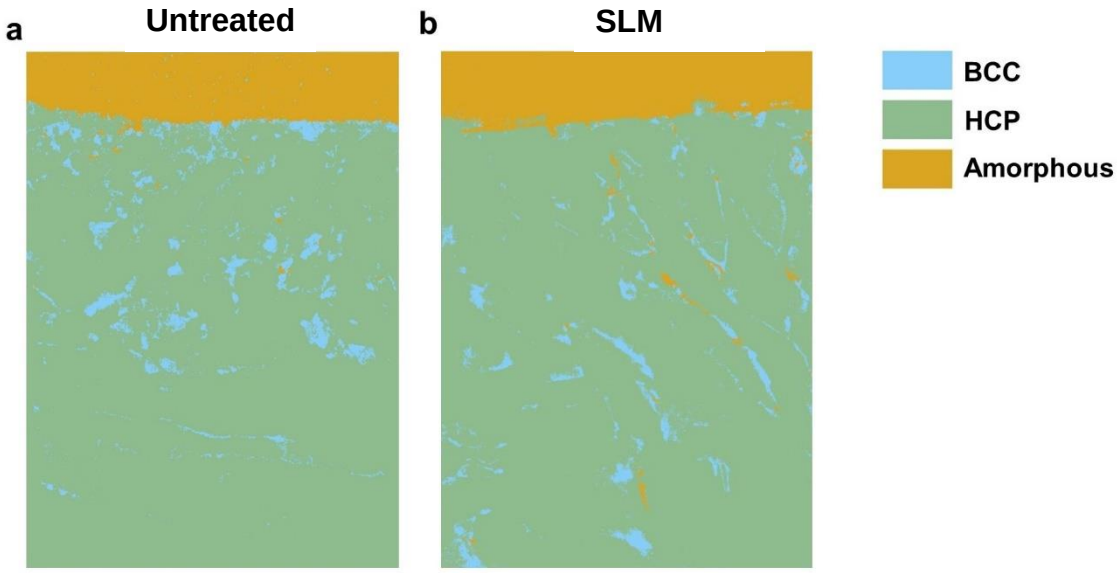

Fig.7. 13. *Phase map showing the α′ and β phase distribution of the worn cross-sectional surface for (a) untreated and (b) SLM samples.*

7.3 Discussion

7.3.1 Effects of texture on electrochemical properties

Both OCP and potentiodynamic polarisation results suggested an improvement of corrosion resistance for SLM samples under static conditions. This can be explained by the reduced area exposed to the medium. Although the specific surface area has increased due to the formation of riblet-like geometry, the texture may prevent the contact between the solution and through

generating “air pockets” inside the trench region, which are widely reported in designing superhydrophobic surfaces [248], [249]. Additionally, nanoscale protrusions provide more grain boundaries compared to the primary structure, implying a more active surface condition. This explains why the I_{corr} of SLM is slightly larger than the untreated surface.

7.3.2 The formation of tribofilm when testing at 2.5 Hz

Generally, the process of tribocorrosion can be summarised as follows: the mechanical movement results in local rupture of the oxide film and substrate, which introduces abrasive wear debris (third body) and generates a galvanic coupling between the worn and unworn surface. This provides a driving force for continuous corrosion during mechanical movement, as well as more severe abrasion, known as “corrosion-accelerated wear” and “wear accelerated corrosion”. For tribocorrosion under the protein-containing circumstances, another factor that needs to be considered is the formation of a tribofilm, which has been assumed as a mechanochemical interaction between denatured protein and metallic products, including oxide and wear material [185], [186], [201]. Previous studies have confirmed that this organic layer could perform as a boundary lubricant which therefore lowers the COF [186], [250]. However, the correlation between tribofilm and wear resistance is still unclear.

From the high-resolution investigation, the formation of a tribofilm was identified for both untreated and SLM samples tested at 2.5 Hz. A heterogeneous structure of the tribofilm was observed for the first time in the untreated sample. The bottom part of tribofilm could be attributed to the delamination of metallic products, with compacted oxide and metallic wear

debris mixing to form a discontinuous tribolayer [10], [251]. The upper part may be regarded as a result of the absorption of denatured protein and metal ions. As previously suggested, the retention of tribofilm would be affected by load condition, applied potential. The real contact geometry and the *in-vivo* biomedical implant environment are much more complicated, which may result in a discontinuous distribution on the implant surface [185], [186], [200], [204].

The tribofilm on the worn SLM surface was more uniform, much thinner and exhibited weaker Z contrast compared to the untreated sample (Fig.7.11c and d). The corresponding EELS results indicated that the tribofilm on the SLM surface was an inorganic layer mainly consisting of metal, although it could be carbon-based but just too thin to obtain a signal unique to the tribofilm.

The difference in worn surface topography between the SLM and untreated samples was striking. The SLM worn surface was remarkably smooth, consistent with the very low wear rates observed. Almost no grooves or other abrasive damage was observed. It should be noted that the contact (attack) angle and pressure between the alumina ball and micro-protrusions for the SLM sample are higher than normal ball-on-disc configuration because of the smaller apparent area of contact, and so contact stresses could not explain the differences. Moreover, given the huge difference in hardness between aluminium and bare surface (1600 vs. 340 HV), the initial stage (i.e., depassivation) is expected to be dominated by microcutting or microploughing [208], [252]. The SEM observation suggested that the wear debris from the SLM surface was derived from delamination, and there was no evidence of microcutting or microploughing, Fig. 7.7d. The removal of the wear debris into the surface recesses prevented

further 3rd body surface damage, thereby protecting the passive film and the substrate and reduced the extent of metallic ion release. This was consistent with the OCP curves, in which SLM samples exhibited a much more stable potential recovery shown in Fig.7.6b.

Another interesting and apparently unique observation is that this smooth worn surface topography was associated with negligible plastic deformation at the worn surface, Fig.7.12b. Classical delamination wear is associated with high Hertzian contact stresses but low surface strain. The classical view is that deformation occurs in a high-contact-stress, low-cycle fatigue (LCF) regime, concentrated below the surface. Cracks initiate at particles and propagate in a manner consistent with the LCF, which then results in the formation of sheet-like debris. However, the current situation is quite different. There was no evidence of any strain at the worn surface, Fig.7.12c and d, with grain and lath boundaries extending up to the worn surface without any distortion. The question then arises as to how delamination sheets are formed with such a microstructure? The answer is not clear, but it could be envisaged that the sheets are sheared from the surface with very localised plastic overload. In any event, it is probable that the delamination events occurred in the early stages of sliding, i.e., during running in, and that the surface examined in Fig.7.12 was a result of subsequent mild wear events, with contact essentially elastic, which is commensurate with a low-contact-stress, high-cycle fatigue (HCF) regime, such that the event leading to delamination was no longer present.

7.3.3 The formation of the nanocrystalline layer

It has been accepted that the imposition of shear during tribological contact can lead to the introduction of extreme strain accumulation and generates a refined nanocrystalline layer underneath the topmost surface [90], [253]. Moreover, tribofilm formation is found to play a key role in suppressing dislocation annihilation leading to severe deformation of the subsurface [200]. Although it is believed that the refined microstructure can improve the wear resistance due to the enhanced hardness, it should be noted the generation of wear debris, as well as hard asperity of counterface, will still destroy surface films and constantly consume bare metals. Especially for metallic implant, these hard metallic particles can introduce irreversible damage to soft tissue leads to implant failure [4], [80]. Thus, it is remarkable that the SLM subsurface still displays a stable microstructure even after 54000 sliding cycles at 2.5 Hz, and a superior capability of plastic accommodation is also confirmed.

7.4 Summary

In summary, the electrochemical properties and tribocorrosion behaviour of untreated and SLM samples were examined. It can be reasonably concluded that laser texturing breaks the vicious cycle of metallic abrasion by cutting off the supply of abrasive debris and plays a significant role in keeping passivating state through transfer aggressive three-body abrasion to mild, two-body oxidative wear, thus promoting the effects of protective layers, i.e., tribofilm layers on SLM surface. The ultra-low wear rate $K = 3.39 \times 10^{-8} \pm 0.09$ mm^3 N^{-1} m^{-1} was obtained, suggesting a great potential for orthopaedic applications.

Chapter 8 Conclusions and Future Work

8.1 Conclusions

The development of metallic materials for biomedical applications is not as simple as designing an alloy with enhanced mechanical performance. Still, the conditions under which tribological contact occurs *in-vivo* should be taken into account as far as possible. This project attempted to present a framework providing good guidance for the development of biomedical Ti alloys. A series of in-house Ti-Mo-Fe-Sn alloys were designed mainly based on *d-electron* theory and average valence electron concentration. A fundamental understanding of their mechanical properties and tribocorrosion performance has been identified and discussed. The link between worn surface and wear mechanism has been evaluated and discussed as well. The main findings are summarised below:

Mechanical deformation of new alloys

- The increasing addition of Mo and Sn both had a significant effect on the deformation mechanism of Ti413, Ti513 and Ti514. Deformation mode firstly changed from stress-induced martensite consisting of internal {332}<113> twinning and type I martensite twinning (TWIP +TRIP) to multiple {332}<113> and {112}<111> twinning (TWIP) as the addition of Mo increased. Single dislocation slip was confirmed in Ti514, indicating that neutral Sn could also perform as a β stabiliser.
- Deformation bands formed of stress-induced martensite and {332}<113> twins were observed in Ti-4Mo-Fe-3Sn and Ti-5Mo-Fe-3Sn alloys with an increase of strain,

which contributed to the stabilisation of strain hardening rate and was responsible for the enhanced plasticity. Moreover, TWIP + TRIP in Ti-4Mo-Fe-3Sn alloy was found to result in a stronger strain hardening effect than single twinning in Ti-5Mo-Fe-3Sn alloy because the introduction of complex twinning and new phase boundaries formed a strong obstacle to the path of dislocation slip.

- The main deformation mode in Ti513 and Ti514 was not consistent with the *d*-electron prediction, implying the discrepancy in $\overline{Bo} - \overline{Md}$ diagram, which needs further experimental investigation to optimise it.
- The enhanced ductility in the Ti-5Mo-Fe-4Sn alloy was mainly attributed to the dislocation multiplication. It resulted in low dislocation mobility but negligible strain hardening.

Electrochemical behaviour

- Measurements of E_{ocp}, E_{corr} and low I_{corr} found that the Ti-5Mo-Fe-3Sn alloy had the best corrosion resistance of the Ti413, Ti513 and Ti64ELI alloys investigated. Additionally, the difference between E_{ocp} and the E_{corr} also indicated that the presence of proteins could weaken interfacial electrochemical reactions and it behaved as a corrosion inhibitor.

Tribocorrosion

- The tribocorrosion wear mechanisms in all alloys were identified as a combination of three-body and two-body (ploughing) abrasive wear when tested at 5 Hz. The Ti-5Mo-Fe-3Sn exhibited better wear resistance compared to Ti-4Mo-Fe-3Sn and Ti-6Al-4V

ELI. This in house developed alloy is the first beta titanium alloy to exhibit better wear resistance than Ti-6Al-4V.

- The evolution of the OCP well described the competition between depassivation and repassivation during tribocorrosion. Decreasing the sliding speed was found to result in unstable potential recovery in both Ti-4Mo-Fe-3Sn and Ti-6Al-4V ELL. This potential recovery was associated with the more extensive formation of a tribofilm in protein-containing solutions. The tribofilm appeared to entrap wear debris and performed as a solid lubricant film, stabilising the COF.
- The specific wear rates were lower at 2.5 Hz (10 mm/s) compared to 5 Hz (20 mm/s) for all tested materials (Ti-5Mo-Fe-3Sn, Ti-4Mo-Fe-3Sn and Ti-6Al-4V ELI). This was associated with the greater formation of a tribofilm at 2.5 compared to 5 Hz.
- The sliding speed had a measurable effect on the formation of a nanocrystalline layer for the Ti-6Al-4V ELI, with a lower sliding speed associated with a more pronounced nanocrystalline layer beneath the worn surface. Thus, the larger nanocrystalline layer was associated with a more widespread tribolayer and a lower specific wear rate. The lower wear rate led to a narrower wear track and thereby higher contact stresses which were believed to promote the thicker nanocrystalline layer.
- The generation of hard wear debris acted as a 3rd body abrasive resulting ploughing and thereby the destruction of the passive state. Thus, it would be interesting to reduce the abrasion from the third body, i.e., wear particles and develop a stable repassivation in titanium alloys in the future.

Effect of surface texturing on wear

In order to develop a strategy for retaining the passive state during wear, recent cutting-edge selective laser melting technology was successfully used to realise a novel surface texture on Ti-6Al-4V ELL. The corresponding topography, mechanical and tribocorrosion performance were examined and discussed. The main findings are summarised below:

- Selective laser melting (SLM) with a low volumetric energy density was applied to Ti64 ELI and led to the successive formation of micro-protrusions and recesses. A superior surface finish was obtained without visible defects such as balling and voiding.
- The rapid cooling kinetics inside of micro-protrusions introduced an ultra-refined martensitic structure with a higher H/E compared to the untreated surface that may help to improve wear resistance.
- *In-situ* micropillar compression testing suggested that the martensitic structure displayed a significant improvement in yield strength. This was mainly attributed to a high-number density of nanograin boundaries, which contributed to a combined dislocation and grain boundary-mediated deformation mechanism.
- The SLM sample exhibited better corrosion resistance compared to the untreated sample, thanks to the hydrophobic effect from recesses, which may reduce the actual contact area.
- The SLM sample exhibited lower material loss under both tribocorrosion test conditions. At 2.5 Hz (10 mm/s), an ultralow specific wear rate of $3.39 \times 10^{-8} \pm 0.09$

$mm^3\ N^{-1}\ m^{-1}$ was obtained, which is far superior to the wear rates normally observed in titanium alloys.

- The SLM texture played a significant role in maintaining a passive state when testing at 2.5 Hz (10 mm/s). The generation of delaminated wear debris during the running-in stage was removed from the contacting surface and stored inside recesses, thereby protecting the surface from abrasive damage and allowing the passive state to be retained.

8.2 Future work

Considering the limitation of this work, some recommendations are proposed for future work.

- It should be noted that the current pin-on-disk apparatus just provides a fundamental understanding of tribocorrosion behaviour. It is necessary to investigate the tribocorrosion behaviour further using an artificial joint simulator, which is closer to the in-vivo condition.
- The degradation of protein becomes the main issue limiting the long-term test in most of the current research. A circulating pump can establish the process of metabolism and realise tribocorrosion more than a million circles, providing high reliability of experiment data.
- Composition analysis of the PBS solution after tribocorrosion should be investigated.

- Surface modification via SLM could be applied in a wider range of ways as riblet-like geometry is just a milestone of this field. A systematic investigation of the various topographies would be valuable and should be undertaken in the future.
- Similarly, the surface texture should be applied to the beta titanium alloys to explore if the wear rate of these alloys could be improved in a similar manner.
- In terms of tribocorrosion behaviour, tests at cathodic and anodic potential should be carried out to investigate more about the synergistic effects between corrosion and wear. The absorption of protein on the surface will be taken into consideration using electrochemical impedance spectroscopy (EIS) as well.

References

[1] J. A. Singh, S. Yu, L. Chen, and J. D. Cleveland, “Rates of total joint replacement in the United States: Future projections to 2020-2040 using the national inpatient sample,” *J. Rheumatol.*, vol. 46, no. 9, pp. 1134–1140, 2019, doi: 10.3899/jrheum.170990.

[2] M. Geetha, A. K. Singh, R. Asokamani, and A. K. Gogia, “Ti based biomaterials, the ultimate choice for orthopaedic implants - A review,” *Progress in Materials Science*, vol. 54, no. 3. pp. 397–425, 2009, doi: 10.1016/j.pmatsci.2008.06.004.

[3] G. S. Matharu, H. G. Pandit, D. W. Murray, and A. Judge, “Adverse reactions to metal debris occur with all types of hip replacement not just metal-on-metal hips: a retrospective observational study of 3340 revisions for adverse reactions to metal debris from the National Joint Registry for England, Wales, Northe,” *BMC Musculoskelet. Disord.*, vol. 17, no. 1, pp. 1–12, 2016, doi: 10.1186/s12891-016-1329-8.

[4] A. Di Laura *et al.*, “The Chemical Form of Metal Species Released from Corroded Taper Junctions of Hip Implants: Synchrotron Analysis of Patient Tissue,” *Sci. Rep.*, vol. 7, no. 1, pp. 1–13, 2017, doi: 10.1038/s41598-017-11225-w.

[5] C. Kenney, S. Dick, J. Lea, J. Liu, and N. A. Ebraheim, “A systematic review of the causes of failure of Revision Total Hip Arthroplasty,” *J. Orthop.*, vol. 16, no. 5, pp. 393–395, 2019, doi: 10.1016/j.jor.2019.04.011.

[6] T. Saito, “Multifunctional Alloys Obtained via a Dislocation-Free Plastic Deformation Mechanism,” *Science (80-.).*, vol. 300, no. 5618, pp. 464–467, 2003, doi: 10.1126/science.1081957.

[7] S. Guo, Q. Meng, X. Zhao, Q. Wei, and H. Xu, “Design and fabrication of a metastable β-type titanium alloy with ultralow elastic modulus and high strength,” *Sci. Rep.*, vol. 5, no. December 2014, pp. 1–8, 2015, doi: 10.1038/srep14688.

[8] X. Yang and C. R. Hutchinson, “Corrosion-wear of β-Ti alloy TMZF (Ti-12Mo-6Zr-2Fe) in simulated body fluid,” *Acta Biomater.*, vol. 42, pp. 429–439, 2016, doi: 10.1016/j.actbio.2016.07.008.

[9] K. G. Budinski, “Tribological properties of titanium alloys,” *Wear*, vol. 151, no. 2, pp. 203–217, 1991, doi: 10.1016/0043-1648(91)90249-T.

[10] A. Molinari, G. Straffelini, B. Tesi, and T. Bacci, “Dry sliding wear mechanisms of the Ti6A14V alloy,” *Wear*, vol. 208, no. 1–2, pp. 105–112, 1997, doi: 10.1016/S0043-1648(96)07454-6.

[11] G. Lütjering and J. C. Williams, *Titanium*. Springer Science & Business Media, 2007.

[12] E. Pereloma and D. V Edmonds, *Phase transformations in steels: Diffusionless transformations, high strength steels, modelling and advanced analytical techniques*. Elsevier, 2012.

[13] G. and J. W. Lütjering, *Titanium (Engineering Materials and Processes)*. Berlin Heidelberg: Springer, 2007.

[14] Y. Zheng, R. E. A. Williams, S. Nag, R. Banerjee, H. L. Fraser, and D. Banerjee, “The effect of alloy composition on instabilities in the β phase of titanium alloys,” *Scr. Mater.*, vol. 116, pp. 49–52, 2016, doi: 10.1016/j.scriptamat.2016.01.024.

[15] W. F. Ho, C. P. Ju, and J. H. Chern Lin, “Structure and properties of cast binary Ti-Mo alloys,” *Biomaterials*, vol. 20, no. 22, pp. 2115–2122, 1999, doi: 10.1016/S0142-9612(99)00114-3.

[16] Y. L. Zhou and D. M. Luo, “Microstructures and mechanical properties of Ti-Mo alloys cold-rolled and heat treated,” *Mater. Charact.*, vol. 62, no. 10, pp. 931–937, 2011, doi: 10.1016/j.matchar.2011.07.010.

[17] M. J. Lai, C. C. Tasan, and D. Raabe, “On the mechanism of {332} twinning in metastable β titanium alloys,” *Acta Mater.*, vol. 111, pp. 173–186, 2016, doi: 10.1016/j.actamat.2016.03.040.

[18] X. Ji, S. Emura, T. Liu, K. Suzuta, X. Min, and K. Tsuchiya, “Effect of oxygen addition on microstructures and mechanical properties of Ti-7.5Mo alloy,” *J. Alloys Compd.*, vol. 737, pp. 221–229, 2018, doi: 10.1016/j.jallcom.2017.12.072.

[19] Z. Tarzimoghadam, S. Sandlöbes, K. G. Pradeep, and D. Raabe, “Microstructure design and mechanical properties in a near-α Ti-4Mo alloy,” *Acta Mater.*, vol. 97, pp. 291–304, 2015, doi: 10.1016/j.actamat.2015.06.043.

[20] F. Sun *et al.*, “Investigation of early stage deformation mechanisms in a metastable ?? titanium alloy showing combined twinning-induced plasticity and transformation-induced plasticity effects,” *Acta Mater.*, vol. 61, no. 17, pp. 6406–6417, 2013, doi: 10.1016/j.actamat.2013.07.019.

[21] S. K. Sikka, Y. K. Vohra, and R. Chidambaram, *Omega phase in materials*, vol. 27, no. 3–4. 1982.

[22] D. Choudhuri *et al.*, “Coupled experimental and computational investigation of omega phase evolution in a high misfit titanium-vanadium alloy,” *Acta Mater.*, vol. 130, pp. 215–228, 2017, doi: 10.1016/j.actamat.2017.03.047.

[23] J. Gao, A. J. Knowles, D. Guan, and W. M. Rainforth, “ω phase strengthened 1.2GPa metastable β titanium alloy with high ductility,” *Scr. Mater.*, vol. 162, pp. 77–81, 2019, doi: 10.1016/j.scriptamat.2018.10.043.

[24] C. Lin, G. Yin, A. Zhang, Y. Zhao, and Q. Li, “Simple models to account for the formation and decomposition of athermal ω phase in titanium alloys,” *Scr. Mater.*, vol. 117, pp. 28–31, 2016, doi: 10.1016/j.scriptamat.2016.01.042.

[25] H. Liu, M. Niinomi, M. Nakai, and K. Cho, “Athermal and deformation-induced w-phase transformations in biomedical beta-type alloy Ti-9Cr-0.2O,” *Acta Mater.*, vol. 106, pp. 162–170, 2016, doi: 10.1016/j.actamat.2016.01.008.

[26] T. Li *et al.*, “New insights into the phase transformations to isothermal ω and ω-assisted α in near β-Ti alloys,” *Acta Mater.*, vol. 106, pp. 353–366, 2016, doi: 10.1016/j.actamat.2015.12.046.

[27] W. Wang, X. Zhang, W. Mei, and J. Sun, “Role of omega phase evolution in plastic deformation of twinning-induced plasticity β Ti–12V–2Fe–1Al alloy,” *Mater. Des.*, vol. 186, p. 108282, 2020, doi: 10.1016/j.matdes.2019.108282.

[28] M. Abdel-Hady, K. Hinoshita, and M. Morinaga, “General approach to phase stability and elastic properties of β-type Ti-alloys using electronic parameters,” *Scr. Mater.*, vol. 55, no. 5, pp. 477–480, 2006, doi: 10.1016/j.scriptamat.2006.04.022.

[29] Y. Al-Zain, Y. Sato, H. Y. Kim, H. Hosoda, T. H. Nam, and S. Miyazaki, “Room temperature aging behavior of Ti-Nb-Mo-based superelastic alloys,” *Acta Mater.*, vol. 60, no. 5, pp. 2437–2447, 2012, doi: 10.1016/j.actamat.2011.12.033.

[30] S. J. Li, T. C. Cui, Y. L. Hao, and R. Yang, “Fatigue properties of a metastable β-type titanium alloy with reversible phase transformation,” *Acta Biomater.*, vol. 4, no. 2, pp. 305–317, 2008, doi: 10.1016/j.actbio.2007.09.009.

[31] Y. L. Hao, S. J. Li, S. Y. Sun, C. Y. Zheng, and R. Yang, “Elastic deformation behaviour of Ti-24Nb-4Zr-7.9Sn for biomedical applications,” *Acta Biomater.*, vol. 3, no. 2, pp. 277–286, 2007, doi: 10.1016/j.actbio.2006.11.002.

[32] D. Kuroda, M. Niinomi, M. Morinaga, Y. Kato, and T. Yashiro, “Design and mechanical properties of new β type titanium alloys for implant materials,” *Mater. Sci. Eng. A*, vol. 243, no. 1–2, pp. 244–249, 1998, doi: 10.1016/s0921-5093(97)00808-3.

[33] K. Hagihara and T. Nakano, “Experimental clarification of the cyclic deformation mechanisms of β-type Ti-Nb-Ta-Zr-alloy single crystals developed for the single-crystalline implant,” *Int. J. Plast.*, vol. 98, pp. 27–44, 2017, doi: 10.1016/j.ijplas.2017.06.006.

[34] P. Li, X. Ma, T. Tong, and Y. Wang, “Microstructural and mechanical properties of β-type Ti–Mo–Nb biomedical alloys with low elastic modulus,” *J. Alloys Compd.*, vol. 815, p. 152412, 2020, doi: 10.1016/j.jallcom.2019.152412.

[35] S. Guo *et al.*, “Design and fabrication of a (β+α″) dual-phase Ti-Nb-Sn alloy with linear deformation behavior for biomedical applications,” *J. Alloys Compd.*, vol. 805, pp. 517–521, 2019, doi: 10.1016/j.jallcom.2019.07.109.

[36] K. Endoh, M. Tahara, T. Inamura, and H. Hosoda, “Effect of Sn and Zr addition on the martensitic transformation behavior of Ti-Mo shape memory alloys,” *J. Alloys Compd.*, vol. 695, pp. 76–82, 2017, doi: 10.1016/j.jallcom.2016.10.108.

[37] Y. L. Hao, S. J. Li, S. Y. Sun, and R. Yang, “Effect of Zr and Sn on Young’s modulus and superelasticity of Ti-Nb-based alloys,” *Mater. Sci. Eng. A*, vol. 441, no. 1–2, pp. 112–118, 2006, doi: 10.1016/j.msea.2006.09.051.

[38] B. Jiang *et al.*, “Effects of Nb and Zr on structural stabilities of Ti-Mo-Sn-based alloys with low modulus,” *Mater. Sci. Eng. A*, vol. 687, no. January, pp. 1–7, 2017, doi: 10.1016/j.msea.2017.01.047.

[39] M. Abdel-Hady, K. Hinoshita, and M. Morinaga, “General approach to phase stability and elastic properties of β-type Ti-alloys using electronic parameters,” *Scr. Mater.*, vol. 55, no. 5, pp. 477–480, 2006, doi: 10.1016/j.scriptamat.2006.04.022.

[40] H. Ikehata, N. Nagasako, T. Furuta, A. Fukumoto, K. Miwa, and T. Saito, “First-principles calculations for development of low elastic modulus Ti alloys,” *Phys. Rev. B - Condens. Matter Mater. Phys.*, vol. 70, no. 17, pp. 1–8, 2004, doi: 10.1103/PhysRevB.70.174113.

[41] Q. Wang, C. Dong, and P. K. Liaw, “Structural Stabilities of β-Ti Alloys Studied Using a New Mo Equivalent Derived from [β/(α + β)] Phase-Boundary Slopes,” *Metall. Mater. Trans. A*, vol. 46, no. 8, pp. 3440–3447, 2015, doi: 10.1007/s11661-015-2923-3.

[42] E. Eisenbarth, D. Velten, M. Müller, R. Thull, and J. Breme, “Biocompatibility of β-stabilizing elements of titanium alloys,” *Biomaterials*, vol. 25, no. 26, pp. 5705–5713, 2004, doi: 10.1016/j.biomaterials.2004.01.021.

[43] S. Cai, L. Wang, J. E. Schaffer, J. Gao, and Y. Ren, “Influence of Sn on martensitic beta Ti alloys,” *Mater. Sci. Eng. A*, vol. 743, no. September 2018, pp. 764–772, 2019, doi: 10.1016/j.msea.2018.11.095.

[44] M. F. Ijaz, H. Y. Kim, H. Hosoda, and S. Miyazaki, “Effect of Sn addition on stress hysteresis and superelastic properties of a Ti-15Nb-3Mo alloy,” *Scr. Mater.*, vol. 72–73, pp. 29–32, 2014, doi: 10.1016/j.scriptamat.2013.10.007.

[45] M. R. Dal Bó *et al.*, “The effect of Zr and Sn additions on the microstructure of Ti-Nb-Fe gum metals with high elastic admissible strain,” *Mater. Des.*, 2018, doi: 10.1016/j.matdes.2018.10.040.

[46] “<www.accessdata.fda.gov/scripts/cdrh/cfdocs/cfres/res.cfm?id=99392>, August 24, 2011).” .

[47] S. K. Fokter, A. Molicnik, R. Kavalar, P. Pelicon, R. Rudolf, and N. Gubeljak, “Why do some titanium-alloy total hip arthroplasty modular necks fail?,” *J. Mech. Behav. Biomed. Mater.*, vol. 69, pp. 107–114, 2017, doi: 10.1016/j.jmbbm.2016.12.012.

[48] S. Ozan, J. Lin, Y. Li, R. Ipek, and C. Wen, “Development of Ti-Nb-Zr alloys with high elastic admissible strain for temporary orthopedic devices,” *Acta Biomater.*, vol. 20, pp. 176–187, 2015, doi: 10.1016/j.actbio.2015.03.023.

[49] A. Nocivin, I. Cinca, D. Raducanu, V. D. Cojocaru, and I. A. Popovici, “Mechanical properties of a Gum-type Ti–Nb–Zr–Fe–O alloy,” *Int. J. Miner. Metall. Mater.*, vol. 24, no. 8, pp. 909–917, 2017, doi: 10.1007/s12613-017-1477-3.

[50] M. Niinomi, “Mechanical properties of biomedical titanium alloys,” *Mater. Sci. Eng. A*, 2002, doi: 10.1016/s0921-5093(97)00806-x.

[51] A. Biesiekierski, J. Lin, Y. Li, D. Ping, Y. Yamabe-Mitarai, and C. Wen, “Investigations into Ti-(Nb,Ta)-Fe alloys for biomedical applications,” *Acta Biomater.*, vol. 32, pp. 336–347, 2016, doi: 10.1016/j.actbio.2015.12.010.

[52] T. Saito *et al.*, “Multifunctional Alloys Obtained via a Dislocation-Free Plastic Deformation Mechanism,” *Science (80-.).*, vol. 300, no. 5618, pp. 464 LP – 467, Apr. 2003, doi: 10.1126/science.1081957.

[53] X. Min *et al.*, “Effect of oxygen content on deformation mode and corrosion behavior in β-type Ti-Mo alloy,” *Mater. Sci. Eng. A*, vol. 684, no. 2, pp. 534–541, 2017, doi: 10.1016/j.msea.2016.12.062.

[54] Y. Abdelrhman, M. A. H. Gepreel, S. Kobayashi, S. Okano, and T. Okamoto, “Biocompatibility of new low-cost (α + β)-type Ti-Mo-Fe alloys for long-term implantation,” *Mater. Sci. Eng. C*, vol. 99, no. January, pp. 552–562, 2019, doi: 10.1016/j.msec.2019.01.133.

[55] Y. L. Zhou and M. Niinomi, “Ti-25Ta alloy with the best mechanical compatibility in Ti-Ta alloys for biomedical applications,” *Mater. Sci. Eng. C*, vol. 29, no. 3, pp. 1061–1065, 2009, doi: 10.1016/j.msec.2008.09.012.

[56] Y. L. Zhou and M. Niinomi, “Microstructures and mechanical properties of Ti-50 mass% Ta alloy for biomedical applications,” *J. Alloys Compd.*, vol. 466, no. 1–2, pp. 535–542, 2008, doi: 10.1016/j.jallcom.2007.11.090.

[57] E. Bertrand *et al.*, “Synthesis and characterisation of a new superelastic Ti-25Ta-25Nb biomedical alloy,” *J. Mech. Behav. Biomed. Mater.*, vol. 3, no. 8, pp. 559–564, 2010, doi: 10.1016/j.jmbbm.2010.06.007.

[58] P. F. Santos *et al.*, “Microstructures, mechanical properties and cytotoxicity of low cost beta Ti-Mn alloys for biomedical applications,” *Acta Biomater.*, vol. 26, pp. 366–376, 2015, doi: 10.1016/j.actbio.2015.08.015.

[59] P. Fernandes Santos *et al.*, “Improvement of microstructure, mechanical and corrosion properties of biomedical Ti-Mn alloys by Mo addition,” *Mater. Des.*, vol. 110, pp. 414–424, 2016, doi: 10.1016/j.matdes.2016.07.115.

[60] C. H. Wang *et al.*, “Martensitic microstructures and mechanical properties of as-quenched metastable β-type Ti-Mo alloys,” *J. Mater. Sci.*, vol. 51, pp. 1–11, 2016, doi: 10.1007/s10853-016-9976-6.

[61] S. E. Haghighi, H. B. Lu, G. Y. Jian, G. H. Cao, D. Habibi, and L. C. Zhang, “Effect of α″ martensite on the microstructure and mechanical properties of beta-type Ti-Fe-Ta alloys,” *Mater. Des.*, vol. 76, pp. 47–54, 2015, doi: 10.1016/j.matdes.2015.03.028.

[62] H. Y. Tingting Yao, Kui Du*, Haoliang Wang, Zhiye Huang, Cuihong Li, Linlin Li, Yulin Hao, Rui Yang, "In situ scanning and transmission electron microscopy investigation on plastic deformation in a metastable β titanium alloy," *Acta Mater.*, vol. 133, pp. 21–29, 2017, doi: 10.1016/j.eatbeh.2007.03.005.

[63] H. L. Wang *et al.*, "Tracing the coupled atomic shear and shuffle for a cubic to a hexagonal crystal transition," *Scr. Mater.*, vol. 133, pp. 70–74, 2017, doi: 10.1016/j.scriptamat.2017.02.024.

[64] H. Tobe, H. Y. Kim, T. Inamura, H. Hosoda, and S. Miyazaki, "Origin of {3 3 2} twinning in metastable β-Ti alloys," *Acta Mater.*, vol. 64, pp. 345–355, 2014, doi: 10.1016/j.actamat.2013.10.048.

[65] T. J. Rupert, D. S. Gianola, Y. Gan, and K. J. Hemker, "Experimental observations of stress-driven grain boundary migration," *Science (80-.).*, vol. 326, no. 5960, pp. 1686–1690, 2009.

[66] M. Marteleur, F. Sun, T. Gloriant, P. Vermaut, P. J. Jacques, and F. Prima, "On the design of new β-metastable titanium alloys with improved work hardening rate thanks to simultaneous TRIP and TWIP effects," *Scr. Mater.*, vol. 66, no. 10, pp. 749–752, 2012, doi: 10.1016/j.scriptamat.2012.01.049.

[67] G.-H. Zhao, X. Xu, D. Dye, and P. E. J. Rivera-Díaz-del-Castillo, "Microstructural evolution and strain-hardening in TWIP Ti alloys," *Acta Mater.*, Nov. 2019, doi: 10.1016/J.ACTAMAT.2019.11.009.

[68] J. Gao *et al.*, "Deformation mechanisms in a metastable beta titanium twinning induced plasticity alloy with high yield strength and high strain hardening rate," *Acta Mater.*, vol. 152, pp. 301–314, 2018, doi: 10.1016/j.actamat.2018.04.035.

[69] F. Sun *et al.*, "Strengthening strategy for a ductile metastable β-titanium alloy using low-temperature aging," *Mater. Res. Lett.*, vol. 5, no. 8, pp. 547–553, 2017, doi: 10.1080/21663831.2017.1350211.

[70] J. Zhang *et al.*, “Strong and ductile beta Ti–18Zr–13Mo alloy with multimodal twinning,” *Mater. Res. Lett.*, vol. 7, no. 6, pp. 251–257, 2019, doi: 10.1080/21663831.2019.1595763.

[71] F. Sun *et al.*, “Investigation of early stage deformation mechanisms in a metastable β titanium alloy showing combined twinning-induced plasticity and transformation-induced plasticity effects,” *Acta Mater.*, vol. 61, no. 17, pp. 6406–6417, 2013, doi: 10.1016/j.actamat.2013.07.019.

[72] M. Marteleur, F. Sun, T. Gloriant, P. Vermaut, P. J. Jacques, and F. Prima, “On the design of new β-metastable titanium alloys with improved work hardening rate thanks to simultaneous TRIP and TWIP effects,” *Scr. Mater.*, vol. 66, no. 10, pp. 749–752, 2012, doi: 10.1016/j.scriptamat.2012.01.049.

[73] X. Min, X. Chen, S. Emura, and K. Tsuchiya, “Mechanism of twinning-induced plasticity in β-type Ti-15Mo alloy,” *Scr. Mater.*, vol. 69, no. 5, pp. 393–396, 2013, doi: 10.1016/j.scriptamat.2013.05.027.

[74] L. Lilensten *et al.*, “On the heterogeneous nature of deformation in a strain-transformable beta metastable Ti-V-Cr-Al alloy,” *Acta Mater.*, vol. 162, pp. 268–276, 2019, doi: 10.1016/j.actamat.2018.10.003.

[75] X. Yang and C. R. Hutchinson, “Corrosion-wear of β-Ti alloy TMZF (Ti-12Mo-6Zr-2Fe) in simulated body fluid,” *Acta Biomater.*, vol. 42, pp. 429–439, 2016, doi: 10.1016/j.actbio.2016.07.008.

[76] B. Barry and P. Milburn, “Tribology, friction and traction: understanding shoe-surface interaction,” *Footwear Sci.*, vol. 5, no. 3, pp. 137–145, 2013, doi: 10.1080/19424280.2013.797030.

[77] J. R. Jones and M. J. Jansen, “Tribology for space applications,” *Proc. Inst. Mech. Eng. Part J J. Eng. Tribol.*, vol. 222, no. 8, pp. 997–1004, 2008, doi: 10.1243/13506501JET305.

[78] K. Holmberg and A. Erdemir, “Influence of tribology on global energy consumption, costs and emissions,” *Friction*, vol. 5, no. 3, pp. 263–284, 2017, doi: 10.1007/s40544-017-0183-5.

[79] N. Diomidis, S. Mischler, N. S. More, and M. Roy, “Tribo-electrochemical characterization of metallic biomaterials for total joint replacement,” *Acta Biomater.*, vol. 8, no. 2, pp. 852–859, 2012, doi: 10.1016/j.actbio.2011.09.034.

[80] H. S. Hothi, R. K. Whittaker, J. M. Meswania, G. W. Blunn, J. A. Skinner, and A. J. Hart, “Influence of stem type on material loss at the metal-on-metal pinnacle taper junction,” *Proc. Inst. Mech. Eng. Part H J. Eng. Med.*, vol. 229, no. 1, pp. 91–97, 2015, doi: 10.1177/0954411914567931.

[81] Y. Yan, *Bio-tribocorrosion in biomaterials and medical implants*. Elsevier, 2013.

[82] I. Hutchings and P. Shipway, *Tribology: Friction and wear of engineering materials: Second Edition*. Butterworth-Heinemann, 2017.

[83] D. Landolt and S. Mischler, *Tribocorrosion of passive metals and coatings*. Elsevier, 2011.

[84] J. Williams, *Engineering tribology*. Cambridge University Press, 2005.

[85] C. Greiner, J. Gagel, and P. Gumbsch, “Solids Under Extreme Shear: Friction-Mediated Subsurface Structural Transformations,” *Adv. Mater.*, 2019, doi: 10.1002/adma.201806705.

[86] C. C. Battaile, B. L. Boyce, C. R. Weinberger, S. V. Prasad, J. R. Michael, and B. G. Clark, “The hardness and strength of metal tribofilms: An apparent contradiction between nanoindentation and pillar compression,” *Acta Mater.*, vol. 60, no. 4, pp. 1712–1720, 2012, doi: 10.1016/j.actamat.2011.11.059.

[87] K. Farokhzadeh and A. Edrisy, “Transition between mild and severe wear in titanium alloys,” *Tribol. Int.*, vol. 94, pp. 98–111, 2016, doi: 10.1016/j.triboint.2015.08.020.

[88] P. J. Blau, “On the nature of running-in,” *Tribol. Int.*, vol. 38, no. 11-12 SPEC. ISS., pp. 1007–1012, 2005, doi: 10.1016/j.triboint.2005.07.020.

[89] D. Dowson, C. M. Taylor, and M. Godet, *The Running-In Process in Tribology: Proceeding of the 8th Leeds–Lyon Symposium on Tribology, Held in the Institute National des Science Appliquées de Lyon, France, 8–11 September 1981*. Elsevier, 2016.

[90] C. Greiner, J. Gagel, and P. Gumbsch, "Solids Under Extreme Shear: Friction-Mediated Subsurface Structural Transformations," *Adv. Mater.*, vol. 31, no. 26, 2019, doi: 10.1002/adma.201806705.

[91] R. Aghababaei, D. H. Warner, and J. F. Molinari, "Critical length scale controls adhesive wear mechanisms," *Nat. Commun.*, vol. 7, no. May, pp. 1–8, 2016, doi: 10.1038/ncomms11816.

[92] E. Milanese, T. Brink, R. Aghababaei, and J. F. Molinari, "Emergence of self-affine surfaces during adhesive wear," *Nat. Commun.*, vol. 10, no. 1, pp. 1–9, 2019, doi: 10.1038/s41467-019-09127-8.

[93] M. Kandeva-Ivanova, A. Vencl, and D. Karastoyanov, *Advanced Tribological Coatings For Heavy-Duty Applications: Case Studies*, no. February 2017. 2016.

[94] W. M. Rainforth, P. Zeng, L. Ma, A. N. Valdez, and T. Stewart, "Dynamic surface microstructural changes during tribological contact that determine the wear behaviour of hip prostheses: Metals and ceramics," *Faraday Discuss.*, vol. 156, pp. 41–57, 2012, doi: 10.1039/c2fd00002d.

[95] S. M. Kurtz *et al.*, "Do ceramic femoral heads reduce taper fretting corrosion in hip arthroplasty? A retrieval study," *Clin. Orthop. Relat. Res.*, vol. 471, no. 10, pp. 3270–3282, 2013, doi: 10.1007/s11999-013-3096-2.

[96] J. P. Davim, *Tribology for engineers: A practical guide*. Elsevier, 2011.

[97] D. C. Mazzucco, "Variation in joint fluid composition and its effect on the tribology of replacement joint articulation." Massachusetts Institute of Technology, 2003.

[98] A. P. Harsha and T. J. Joyce, "Challenges associated with using bovine serum in wear testing orthopaedic biopolymers," *Proc. Inst. Mech. Eng. Part H J. Eng. Med.*, vol. 225, no. 10, pp. 948–958, 2011, doi: 10.1177/0954411911416047.

[99] M. A. MacConail, “The function of intra-articular fibrocartilages,” *J Anat.*, vol. 66, pp. 210–227, 1932.

[100] P. S. Walker, D. Dowson, M. D. Longfield, and V. Wright, “‘ Boosted lubrication’ in synovial joints by fluid entrapment and enrichment.,” *Ann. Rheum. Dis.*, vol. 27, no. 6, p. 512, 1968.

[101] E. E. Stansbury and R. A. Buchanan, *Fundamentals of electrochemical corrosion*. ASM international, 2000.

[102] D. Prando *et al.*, “Corrosion of titanium: Part 1: Aggressive environments and main forms of degradation,” *J. Appl. Biomater. Funct. Mater.*, vol. 15, no. 4, pp. e291–e302, 2017, doi: 10.5301/jabfm.5000387.

[103] S. Mischler, “Triboelectrochemical techniques and interpretation methods in tribocorrosion: A comparative evaluation,” *Tribol. Int.*, vol. 41, no. 7, pp. 573–583, 2008, doi: 10.1016/j.triboint.2007.11.003.

[104] S. W. Watson, F. J. Friedersdorf, B. W. Madsen, and S. D. Cramer, “Methods of measuring wear-corrosion synergism,” *Wear*, vol. 183, pp. 476–484, 1995.

[105] B. W. Madsen, “Standard guide for determining amount of synergism between wear and corrosion,” *ASTM G119-93 Annu. B. ASTM Stand*, vol. 3, pp. 507–512, 1994.

[106] S. Akonko, D. Y. Li, and M. Ziomek-Moroz, “Effects of cathodic protection on corrosive wear of 304 stainless steel,” *Tribol. Lett.*, vol. 18, no. 3, pp. 405–410, 2005, doi: 10.1007/s11249-004-3205-1.

[107] A. Bidiville, M. Favero, P. Stadelmann, and S. Mischler, “Effect of surface chemistry on the mechanical response of metals in sliding tribocorrosion systems,” *Wear*, vol. 263, no. 1-6 SPEC. ISS., pp. 207–217, 2007, doi: 10.1016/j.wear.2007.01.066.

[108] H. H. Uhlig, “Mechanism of fretting corrosion,” *J. Appl. Mech. ASME*, vol. 21, no. 4, pp. 401–407, 1954.

[109] M. T. Mathew, M. J. Runa, M. Laurent, J. J. Jacobs, L. A. Rocha, and M. A. Wimmer, “Tribocorrosion behavior of CoCrMo alloy for hip prosthesis as a function

of loads: A comparison between two testing systems," *Wear*, vol. 271, no. 9–10, pp. 1210–1219, 2011, doi: 10.1016/j.wear.2011.01.086.

[110] M. M. Stack and G. H. Abdulrahman, "Mapping erosion-corrosion of carbon steel in oil exploration conditions: Some new approaches to characterizing mechanisms and synergies," *Tribol. Int.*, vol. 43, no. 7, pp. 1268–1277, 2010, doi: 10.1016/j.triboint.2010.01.005.

[111] M. J. Runa, M. T. Mathew, and L. A. Rocha, "Tribocorrosion response of the Ti6Al4V alloys commonly used in femoral stems," *Tribol. Int.*, vol. 68, pp. 85–93, 2013, doi: 10.1016/j.triboint.2013.09.022.

[112] F. Contu, B. Elsener, and H. Böhni, "A study of the potentials achieved during mechanical abrasion and the repassivation rate of titanium and Ti6Al4V in inorganic buffer solutions and bovine serum," *Electrochim. Acta*, vol. 50, no. 1, pp. 33–41, 2004, doi: 10.1016/j.electacta.2004.07.024.

[113] N. T. C. Oliveira and A. C. Guastaldi, "Electrochemical stability and corrosion resistance of Ti–Mo alloys for biomedical applications," *Acta Biomater.*, vol. 5, no. 1, pp. 399–405, 2009, doi: 10.1016/j.actbio.2008.07.010.

[114] I. Gurappa, "Characterization of different materials for corrosion resistance under simulated body fluid conditions," *Mater. Charact.*, vol. 49, no. 9, pp. 73–79, 2002, doi: 10.1002/jor.23150.

[115] I. Milošev, G. Žerjav, J. M. Calderon Moreno, and M. Popa, "Electrochemical properties, chemical composition and thickness of passive film formed on novel Ti-20Nb-10Zr-5Ta alloy," *Electrochim. Acta*, vol. 99, pp. 176–189, 2013, doi: 10.1016/j.electacta.2013.03.086.

[116] A. López-Ortega, J. L. Arana, and R. Bayón, "Tribocorrosion of Passive Materials: A Review on Test Procedures and Standards," *Int. J. Corros.*, vol. 2018, 2018, doi: 10.1155/2018/7345346.

[117] S. Cao and S. Mischler, “Modeling tribocorrosion of passive metals – A review,” *Curr. Opin. Solid State Mater. Sci.*, vol. 22, no. 4, pp. 127–141, 2018, doi: 10.1016/j.cossms.2018.06.001.

[118] R. J. K. Wood, “Tribo-corrosion of coatings: A review,” *J. Phys. D. Appl. Phys.*, vol. 40, no. 18, pp. 5502–5521, 2007, doi: 10.1088/0022-3727/40/18/S10.

[119] P. Ponthiaux, F. Wenger, D. Drees, and J. P. Celis, “Electrochemical techniques for studying tribocorrosion processes,” *Wear*, vol. 256, no. 5, pp. 459–468, 2004, doi: 10.1016/S0043-1648(03)00556-8.

[120] L. Yang, *Techniques for corrosion monitoring*. Southwest Research Institute. Institute of Materials, Minerals, and Mining., 2008.

[121] E. L. Bortel, B. Charbonnier, and R. Heuberger, “Development of a synthetic synovial fluid for tribological testing,” *Lubricants*, vol. 3, no. 4, pp. 664–686, 2015, doi: 10.3390/lubricants3040664.

[122] F. Contu, B. Elsener, and H. Böhni, “Serum effect on the electrochemical behaviour of titanium, Ti6Al4V and Ti6Al7Nb alloys in sulphuric acid and sodium hydroxide,” *Corros. Sci.*, vol. 46, no. 9, pp. 2241–2254, 2004, doi: 10.1016/j.corsci.2004.01.005.

[123] S. Karimi, T. Nickchi, and A. Alfantazi, “Effects of bovine serum albumin on the corrosion behaviour of AISI 316L, Co-28Cr-6Mo, and Ti-6Al-4V alloys in phosphate buffered saline solutions,” *Corros. Sci.*, vol. 53, no. 10, pp. 3262–3272, 2011, doi: 10.1016/j.corsci.2011.06.009.

[124] R. Yazdi, H. M. Ghasemi, M. Abedini, C. Wang, and A. Neville, “Mechanism of tribofilm formation on Ti6Al4V oxygen diffusion layer in a simulated body fluid,” *J. Mech. Behav. Biomed. Mater.*, vol. 77, no. October 2017, pp. 660–670, 2018, doi: 10.1016/j.jmbbm.2017.10.020.

[125] L. Kunčická, R. Kocich, and T. C. Lowe, “Advances in metals and alloys for joint replacement,” *Prog. Mater. Sci.*, vol. 88, pp. 232–280, 2017, doi: 10.1016/j.pmatsci.2017.04.002.

[126] P. Zeng, W. M. Rainforth, and R. B. Cook, “Characterisation of the oxide film on the taper interface from retrieved large diameter metal on polymer modular total hip replacements,” *Tribol. Int.*, vol. 89, pp. 86–96, 2015, doi: 10.1016/j.triboint.2014.12.012.

[127] E. Jensen, N. Espallargas, R. Johnsen, and C. B. von der Ohe, “Tribocorrosion properties of super duplex stainless steel in 3.4% NaCl and H2SO4 0.5 M solutions,” 2009.

[128] N. Espallargas, R. Johnsen, C. Torres, and A. I. Muñoz, “A new experimental technique for quantifying the galvanic coupling effects on stainless steel during tribocorrosion under equilibrium conditions,” *Wear*, vol. 307, no. 1–2, pp. 190–197, 2013.

[129] M. P. Licausi, A. I. Muñoz, V. A. Borrás, and N. Espallargas, “Tribocorrosion Mechanisms of Ti6Al4V in Artificial Saliva by Zero-Resistance Ammetry (ZRA) Technique,” *J. Bio- Tribo-Corrosion*, vol. 1, no. 1, pp. 1–11, 2015, doi: 10.1007/s40735-015-0008-x.

[130] K. Liu and L. Jiang, “Multifunctional integration: From biological to bio-inspired materials,” *ACS Nano*, vol. 5, no. 9, pp. 6786–6790, 2011, doi: 10.1021/nn203250y.

[131] G. D. Bixler and B. Bhushan, “Bioinspired rice leaf and butterfly wing surface structures combining shark skin and lotus effects,” *Soft Matter*, vol. 8, no. 44, pp. 11271–11284, 2012, doi: 10.1039/c2sm26655e.

[132] A. Marmur, “The lotus effect: Superhydrophobicity and metastability,” *Langmuir*, vol. 20, no. 9, pp. 3517–3519, 2004, doi: 10.1021/la036369u.

[133] P. Andersson *et al.*, “Microlubrication effect by laser-textured steel surfaces,” *Wear*, vol. 262, no. 3–4, pp. 369–379, 2007, doi: 10.1016/j.wear.2006.06.003.

[134] C. Momma, S. Nolte, B. N. Chichkov, F. V. Alvensleben, and A. Tünnermann, “Precise laser ablation with ultrashort pulses,” *Appl. Surf. Sci.*, vol. 109–110, pp. 15–19, 1997, doi: 10.1016/S0169-4332(96)00613-7.

[135] K. Sugioka and Y. Cheng, “Femtosecond laser three-dimensional micro-and nanofabrication,” *Appl. Phys. Rev.*, vol. 1, no. 4, 2014, doi: 10.1063/1.4904320.

[136] D. Patel, V. K. Jain, and J. Ramkumar, “Micro texturing on metallic surfaces: State of the art,” *Proc. Inst. Mech. Eng. Part B J. Eng. Manuf.*, vol. 232, no. 6, pp. 941–964, 2018, doi: 10.1177/0954405416661583.

[137] W. Pfleging, R. Kumari, H. Besser, T. Scharnweber, and J. D. Majumdar, “Laser surface textured titanium alloy (Ti-6Al-4V): Part 1 - Surface characterization,” *Appl. Surf. Sci.*, vol. 355, pp. 104–111, 2015, doi: 10.1016/j.apsusc.2015.06.175.

[138] R. Kumari, T. Scharnweber, W. Pfleging, H. Besser, and J. D. Majumdar, “Laser surface textured titanium alloy (Ti-6Al-4V) - Part II - Studies on bio-compatibility,” *Appl. Surf. Sci.*, vol. 357, pp. 750–758, 2015, doi: 10.1016/j.apsusc.2015.08.255.

[139] T. Hu, L. Hu, and Q. Ding, “Effective solution for the tribological problems of Ti-6Al-4V: Combination of laser surface texturing and solid lubricant film,” *Surf. Coatings Technol.*, vol. 206, no. 24, pp. 5060–5066, 2012, doi: 10.1016/j.surfcoat.2012.06.014.

[140] D. Choudhury, D. Rebenda, S. Sasaki, P. Hekrle, M. Vrbka, and M. Zou, “Enhanced lubricant film formation through micro-dimpled hard-on-hard artificial hip joint: An in-situ observation of dimple shape effects,” *J. Mech. Behav. Biomed. Mater.*, vol. 81, no. October 2017, pp. 120–129, 2018, doi: 10.1016/j.jmbbm.2018.02.014.

[141] B. G. I. Dance and E. J. C. Kellar, “Workpiece structure modification.” Google Patents, Feb. 23, 2010.

[142] B. G. I. Dance and A. L. Buxton, “An introduction to Surfi-Sculpt technology-new opportunities, new challenges,” *Proc. ICBT*, vol. 7, 2007.

[143] A. Temmler, E. Willenborg, N. Pirch, and K. Wissenbach, “Structuring by Remelting,” *Technology*, no. June, pp. 403–408, 2009.

[144] J. Svensson, N. M. Bulgakova, O. A. Nerushev, and E. E. B. Campbell, “Marangoni effect in Si O2 during field-directed chemical vapor deposition growth of carbon

nanotubes," *Phys. Rev. B - Condens. Matter Mater. Phys.*, vol. 73, no. 20, pp. 1–5, 2006, doi: 10.1103/PhysRevB.73.205413.

[145] A. Temmler *et al.*, "Surface structuring by laser remelting of metals," *J. Laser Appl.*, vol. 29, no. 1, p. 012015, 2017, doi: 10.2351/1.4972414.

[146] A. Temmler, D. M. Liu, S. Drinck, J. B. Luo, and R. Poprawe, "Experimental investigation on a new hybrid laser process for surface structuring by vapor pressure on Ti6Al4V," *J. Mater. Process. Technol.*, vol. 277, no. October 2019, p. 116450, 2020, doi: 10.1016/j.jmatprotec.2019.116450.

[147] C. Gachot, A. Rosenkranz, S. M. Hsu, and H. L. Costa, "A critical assessment of surface texturing for friction and wear improvement," *Wear*, vol. 372–373, pp. 21–41, 2017, doi: 10.1016/j.wear.2016.11.020.

[148] M. Abdel-Hady Gepreel and M. Niinomi, "Biocompatibility of Ti-alloys for long-term implantation," *J. Mech. Behav. Biomed. Mater.*, vol. 20, pp. 407–415, 2013, doi: 10.1016/j.jmbbm.2012.11.014.

[149] H. C. Hsu, S. C. Wu, S. K. Hsu, J. Y. Syu, and W. F. Ho, "The structure and mechanical properties of as-cast Ti-25Nb-xSn alloys for biomedical applications," *Mater. Sci. Eng. A*, vol. 568, pp. 1–7, 2013, doi: 10.1016/j.msea.2013.01.002.

[150] E. P.J. Bania, "Beta titanium alloys and their role in the titanium industry," *JOM*, vol. 46, pp. 6-19, 1994.

[151] L. Ma and W. M. Rainforth, "The effect of lubrication on the friction and wear of Biolox®delta," *Acta Biomater.*, vol. 8, no. 6, pp. 2348–2359, 2012, doi: http://dx.doi.org/10.1016/j.actbio.2011.12.037.

[152] F. Sun *et al.*, "Investigation of early stage deformation mechanisms in a metastable β titanium alloy showing combined twinning-induced plasticity and transformation-induced plasticity effects," *Acta Mater.*, vol. 61, no. 17, pp. 6406–6417, 2013, doi: 10.1016/j.actamat.2013.07.019.

[153] E. L. Pang, E. J. Pickering, S. I. Baik, D. N. Seidman, and N. G. Jones, “The effect of zirconium on the omega phase in Ti-24Nb-[0–8]Zr (at.%) alloys,” *Acta Mater.*, vol. 153, pp. 62–70, 2018, doi: 10.1016/j.actamat.2018.04.016.

[154] A. A. Salem, S. R. Kalidindi, and R. D. Doherty, “Strain hardening of titanium: Role of deformation twinning,” *Acta Mater.*, vol. 51, no. 14, pp. 4225–4237, 2003, doi: 10.1016/S1359-6454(03)00239-8.

[155] J. W. Christian and S. Mahajan, “Deformation twinning,” *Prog. Mater. Sci.*, vol. 39, no. 1–2, pp. 1–157, 1995, doi: 10.1016/0079-6425(94)00007-7.

[156] S. Ozan, J. Lin, Y. Li, R. Ipek, and C. Wen, “Development of Ti-Nb-Zr alloys with high elastic admissible strain for temporary orthopedic devices,” *Acta Biomater.*, vol. 20, pp. 176–187, 2015, doi: 10.1016/j.actbio.2015.03.023.

[157] M. Niinomi, C. K. Kuo, and P. X. Ma, “Mechanical properties of biomedical titanium alloys,” *Mater. Sci. Eng. A*, vol. 243, pp. 231–236, 1998, doi: 10.1016/S0142-9612(00)00201-5.

[158] M. Besse, P. Castany, and T. Gloriant, “Mechanisms of deformation in gum metal TNTZ-O and TNTZ titanium alloys: A comparative study on the oxygen influence,” *Acta Mater.*, vol. 59, no. 15, pp. 5982–5988, 2011, doi: 10.1016/j.actamat.2011.06.006.

[159] P. Castany, M. Besse, and T. Gloriant, “In situ TEM study of dislocation slip in a metastable β titanium alloy,” *Scr. Mater.*, vol. 66, no. 6, pp. 371–373, 2012, doi: 10.1016/j.scriptamat.2011.11.036.

[160] S. Sadeghpour, S. M. Abbasi, M. Morakabati, and L. P. Karjalainen, “Effect of dislocation channeling and kink band formation on enhanced tensile properties of a new beta Ti alloy,” *J. Alloys Compd.*, vol. 808, p. 151741, 2019, doi: 10.1016/j.jallcom.2019.151741.

[161] M. Tane *et al.*, “Low Young’s modulus in Ti-Nb-Ta-Zr-O alloys: Cold working and oxygen effects,” *Acta Mater.*, vol. 59, no. 18, pp. 6975–6988, 2011, doi: 10.1016/j.actamat.2011.07.050.

[162] “Titanium Price 2020 [Updated Daily] - Metalary.” https://www.metalary.com/titanium-price/ (accessed Mar. 11, 2021).

[163] P. Wang, M. Todai, and T. Nakano, “Beta titanium single crystal with bone-like elastic modulus and large crystallographic elastic anisotropy,” *J. Alloys Compd.*, vol. 782, pp. 667–671, 2019, doi: 10.1016/j.jallcom.2018.12.236.

[164] I. Gutierrez-Urrutia, C. L. Li, S. Emura, X. Min, and K. Tsuchiya, “Study of {332}<113> twinning in a multilayered Ti-10Mo-xFe (x = 1–3) alloy by ECCI and EBSD,” *Sci. Technol. Adv. Mater.*, vol. 17, no. 1, pp. 220–228, 2016, doi: 10.1080/14686996.2016.1177439.

[165] W. D. Zeng and Y. G. Zhou, “Effect of beta flecks on mechanical properties of Ti–10V–2Fe–3Al alloy,” *Mater. Sci. Eng. A*, vol. 260, no. 1–2, pp. 203–211, 1999, doi: 10.1016/s0921-5093(98)00954-x.

[166] C. E. Shamblen, “Minimizing beta flecks in the ti-17 alloy,” *Metall. Mater. Trans. B Process Metall. Mater. Process. Sci.*, vol. 28, no. 5, pp. 899–903, 1997, doi: 10.1007/s11663-997-0017-3.

[167] M. J. Lai, C. C. Tasan, and D. Raabe, “Acta Materialia On the mechanism of { 332 } twinning in metastable b titanium alloys,” *Acta Mater.*, vol. 111, pp. 173–186, 2016, doi: 10.1016/j.actamat.2016.03.040.

[168] L. Ren, W. Xiao, C. Ma, R. Zheng, and L. Zhou, “Development of a high strength and high ductility near β-Ti alloy with twinning induced plasticity effect,” *Scr. Mater.*, vol. 156, pp. 47–50, 2018, doi: 10.1016/j.scriptamat.2018.07.012.

[169] S. A. Mantri *et al.*, “Deformation Induced hierarchical twinning coupled with omega transformation in a metastable β-Ti Alloy,” *Sci. Rep.*, vol. 9, no. 1, pp. 1–8, 2019, doi: 10.1038/s41598-018-37865-0.

[170] E. Plancher, C. C. Tasan, S. Sandloebes, and D. Raabe, “On dislocation involvement in Ti-Nb gum metal plasticity,” *Scr. Mater.*, vol. 68, no. 10, pp. 805–808, 2013, doi: 10.1016/j.scriptamat.2013.01.034.

[171] P. Castany, M. Besse, and T. Gloriant, “Dislocation mobility in gum metal β-titanium alloy studied via in situ transmission electron microscopy,” *Phys. Rev. B - Condens. Matter Mater. Phys.*, vol. 84, no. 2, pp. 1–4, 2011, doi: 10.1103/PhysRevB.84.020201.

[172] M. J. Lai, T. Li, and D. Raabe, “ω Phase Acts As a Switch Between Dislocation Channeling and Joint Twinning- and Transformation-Induced Plasticity in a Metastable B Titanium Alloy,” *Acta Mater.*, vol. 151, pp. 67–77, 2018, doi: 10.1016/j.actamat.2018.03.053.

[173] C. H. Wang, A. M. Russell, and G. H. Cao, “A semi-empirical approach to the prediction of deformation behaviors of β-Ti alloys,” *Scr. Mater.*, vol. 158, pp. 62–65, 2019, doi: 10.1016/j.scriptamat.2018.08.035.

[174] P. Castany, Y. Yang, E. Bertrand, and T. Gloriant, “Reversion of a Parent 310 α″ Martensitic Twinning System at the Origin of {332 } 113 ©β Twins Observed in Metastable β Titanium Alloys,” *Phys. Rev. Lett.*, vol. 117, no. 24, pp. 1–6, 2016, doi: 10.1103/PhysRevLett.117.245501.

[175] W. Xu *et al.*, “Effects of Mo content on corrosion and tribocorrosion behaviours of Ti-Mo orthopaedic alloys fabricated by powder metallurgy,” *Corros. Sci.*, vol. 168, no. February, 2020, doi: 10.1016/j.corsci.2020.108557.

[176] I. Hacisalihoglu, A. Samancioglu, F. Yildiz, G. Purcek, and A. Alsaran, “Tribocorrosion properties of different type titanium alloys in simulated body fluid,” *Wear*, vol. 332–333, pp. 679–686, 2014, doi: 10.1016/j.wear.2014.12.017.

[177] J. Ureña, S. Tsipas, A. M. Pinto, F. Toptan, E. Gordo, and A. Jiménez-Morales, “Corrosion and tribocorrosion behaviour of β-type Ti-Nb and Ti-Mo surfaces designed by diffusion treatments for biomedical applications,” *Corros. Sci.*, vol. 140, no. January, pp. 51–60, 2018, doi: 10.1016/j.corsci.2018.06.024.

[178] Z. Wang, Y. Zhou, H. Wang, Y. Li, and W. Huang, “Tribocorrosion behavior of Ti-30Zr alloy for dental implants,” *Mater. Lett.*, vol. 218, pp. 190–192, 2018, doi: 10.1016/j.matlet.2018.02.008.

[179] S. Kurtz, K. Ong, E. Lau, F. Mowat, and M. Halpern, “Projections of primary and revision hip and knee arthroplasty in the United States from 2005 to 2030,” *J. Bone Jt. Surg. - Ser. A*, vol. 89, no. 4, pp. 780–785, 2007, doi: 10.2106/JBJS.F.00222.

[180] M. Baxmann, A. M. Pfaff, C. Schilling, T. M. Grupp, and M. M. Morlock, “Biomechanical Evaluation of the Fatigue Performance, the Taper Corrosion and the Metal Ion Release of a Dual Taper Hip Prosthesis under Physiological Environmental Conditions,” *Biotribology*, vol. 12, no. April, pp. 1–7, 2017, doi: 10.1016/j.biotri.2017.07.002.

[181] C. E. B. Marino, E. M. de Oliviera, R. C. Rocha-Filho, and S. R. Biaggio, “On the stability of thin-anodic-oxide films of titanium in acid phosphoric media,” *Corros. Sci.*, vol. 43, no. 8, pp. 1465–1476, 2001, doi: 10.1016/S0010-938X(00)00162-1.

[182] M. V. Popa *et al.*, “Corrosion susceptibility of implant materials Ti-5Al-4V and Ti-6Al-4Fe in artificial extra-cellular fluids,” *Electrochim. Acta*, vol. 49, no. 13, pp. 2113–2121, 2004, doi: 10.1016/j.electacta.2003.12.036.

[183] N. Diomidis, S. Mischler, N. S. More, M. Roy, and S. N. Paul, “Fretting-corrosion behavior of β titanium alloys in simulated synovial fluid,” *Wear*, vol. 271, no. 7–8, pp. 1093–1102, 2011, doi: 10.1016/j.wear.2011.05.010.

[184] S. Cao and S. Mischler, “Modeling tribocorrosion of passive metals – A review,” *Curr. Opin. Solid State Mater. Sci.*, no. June, pp. 1–15, 2018, doi: 10.1016/j.cossms.2018.06.001.

[185] R. Yazdi, H. M. Ghasemi, M. Abedini, C. Wang, and A. Neville, “Mechanism of tribofilm formation on Ti6Al4V oxygen diffusion layer in a simulated body fluid,” *J. Mech. Behav. Biomed. Mater.*, vol. 77, pp. 660–670, 2018, doi: 10.1016/j.jmbbm.2017.10.020.

[186] M. A. Wimmer *et al.*, “The effect of contact load on CoCrMo wear and the formation and retention of tribofilms,” *Wear*, vol. 332–333, pp. 643–649, 2015, doi: 10.1016/j.wear.2015.02.013.

[187] Y. Zhou *et al.*, “Comparative research on the effect of an oxide coating and a tribo-oxide layer on dry sliding wear of Ti–6Al–4V alloy,” *Proc. Inst. Mech. Eng. Part J J. Eng. Tribol.*, vol. 232, no. 12, pp. 1569–1580, 2018, doi: 10.1177/1350650118757329.

[188] L. Wang, Q. Y. Zhang, X. X. Li, X. H. Cui, and S. Q. Wang, “Dry sliding wear behavior of Ti-6.5Al-3.5Mo-1.5Zr-0.3Si alloy,” *Metall. Mater. Trans. A Phys. Metall. Mater. Sci.*, vol. 45, no. 4, pp. 2284–2296, 2014, doi: 10.1007/s11661-013-2167-z.

[189] M. A. Wimmer *et al.*, “Wear mechanisms in metal-on-metal bearings: The importance of tribochemical reaction layers,” *J. Orthop. Res.*, vol. 28, no. 4, pp. 436–443, 2010, doi: 10.1002/jor.21020.

[190] D. B. Williams and C. B. Carter, “The transmission electron microscope,” in *Transmission electron microscopy*, Springer, 1996, pp. 3–17.

[191] J. F. Archard, “The temperature of rubbing surfaces,” *Wear*, vol. 2, no. 6, pp. 438–455, 1959, doi: 10.1016/0043-1648(59)90159-0.

[192] M. D. Marko, J. P. Kyle, Y. S. Wang, and E. J. Terrell, “Tribological investigations of the load, temperature, and time dependence of wear in sliding contact,” *PLoS One*, vol. 12, no. 4, pp. 1–20, 2017, doi: 10.1371/journal.pone.0175198.

[193] Z. Zhang and Y. Liu, “Recent progresses of understanding the viscosity of concentrated protein solutions,” *Curr. Opin. Chem. Eng.*, vol. 16, pp. 48–55, 2017, doi: 10.1016/j.coche.2017.04.001.

[194] J. Jaspe and S. J. Hagen, “Do protein molecules unfold in a simple shear flow?,” *Biophys. J.*, vol. 91, no. 9, pp. 3415–3424, 2006, doi: 10.1529/biophysj.106.089367.

[195] M. M. Castellanos, J. A. Pathak, and R. H. Colby, “Both protein adsorption and aggregation contribute to shear yielding and viscosity increase in protein solutions,” *Soft Matter*, vol. 10, no. 1, pp. 122–131, 2014, doi: 10.1039/c3sm51994e.

[196] V. Pejaković, V. Totolin, and M. Rodríguez Ripoll, “Tribocorrosion behaviour of Ti6Al4V in artificial seawater at low contact pressures,” *Tribol. Int.*, vol. 119, no. October 2017, pp. 55–65, 2018, doi: 10.1016/j.triboint.2017.10.025.

[197] M. A. Khan, R. L. Williams, and D. F. Williams, “The corrosion behaviour of Ti–6Al–4V, Ti–6Al–7Nb and Ti–13Nb–13Zr in protein solutions,” *Biomaterials*, vol. 20, no. 7, pp. 631–637, 1999, doi: https://doi.org/10.1016/S0142-9612(98)00217-8.

[198] M. A. Khan, R. L. Williams, and D. F. Williams, “In-vitro corrosion and wear of titanium alloys in the biological environment,” *Biomaterials*, vol. 17, no. 22, pp. 2117–2126, 1996, doi: https://doi.org/10.1016/0142-9612(96)00029-4.

[199] M. T. Mathew *et al.*, “Tribolayer formation in a metal-on-metal (MoM) hip joint: An electrochemical investigation,” *J. Mech. Behav. Biomed. Mater.*, vol. 29, pp. 199–212, 2014, doi: 10.1016/j.jmbbm.2013.08.018.

[200] Z. Wang, Y. Yan, Y. Su, and L. Qiao, “Effect of proteins on the surface microstructure evolution of a CoCrMo alloy in bio-tribocorrosion processes,” *Colloids Surfaces B Biointerfaces*, vol. 145, pp. 176–184, 2016, doi: 10.1016/j.colsurfb.2016.05.002.

[201] Y. Liao, R. Pourzal, M. A. Wimmer, J. J. Jacobs, A. Fischer, and L. D. Marks, “Graphitic Tribological Layers in,” *Science (80-.).*, vol. 334, no. December, pp. 1687–1690, 2011, doi: 10.1126/science.1213902.

[202] A. Erdemir *et al.*, “Carbon-based tribofilms from lubricating oils,” *Nature*, vol. 536, no. 7614, pp. 67–71, 2016, doi: 10.1038/nature18948.

[203] P. Zeng, A. Rana, R. Thompson, and W. M. Rainforth, “Subsurface characterisation of wear on mechanically polished and electro-polished biomedical grade CoCrMo,” *Wear*, vol. 332–333, pp. 650–661, 2015, doi: 10.1016/j.wear.2015.02.007.

[204] Z. Wang, Y. Yan, Y. Su, and L. Qiao, “Effect of electrochemical corrosion on the subsurface microstructure evolution of a CoCrMo alloy in albumin containing environment,” *Appl. Surf. Sci.*, vol. 406, pp. 319–329, 2017, doi: 10.1016/j.apsusc.2017.02.152.

[205] V. A. Borzova *et al.*, “Kinetics of thermal denaturation andaggregation of bovine serum albumin,” *PLoS One*, vol. 11, no. 4, pp. 1–29, 2016, doi: 10.1371/journal.pone.0153495.

[206] M. Lundqvist, J. Stigler, G. Elia, I. Lynch, T. Cedervall, and K. A. Dawson, "Nanoparticle size and surface properties determine the protein corona with possible implications for biological impacts," *Proc. Natl. Acad. Sci. U. S. A.*, vol. 105, no. 38, pp. 14265–14270, 2008, doi: 10.1073/pnas.0805135105.

[207] M. A. Khan, R. L. Williams, and D. F. Williams, "Conjoint corrosion and wear in titanium alloys," *Biomaterials*, vol. 20, no. 8, pp. 765–772, 1999, doi: https://doi.org/10.1016/S0142-9612(98)00229-4.

[208] N. Gao, C. T. Wang, R. J. K. Wood, and T. G. Langdon, "Tribological properties of ultrafine-grained materials processed by severe plastic deformation," *J. Mater. Sci.*, vol. 47, no. 12, pp. 4779–4797, 2012, doi: 10.1007/s10853-011-6231-z.

[209] X. Chen, Z. Han, X. Li, and K. Lu, "Lowering coefficient of friction in cu alloys with stable gradient nanostructures," *Sci. Adv.*, vol. 2, no. 12, pp. 1–8, 2016, doi: 10.1126/sciadv.1601942.

[210] J. Perret *et al.*, "EBSD, SEM and FIB characterisation of subsurface deformation during tribocorrosion of stainless steel in sulphuric acid," *Wear*, vol. 269, no. 5–6, pp. 383–393, 2010, doi: 10.1016/j.wear.2010.04.023.

[211] M. Favero, P. Stadelmann, and S. Mischler, "Effect of the applied potential of the near surface microstructure of a 316L steel submitted to tribocorrosion in sulfuric acid," *J. Phys. D. Appl. Phys.*, vol. 39, no. 15, pp. 3175–3183, 2006, doi: 10.1088/0022-3727/39/15/S07.

[212] U. N. Desa, "World population prospects 2019: Highlights," *New York United Nations Dep. Econ. Soc. Aff.*, 2019.

[213] W. Xu *et al.*, "Additive manufacturing of strong and ductile Ti-6Al-4V by selective laser melting via in situ martensite decomposition," *Acta Mater.*, vol. 85, pp. 74–84, 2015, doi: 10.1016/j.actamat.2014.11.028.

[214] C. de Formanoir *et al.*, "Micromechanical behavior and thermal stability of a dual-phase α+α' titanium alloy produced by additive manufacturing," *Acta Mater.*, vol. 162, pp. 149–162, 2019, doi: 10.1016/j.actamat.2018.09.050.

[215] X. Tan *et al.*, “Revealing martensitic transformation and α/β interface evolution in electron beam melting three-dimensional-printed Ti-6Al-4V,” *Sci. Rep.*, vol. 6, no. January, pp. 1–10, 2016, doi: 10.1038/srep26039.

[216] J. Archard, “Contact and rubbing of flat surfaces,” *J. Appl. Phys.*, vol. 24, no. 8, pp. 981–988, 1953.

[217] P. L. Hurricks, “Some metallurgical factors controlling the adhesive and abrasive wear resistance of steels. A review,” *Wear*, vol. 26, no. 3, pp. 285–304, 1973.

[218] A. Leyland and A. Matthews, “On the significance of the H/E ratio in wear control: A nanocomposite coating approach to optimised tribological behaviour,” *Wear*, vol. 246, no. 1–2, pp. 1–11, 2000, doi: 10.1016/S0043-1648(00)00488-9.

[219] T. L. Oberle, “Wear of metals,” *JOM*, vol. 3, no. 6, pp. 438–439, 1951.

[220] T. S. Jun, G. Sernicola, F. P. E. Dunne, and T. B. Britton, “Local deformation mechanisms of two-phase Ti alloy,” *Mater. Sci. Eng. A*, vol. 649, pp. 39–47, 2016, doi: 10.1016/j.msea.2015.09.016.

[221] M. F. Savage, J. Tatalovich, and M. J. Mills, “Anisotropy in the room-temperature deformation of α-β colonies in titanium alloys: Role of the α-β interface,” *Philos. Mag.*, vol. 84, no. 11, pp. 1127–1154, 2004, doi: 10.1080/1478643032000158305.

[222] J. R. Greer and W. D. Nix, “Nanoscale gold pillars strengthened through dislocation starvation,” *Phys. Rev. B - Condens. Matter Mater. Phys.*, vol. 73, no. 24, pp. 1–6, 2006, doi: 10.1103/PhysRevB.73.245410.

[223] S. A. Khairallah, A. T. Anderson, A. M. Rubenchik, and W. E. King, “Laser powder-bed fusion additive manufacturing: Physics of complex melt flow and formation mechanisms of pores, spatter, and denudation zones,” *Acta Mater.*, vol. 108, pp. 36–45, 2016, doi: 10.1201/9781315119106.

[224] T. Zhang, H. Li, Z. Guoqing, and B. Shen, “Evolution of molten pool during selective laser melting of Ti-6Al-4V Manuscript version : Accepted Manuscript,” no. November, 2018, doi: 10.1088/1361-6463/aaee04.

[225] C. M. Cepeda-Jiménez, F. Potenza, E. Magalini, V. Luchin, A. Molinari, and M. T. Pérez-Prado, “Effect of energy density on the microstructure and texture evolution of Ti-6Al-4V manufactured by laser powder bed fusion,” *Mater. Charact.*, vol. 163, no. September 2019, p. 110238, 2020, doi: 10.1016/j.matchar.2020.110238.

[226] U. Scipioni Bertoli, A. J. Wolfer, M. J. Matthews, J. P. R. Delplanque, and J. M. Schoenung, “On the limitations of Volumetric Energy Density as a design parameter for Selective Laser Melting,” *Mater. Des.*, vol. 113, pp. 331–340, 2017, doi: 10.1016/j.matdes.2016.10.037.

[227] X. Y. Zhang, G. Fang, S. Leeflang, A. J. Böttger, A. A. Zadpoor, and J. Zhou, “Effect of subtransus heat treatment on the microstructure and mechanical properties of additively manufactured Ti-6Al-4V alloy,” *J. Alloys Compd.*, vol. 735, pp. 1562–1575, 2018, doi: 10.1016/j.jallcom.2017.11.263.

[228] R. Ding, J. Gong, A. J. Wilkinson, and I. P. Jones, “Transmission electron microscopy of deformed Ti-6Al-4V micro-cantilevers,” *Philos. Mag.*, vol. 92, no. 25–27, pp. 3290–3314, 2012, doi: 10.1080/14786435.2012.700414.

[229] M. Dao, “Toward a quantitative understanding of mechanical behavior of nanocrystalline metals,” vol. 55, no. 143, pp. 4041–4065, 2007, doi: 10.1016/j.actamat.2007.01.038.

[230] B. Chen, S. Li, H. Zong, X. Ding, J. Sun, and E. Ma, “Unusual activated processes controlling dislocation motion in body-centered-cubic high-entropy alloys,” *Proc. Natl. Acad. Sci. U. S. A.*, vol. 117, no. 28, pp. 16199–161206, 2020, doi: 10.1073/pnas.1919136117.

[231] E. O. Hall, “The deformation and ageing of mild steel: III discussion of results,” *Proc. Phys. Soc. Sect. B*, vol. 64, no. 9, p. 747, 1951.

[232] Y. Guo, T. B. Britton, and A. J. Wilkinson, “Slip band-grain boundary interactions in commercial-purity titanium,” *Acta Mater.*, vol. 76, pp. 1–12, 2014, doi: 10.1016/j.actamat.2014.05.015.

[233] M. Y. Gutkin, T. Ishizaki, S. Kuramoto, and I. A. Ovid'ko, "Nanodisturbances in deformed Gum Metal," *Acta Mater.*, vol. 54, no. 9, pp. 2489–2499, 2006, doi: 10.1016/j.actamat.2006.01.027.

[234] J. P. Cui, Y. L. Hao, S. J. Li, M. L. Sui, D. X. Li, and R. Yang, "Reversible movement of homogenously nucleated dislocations in a β-titanium alloy," *Phys. Rev. Lett.*, vol. 102, no. 4, 2009, doi: 10.1103/PhysRevLett.102.045503.

[235] J. He *et al.*, "The Martensitic Transformation and Mechanical Properties of Ti6Al4V Prepared via Selective Laser Melting," *Materials (Basel).*, vol. 12, no. 2, p. 321, 2019, doi: 10.3390/ma12020321.

[236] H. K. Rafi, N. V. Karthik, H. Gong, T. L. Starr, and B. E. Stucker, "Microstructures and mechanical properties of Ti6Al4V parts fabricated by selective laser melting and electron beam melting," *J. Mater. Eng. Perform.*, vol. 22, no. 12, pp. 3872–3883, 2013, doi: 10.1007/s11665-013-0658-0.

[237] J. R. Greer and J. T. M. De Hosson, "Plasticity in small-sized metallic systems: Intrinsic versus extrinsic size effect," *Prog. Mater. Sci.*, vol. 56, no. 6, pp. 654–724, 2011, doi: 10.1016/j.pmatsci.2011.01.005.

[238] D. Guan, W. M. Rainforth, L. Ma, B. Wynne, and J. Gao, "Twin recrystallization mechanisms and exceptional contribution to texture evolution during annealing in a magnesium alloy," *Acta Mater.*, vol. 126, pp. 132–144, 2017, doi: 10.1016/j.actamat.2016.12.058.

[239] X. Zhou and X. Min, "Effect of grain boundary angle on {332}<113> twinning transfer behavior in β-type Ti–15Mo–5Zr alloy," *J. Mater. Sci.*, vol. 53, no. 11, pp. 8604–8618, 2018, doi: 10.1007/s10853-018-2167-x.

[240] S. Shim, H. Bei, M. K. Miller, G. M. Pharr, and E. P. George, "Effects of focused ion beam milling on the compressive behavior of directionally solidified micropillars and the nanoindentation response of an electropolished surface," *Acta Mater.*, vol. 57, no. 2, pp. 503–510, 2009, doi: 10.1016/j.actamat.2008.09.033.

[241] J. Mayer, L. a Giannuzzi, T. Kamino, and J. Michael, “TEM Sample Preparation and Damage,” *MRS Bull.*, vol. 32, no. May 2007, pp. 400–407, 2007.

[242] M. G. Bryant *et al.*, “Surface and subsurface changes as a result of tribocorrosion at the stem-neck interface of bi-modular prosthesis,” *Biotribology*, vol. 10, pp. 1–16, 2017, doi: 10.1016/j.biotri.2017.02.002.

[243] Z. Wang, Y. Yan, and L. Qiao, “Protein adsorption on implant metals with various deformed surfaces,” *Colloids Surfaces B Biointerfaces*, vol. 156, pp. 62–70, 2017, doi: 10.1016/j.colsurfb.2017.05.015.

[244] E. Matykina, R. Arrabal, R. Z. Valiev, J. M. Molina-Aldareguia, P. Belov, and I. Sabirov, “Electrochemical Anisotropy of Nanostructured Titanium for Biomedical Implants,” *Electrochim. Acta*, vol. 176, pp. 1221–1232, 2015, doi: 10.1016/j.electacta.2015.07.128.

[245] W. Huang, Z. Wang, C. Liu, and Y. Yu, “Wear and Electrochemical Corrosion Behavior of Biomedical Ti–25Nb–3Mo–3Zr–2Sn Alloy in Simulated Physiological Solutions,” *J. Bio- Tribo-Corrosion*, vol. 1, no. 1, pp. 1–10, 2015, doi: 10.1007/s40735-014-0001-9.

[246] A. W. Thompson, Z. D. Harris, and J. T. Burns, “Examination of focused ion beam-induced damage during platinum deposition in the near-surface region of an aerospace aluminum alloy,” *Micron*, vol. 118, no. July 2018, pp. 43–49, 2019, doi: 10.1016/j.micron.2018.12.004.

[247] J. Yu, J. Liu, J. Zhang, and J. Wu, “TEM investigation of FIB induced damages in preparation of metal material TEM specimens by FIB,” *Mater. Lett.*, vol. 60, no. 2, pp. 206–209, 2006, doi: 10.1016/j.matlet.2005.08.018.

[248] A. M. A. Mohamed, A. M. Abdullah, and N. A. Younan, “Corrosion behavior of superhydrophobic surfaces: A review,” *Arab. J. Chem.*, vol. 8, no. 6, pp. 749–765, 2015, doi: 10.1016/j.arabjc.2014.03.006.

[249] L. B. Boinovich, A. M. Emelyanenko, A. D. Modestov, A. G. Domantovsky, and K. A. Emelyanenko, “Not simply repel water: the diversified nature of corrosion

protection by superhydrophobic coatings," *Mendeleev Commun.*, vol. 27, no. 3, pp. 254–256, 2017, doi: 10.1016/j.mencom.2017.05.012.

[250] H. Y. Zhang, J. B. Luo, M. Zhou, Y. Zhang, and Y. L. Huang, "Biotribological properties at the stem-cement interface lubricated with different media," *J. Mech. Behav. Biomed. Mater.*, vol. 20, pp. 209–216, 2013, doi: 10.1016/j.jmbbm.2013.01.001.

[251] G. Straffelini and A. Molinari, "Dry sliding wear of Ti-6Al-4V alloy as influenced by the counterface and sliding conditions," *Wear*, vol. 236, no. 1–2, pp. 328–338, 1999, doi: 10.1016/S0043-1648(99)00292-6.

[252] K. H. Z. Gahr, "Formation of wear debris by the abrasion of ductile metals," *Wear*, vol. 74, no. 2, pp. 353–373, 1981, doi: 10.1016/0043-1648(81)90173-3.

[253] N. Argibay, M. Chandross, S. Cheng, and J. R. Michael, "Linking microstructural evolution and macro-scale friction behavior in metals," *J. Mater. Sci.*, vol. 52, no. 5, pp. 2780–2799, 2017, doi: 10.1007/s10853-016-0569-1.